INTRINSIC SELF-SENSING OF PULSED LASER ABLATION IN CARBON NANOFIBER-MODIFIED GLASS FIBER/EPOXY LAMINATES

by

Rajan Jain

A Thesis

Submitted to the Faculty of Purdue University

In Partial Fulfillment of the Requirements for the degree of

Master of Science

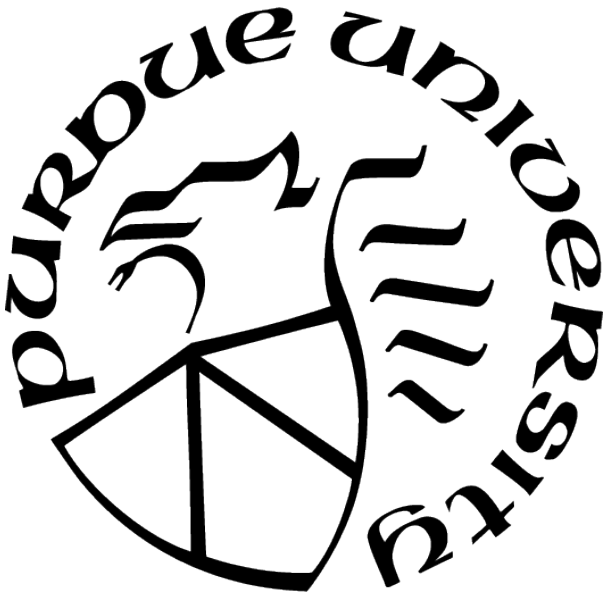

School of Aeronautics and Astronautics

West Lafayette, Indiana

May 2021

THE PURDUE UNIVERSITY GRADUATE SCHOOL
STATEMENT OF COMMITTEE APPROVAL

Dr. Tyler N. Tallman, Chair

School of Aeronautics and Astronautics

Dr. R. Byron Pipes

School of Aeronautics and Astronautics

Dr. Weinong W. Chen

School of Aeronautics and Astronautics

Approved by:

Dr. Gregory A. Blaisdell

For Inj and the progress of science

ACKNOWLEDGMENTS

I would like to start by thanking my advisor, Dr. Tyler N. Tallman for providing me an opportunity to work at his research lab, TNT Labs in the School of Aeronautics and Astronautics at Purdue University to work on this project. I am very grateful to have worked under the guidance of such an incredible advisor.

Next, I would like to thank my committee members, Dr. R. Byron Pipes for introducing me to experimental domain of composites, especially with the experimental characterization and manufacturing of advanced composites. I would also like to convey my gratitude to Dr. Weinong W. Chen for allowing me to use the laser and the optical microscope present in the Impact Science Laboratory.

I express my sincere gratitude to Dr. Christopher Gilpin of the Purdue Life Sciences department in obtaining SEM photomicrographs of my specimens. I would also like to thank Nesredin 'Nes' Kedir for coming down to the lab and setting up the laser every time I had to use the laser for specimen ablation. Furthermore, I would like to thank my lab mate, Hashim Hassan for helping me with EIT imaging of my specimen. Without these elements, my project would have never reached completion.

Finally, I would like to thank my lab mates, especially, Julio, Hashim, and Ishan for helping me navigate through research and making my experience at Purdue very memorable.

TABLE OF CONTENTS

LIST OF TABLES

LIST OF FIGURES

LIST OF SYMBOLS

$\delta\sigma$	conductivity change distribution
ϕ	domain voltage
ϕ_{tunnel}	potential barrier height
ϕ_{th}	threshold fluence
ρ	domain resistivity
σ	domain conductivity
τ_l	pulse duration
τ_t	relaxation time
A	inter-nanofiller area
e	charge of an electron
E	energy per pulse
E_A	activation energy
E_l	length of the l^{th} electrode
$F(\sigma)$	forward model electrode voltages
f_{rep}	repetition rate/frequency
h	Planck's constant
$I(r)$	intensity of laser beam at distance r
J	sensitivity matrix
k_B	Boltzmann's constant
L	total number of electrodes
m	mass of an electron
n	outward-pointing normal vector
R_{tunnel}	tunnel resistance
t	inter-nanofiller distance
T_{st}	stationary temperature
v_0	velocity of ablation front
V_l	voltage on the l^{th} electrode
w	width of laser spot

w_0	width of laser focus where laser intensity is I_0/e
x	position vector
z_l	contact impedance between l^{th} electrode and the domain

ABBREVIATIONS

AC	alternating current
AE	acoustic emission
BPH	benign prostate hyperplasia
CB	carbon black
CEM	complete electrode model
CNF	carbon nanofiller/nanofiber
CNT	carbon nanotube
CW	continuous wave
DC	direct current
DPSS	diode-pumped solid state
EIT	electrical impedance tomography
ERT	electrical resistance tomography
FRC	fiber reinforced composite
FWHM	full width half-maximum
GFRC	glass fiber reinforced composite
HELWS	high-energy laser weapon system
IPL	intense pulsed light
IR	infra-red
LASER	light amplification by stimulated emission of radiation
LASIK	laser-assisted in-situ keratomileusis
LDEW	laser directed energy weapon
MPE	multi-photon excitation
MWCNT	multi-walled carbon nanotube
NIR	near infra-red
PC	polycarbonate
PLA	pulsed laser ablation
PRK	photo-refractive keratectomy
PZT	lead zirconia titanate

RC	resistive-capacitive
SEM	scanning electron microscope
SHM	structural health monitoring
SPE	single-photon excitation
UV	ultra-violet

ABSTRACT

Laser-to-composite interactions are becoming increasingly common in diverse applications such as diagnostics, fabrication and machining, and weapons systems. Lasers are capable of not only performing non-contact diagnostics, but also inducing seemingly imperceptible structural damage to materials. In safety-critical venues like aerospace, automotive, and civil infrastructure where composites are playing an increasingly prominent role, it is desirable to have means of sensing laser exposure on a composite material. Self-sensing materials may be a powerful method of addressing this need. Herein, we present an exploratory study on the potential of using changes in electrical measurements as a way of detecting laser exposure to a carbon nanofiber (CNF)-modified glass fiber/epoxy laminate. CNFs were dispersed in liquid epoxy resin prior to laminate fabrication via hand layup. The dispersed CNFs form a three-dimensional conductive network which allows for electrical measurements to be taken from the traditionally insulating glass fiber/epoxy material system. It is expected that damage to the network will disrupt the electrical pathways, thereby causing the material to exhibit slightly higher resistance. To test laser sensing capabilities, a resistance baseline of the CNF-modified glass fiber/epoxy specimens was first established before laser exposure. These specimens were then exposed to an infra-red laser operating at 1064 nm, 35 kHz, and pulse duration of 8 ns. The specimens were irradiated for a total of 20 seconds (4 exposures each at 5 seconds). The resistances of the specimens were then measured again post-ablation. In this study, it was found that for 1.0 wt.% CNF by weight the average resistance increased by about 18 percent. However, this values varied for specimens with different weight fractions. This established that the laser was indeed causing damage to the specimen sufficient to evoke a change in electrical properties. In order to expand on this result, electrical impedance tomography (EIT) was employed for localization of laser exposures of 1, 3, and 5 seconds on a larger specimen, a 3.25" square plate. EIT was used to measure the changes in conductivity after each exposure. EIT was not only successful in detecting damage that was virtually imperceptible to the human-eye, but it also accurately localized the exposure sites. The post-ablation conductivity of the exposure sites decreased in a manner that was comparable to the resistance increase obtained during

prior testing. Based on this preliminary study, this research could lead to the development of a real-time exposure detection and tracking system for the measurement, fabrication, and defense industries.

1. INTRODUCTION

1.1 Introduction to Composite Materials

Composite materials have been used in various industrial applications for several decades now. Ever since the introduction of glass fibers in the 1930s [1], these materials have been gradually phasing out the use of their traditional engineering material counterparts for a variety of reasons. World War II saw the rise in use of composites when metal shortages came up. Yet another issue with metal-clad military aircraft was the high weight of the vehicle itself, which reduced cargo-carrying capabilities. As a result of their superior mechanical properties, relatively good machinability, and easy manufacturing as compared to conventional materials, composite materials have been an integral part of the automotive, aerospace, defense, and the civil industry. Composites comprise of two or more phases – usually the fiber and the matrix. The fibers reinforce the composite by providing high specific strength and stiffness while the matrix gives the composite shape and influences the service temperature, environmental conditions, and manufacturing process [1].

There are a variety of fibers that could be used for reinforcing a composite, e.g., carbon, glass, aramid, boron, aluminum, etc. Depending on its composition, the matrix may be sub-divided into one of the three categories – metal matrix, ceramic matrix, or polymer matrix. Metal matrix composites offer various advantages that include but are not limited to high temperature usage, high transverse strength, high toughness, and thermal conductivity. However, they are susceptible to interfacial degradation at the fiber-matrix interfaces and also to corrosion. Ceramic matrix composites have applications in extremely high temperature venues (such as the leading edge of the spacecrafts during re-entry [1]), but conversely are expensive and complicated to manufacture. Polymer matrix composites may be further classified as thermoplastic and thermoset polymers and are more commonly used than the metal and ceramic types. Thermoplastics are long, entangled polymer chains which have covalent bonding prevalent in their backbone and secondary bonding between individual chains. They soften upon heating can be re-molded and re-formed by elevation of the temperature. However, these materials have high viscosity during processing. On the other hand, thermosets are liquids with relatively low molecular weights compared to thermoplastics. The

molecules form a polymer network among themselves via covalent bonds. No secondary bonding is present in these materials and they also exhibit low viscosity during material processing [2]. This makes them more suitable than the latter for cost-efficient manufacturing [1]. Most widely used thermoset polymers include epoxies, polyesters, and phenolics. The low-viscosity resin, upon combining with the hardener, undergoes cross-linking to form a high molecular weight polymer solid [3].

1.2 Introduction to Lasers

First developed in 1960 [4], lasers are devices which produce a monochromatic, coherent, and collimated beam of light as a result of stimulation of a lasing medium. The word laser is an acronym derived from Light Amplification by Stimulated Emission of Radiation. Depending on their mode of operation, lasers can be classified into two types – continuous wave and pulsed. A continuous wave (or CW) laser produces a continuous output beam, while a pulsed laser produces an output beam at given repetition rate. A typical laser consists of three major components – a lasing or active medium, an excitation system or pump, and an optical resonator. The lasing medium is a source of optical gain within the laser. It may be solid, liquid, or gaseous depending on the type of laser. The pump produces a population inversion in the lasing medium by either optical, electrical, or chemical means. For lasing to occur, the number of stimulated emissions must be greater than those of spontaneous and absorptive nature. This implies that there are more electrons in an excited state than those in the ground state. As of result of which, the population of atoms in the ground state is 'inverted'. During this process, atoms are excited to a higher quantum-mechanical energy level by the addition of energy provided by the pump [5]. When the atoms return to the ground state, they do so by emitting a photon of the corresponding energy (see Figure 1.1).

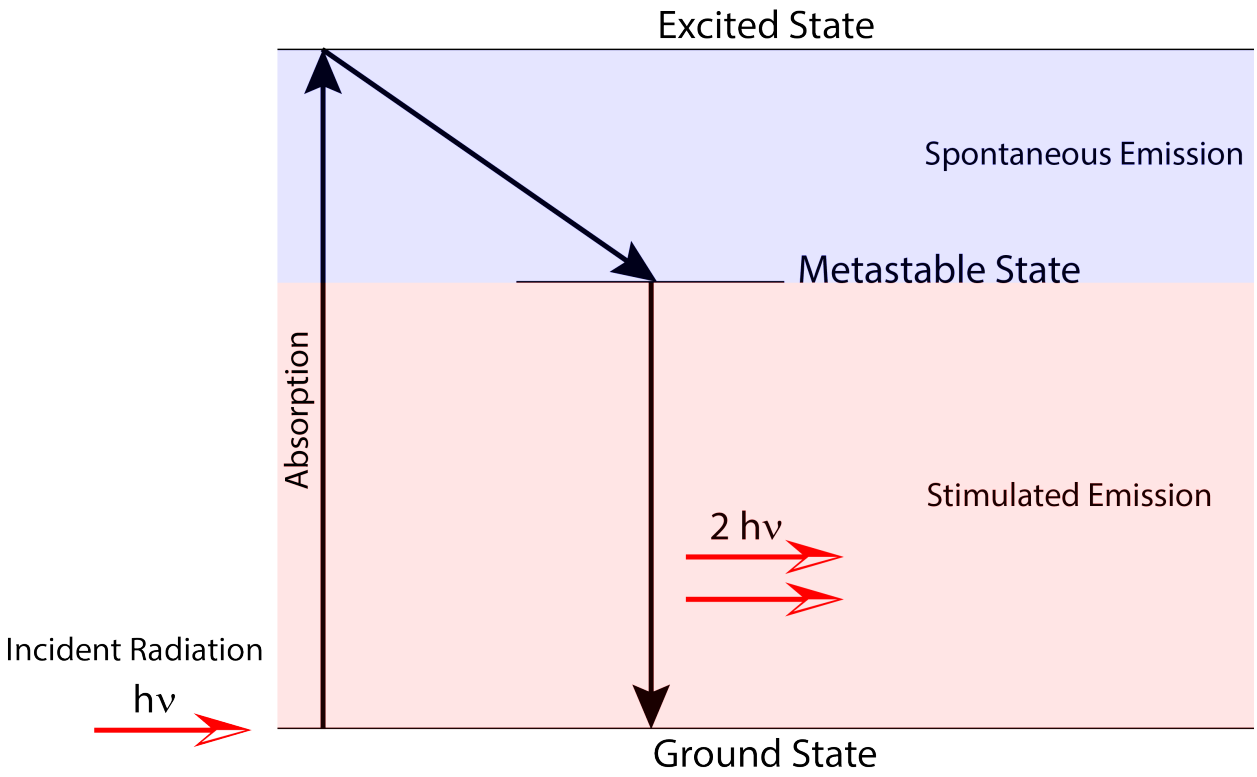

Figure 1.1. Mechanism of absorption and emission of photons during lasing action [5].

The optical resonator cavity consists of an arrangement of mirrors which allows for amplification by increasing the number of stimulated photons. The huge population of photons travel along the axis of the laser within the optical cavity, while some of it exits the cavity through a partially transmitting mirror in the form of the output beam.

As a result of having a diverse range of output power, lasers are used in a variety of applications in numerous fields [6]. They are capable of output powers which range from a few milliwatts (10^{-3} W) in CD/DVD readers to several kilowatts (10^{3} W) in material processes which include but are not limited to cutting, brazing, welding, etc. for CW lasers. A peak pulse power of up to several petawatts (10^{15} W) for pulsed lasers (such as the Texas Petawatt Laser [7]) can be used in the study of exotic states of matter. Lasers are capable of emitting these photons in a plethora of frequencies across the electromagnetic spectrum, and hence are very versatile and suitable for a suite of applications in industries like communication, diagnostic sciences, atomic physics, medicine, manufacturing, entertainment and even the military.

Lasers are also increasingly replacing radio waves as a means of communication. Usually operating in the infra-red (IR) regime of the spectrum for communication purposes, lasers hold the edge over radio waves in terms of data transfer rate. Radio waves exhibit transfer rates over a few mega bits per second, whereas lasers have reported transfer rates of several gigabits per second. With their advent, lasers have slowly made their way into extra-terrestrial communications. Satellite constellations which aim to connect even the most remote places on Earth to the internet would not be possible without lasers.

Diagnostics tools are extensively used for studying phenomena in combustion chemistry [8]. These reactions take place on an order of a few picoseconds to few microseconds. Using lasers, it possible to provide a high spatio-temporal resolution of the reacting species, which is instrumental in understanding the chemical kinetics of reactions. Being non-contact in nature, these tools do not disrupt the flow field and hence allow for accurate measurements of parameters like velocity, temperature, and concentration of species.

In the world of modern medicine, lasers have proved themselves to be excellent diagnostic, therapeutic, and surgical tools [9]. Ophthalmological surgeries like laser-assisted in-situ keratomileusis (or LASIK) and photorefractive keratectomy (or PRK) utilize the power of UV photons to reshape the tissue via ablation [10]. Over the past two decades, LASIK eye corrective surgeries have had 95.4% overall patient satisfaction, according to a recent meta-analysis [11]. Dermatological treatments such as skin resurfacing (CO_2 and Er:YAG lasers) [12], skin disorder treatment [13] (Q-switched Ruby (694 nm), Alexandrite (755 nm), and Nd:YAG (1064 nm)), photoepilation and tattoo removal [14] (Ruby, Alexandrite, semiconductor diode (800-810 nm), flash lamp-based intense pulsed light (IPL) (550-1200 nm)) harness the power of IR and near infra-red (NIR) photons (either in continuous or pulsed form) to achieve the respective results. Benign prostate hyperplasia (or BPH), a benign condition affects about 50% of men by age of 50 and upto 90% older than 80. High-powered holmium lasers are used to ablate the excess tissue [15]. Lithotripsy utilizes Ho:YAG lasers (2100 nm) to destroy kidney stones [16]. Laser-assisted lead extraction use XeCl lasers (308 nm) in extraction of lead wires of cardiac pacemakers and defibrillators from coronary blood vessels [17]. In dentistry, CO_2, Nd:YAG and diode lasers are used for soft-tissue removal, while Er:YAG lasers are used for hard-tissue removal [18], [19].

In the field of atomic physics, recent advancements at Max Planck Gesselschaft [20], Berlin aim to not only generate but also control attosecond (10^{-18} s) pulses ranging from hard X-rays to IR regime of the light spectrum. This would help researchers to not only study electronic behavior, but also control them by forcing chemical reactions to follow a certain path. Attosecond pulses make it possible to control the behavior of electrons, hence the concomitant properties of a material [21]. Figure 1.2 shows the distribution of petawatt lasers in the world, signifying the shift towards the advancement in this research. The development of electronics which function at terahertz scale, rather than at the current microwave frequency of a few gigahertz would bring about a change in the state of processors which function 10,000 times faster than the current state-of-the-art processors [21]. Krishnamurthy et al (2015) [22] show the generation of hard X-rays from E. coli bacteria by exposing them to femtosecond pulsed lasers. Figure 1.3 shows the electron density, temperature, and plasma frequency of plasma generated by lasers, which is used to recreate dense matter interactions to understand the behavior of relativistic electrons [23].

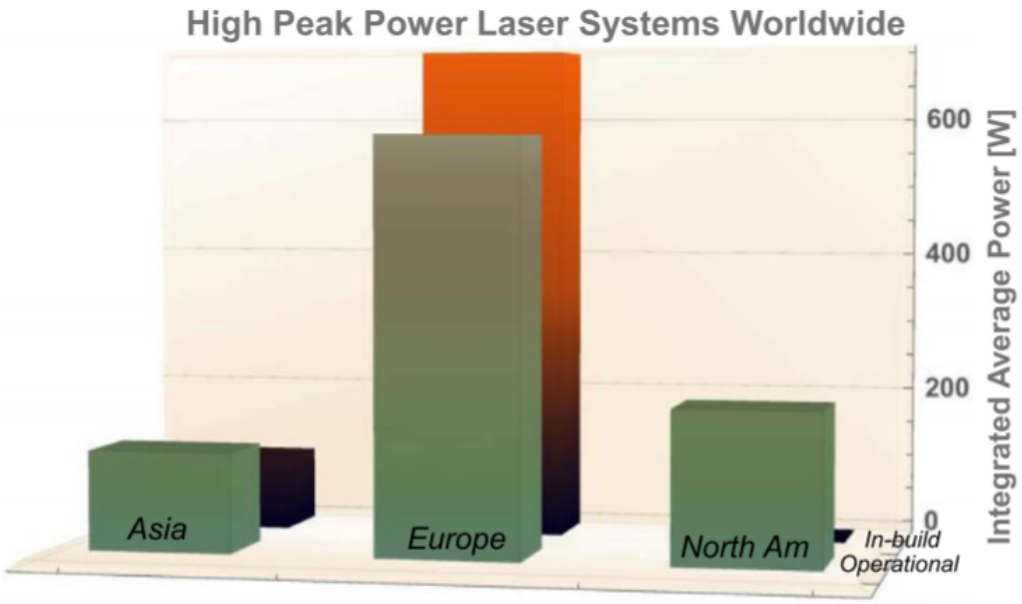

	Asia	Europe	North Am
Operational	140	579	213
In-build	103	696	0

Figure 1.2. Distribution of petawatt (>0.1 PW) lasers in the world [24].

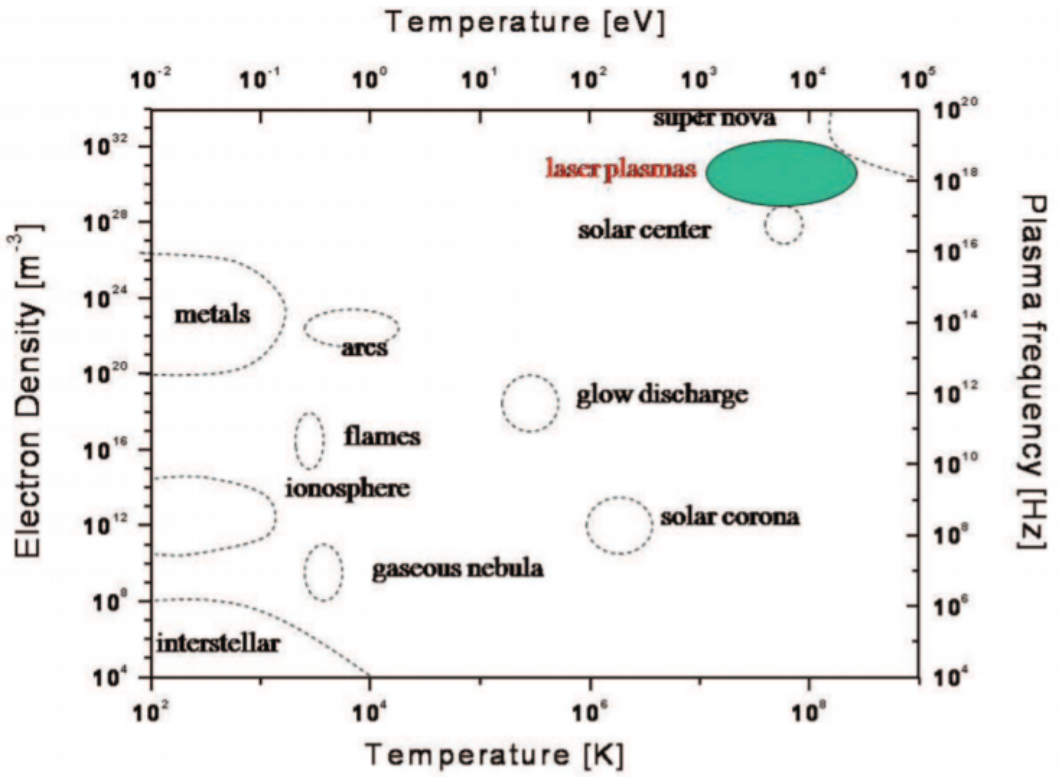

Figure 1.3. Comparison of laser-generated plasma with natural and artificial plasma in terms of electron density, temperature, and plasma frequency[23].

With the emergence of additive manufacturing technologies like stereolithography, laminated object manufacturing, and selective laser sintering, lasers slowly made their way into the manufacturing industry. Today, this industry employs lasers for not only additive manufacturing applications, but also for material processing like machining, engraving, welding, and brazing of metals. Recent advancements in these fields have allowed the automotive and aerospace industry to produce lightweight, yet strong components. Introduced in mid-2015, the Airbus A350 XWB included over a thousand components manufactured by 3D printing [25]. General Electrical Aviation additive-manufactured a helicopter engine by replacing 900 conventional parts with only 16 3D-printed parts. The printed parts were claimed to be 40 percent lighter and 60 percent cheaper than the traditional counterparts [26]. Thus, there is strong precedent for future manufacturing advances centered around lasers.

First depicted in *Goldfinger* (1964), just a few years after their development, lasers have been used heavily in the entertainment industry. Today, lasers are widely used in concerts,

full-color vector-drawn graphics on sides of skyscrapers, and even project three-dimensional holograms in fog [27]. The development of discs to store data in the form of Compact Discs (read/written at 780 nm), Digital Virtual Disc (read/written at 650 nm), and Blu-Ray Discs (read/written at 405 nm) utilize the ability of lasers to store data in 'pits' on the surface of the optical discs [28].

Laser-based weaponry in modern warfare such as the US Air Force's High-Energy Laser Weapon System (HELWS) [29] with over 4000 operational hours since its introduction in 2019 or the UK's Dragonfire Laser Directed Energy Weapon (LDEW) [30] shed light on the development of the emerging technologies on the armed forces front which utilize lasers as weapons. Although they may be expensive to build, the relatively inexpensive operation of lasers (powered solely by electricity) is slowly transitioning to them being the weapon of choice for various armies around the world. It is important to have means of sensing the damage caused by such weapons.

1.3 Introduction to Laser-Polymer Interactions

As described in the §1.2, a plethora of applications involve the usage of lasers. Laser-polymer interactions in venues like rapid manufacturing [31], [32], machining [33], [34], and surface treatment and microstructuring [35] involve optical energy transfer. The energy transmitted by the laser may interact with the material and could possibly bring about undesirable changes. Understanding the effect of laser exposure on polymeric materials is therefore both interesting and important.

Laser pulses operated at high intensities have the ability to cause removal of material at the site of action. This phenomenon is referred to as pulsed laser ablation (PLA) and it occurs when the photon intensity is greater than the threshold value of the material, which is the value of photon intensity above which the material will undergo photo-ablation [36]. This value depends on the optical properties of the material, laser wavelength, and the pulse duration. The process of thermal excitation, which results in PLA, commences with photon excitation [36]. This may be either by single-photon excitation (SPE) mode or a multi-photon excitation (MPE) mode, depending on the type of material. Single-photon

excitation can be defined as the excitation process of an atom by a single photon. In general, electrons prefer to be at a lower (ground) state of energy rather than the excited state. In order to attain the ground state, they emit a photon and come back to the ground state. In case of an electron utilizing multiple photons to reach this excited state, it is called multi-photon excitation. If the excitation energy is suddenly transformed to thermal energy, there is a change in the absorption properties of the material which in turn causes a change in the absorbed laser power. It can be said that the absorbed thermal energy and the optical properties of the material are co-dependent. The laser ablation process can be deemed to be thermal-only process if the thermal relaxation time, τ_t, is very short. The presence of surface melting is often driven by thermal processes.

1.3.1 Factors Affecting Rate of Ablation

Besides the type of material on which PLA is carried out, there are various parameters which affect the rate of ablation on the surface of the material. These include but are not limited to photon energy, fluence, pulse length, width of laser focus, heat or optical penetration depth, enthalpy of vaporization, internal stress, and type and pressure of the ambient atmosphere. The more widely studied factors are listed below [36], [37].

[1.] **Photon energy and fluence** – The photon energy is a value dependent on the frequency of light by the relation, $E = h\nu$, usually expressed in eV. Photons with a higher frequency (or shorter wavelength) are more energetic than those with a lower frequency (or longer wavelength). The fluence is defined as the amount of optical energy delivered by the laser per unit area, usually expressed in J/cm^2.

[2.] **Pulse duration** – This parameter is defined for pulsed lasers only. It is defined as the time measured across a pulse at its full width half-maximum (FWHM). It can range from several tens of attoseconds [38] (10^{-18} s) to a few hundred nanoseconds (10^{-9} s).

[3.] **Beam spot size and screening effect** – The beam spot size refers to the beam width at the laser focus. When PLA is carried out for longer duration on a substrate, the formation of a vapor cloud on the ablation site is observed. The vaporized substrate absorbs

a considerable amount of radiation, thereby reducing the amount of energy transmitted to the substrate. This causes the 'shielding' or 'screening' effect.

[4.] **Pulse number** – The pulse number is defined as the number of laser pulses administered to the substrate during an instance of PLA.

In addition to affecting the rate of PLA, these factors also control the various physics-driven effects like heat transfer within the material. This allows for the variation in physical appearance of the ablation site and results in varying degrees of precision when micromachining a material [39].

Photon energy and fluence

In studies conducted by Küper [40] and Arnold et al. [41], the ablation rate of a polyimide substrate as a function of the laser fluence in the UV region of the spectrum was observed (see Figure 1.4).

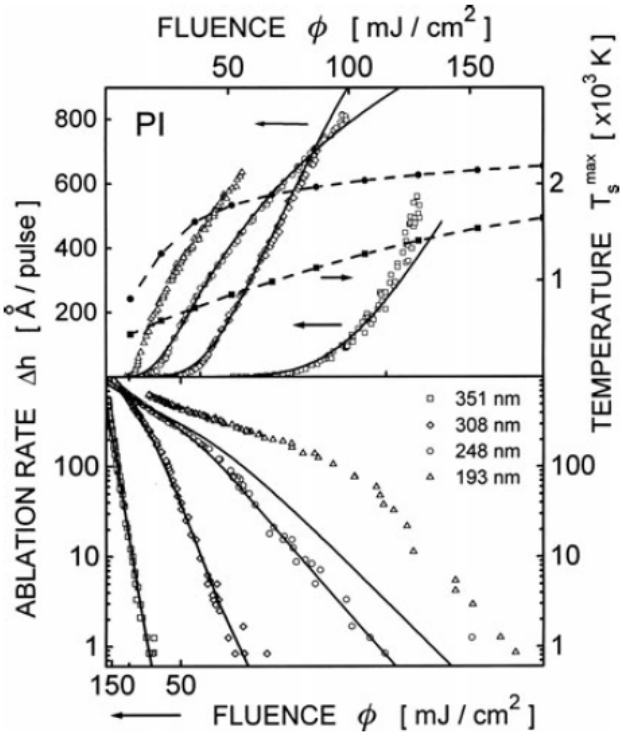

Figure 1.4. Effect of variation of wavelength on ablation rate and temperature as a function of fluence for a polyimide substrate [40], [41].

It was observed that with increasing wavelength (or decreasing frequency) for a given fluence, there was a reduction in the ablation rate due to the decrease in the intrinsic absorption. Figure 1.5 shows that an increase in the laser fluence was accompanied by an increase in the rate of ablation.

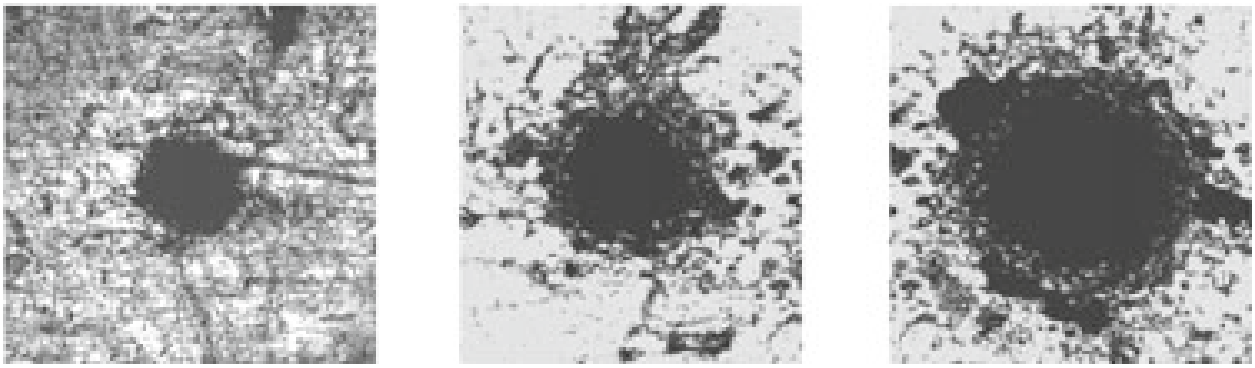

Figure 1.5. Effect of variation of fluence (from (L) to (R) 20, 60, 2000 J/cm^2 respectively) on an aluminum target by nanosecond laser [37].

Pulse duration

In an experiment performed by Himmelbauer [42], the dependence of pulse duration on ablated depth on a polyimide target was observed. It was inferred that for increasing pulse duration with various constant intensities, the threshold frequency, ϕ_{th}, increased correspondingly. The slope of the graph, i.e., the ablation velocity for a more intense pulse was higher than that for a less intense pulse (see Figure 1.7). This experiment also allowed Himmelbauer to compute the activation energy by utilizing the relation between activation energy, E_A and stationary temperature, T_{st} (see Equation 1.1).

$$v \approx v_0 \; exp\left(- \frac{\Delta E_A}{k_B T_{st}} \right) \tag{1.1}$$

In a study conducted by Chichkov et al. [43], the effect of pulse duration in nanosecond, picosecond, and femtosecond laser pulses on a steel substrate was observed. Although this is a different material class than polymers, the effect of pulse duration is better observed in this example. The pulse duration dictates how 'clean' an ablation crater is. As seen in Figure 1.6, it is evident that the specimen irradiated by the nanosecond and picosecond

laser beam there is an absence of 'clean' edges. This leads to the speculation of splashing of molten material during the laser operation. On the contrary, in the specimen irradiated by the femtosecond laser beam there is absence of a crude edge and only a fine vapor ring is present on the periphery of the crater.

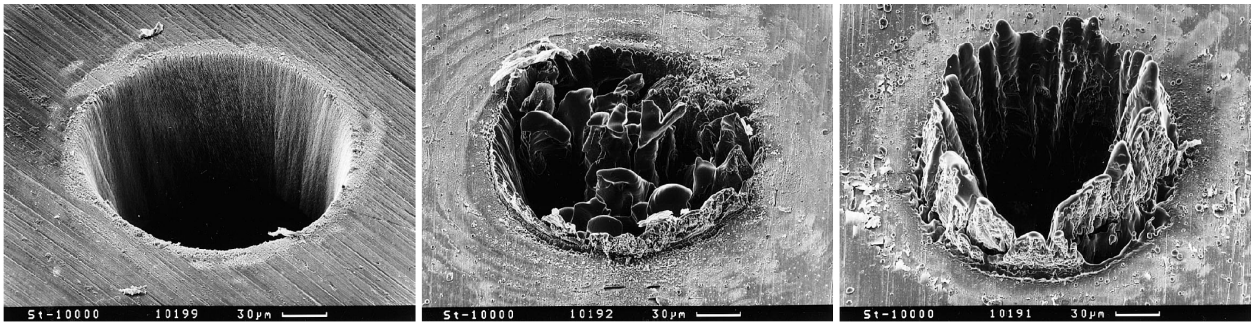

Figure 1.6. Effect of variation of pulse duration ranging from the femtosecond scale (200 fs), to the picosecond scale (80 ps), and the nanosecond scale (3.3 ns) [43].

Besides the pulse duration, the crater geometry fineness is characterized by the laser fluence, especially just above the threshold fluence of 1-10 J/cm^2 for nanosecond pulses (see Figure 1.7).

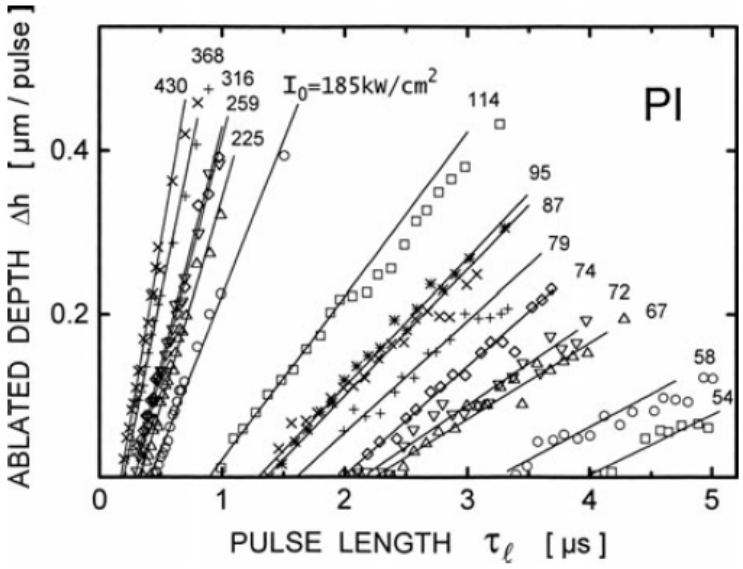

Figure 1.7. Effect of variation of pulse duration with multiple constant intensities on a polyimide target [42].

This can be explained by the varying time scales of heat transfer between the interacting species involved in the process of laser ablation (see Figure 1.8). The recoil pressure created due to the sudden ablation of the material causes the molten material to splash around, thereby forming an irregular geometry. This is avoided in ultra-short laser interactions performed by femtosecond lasers.

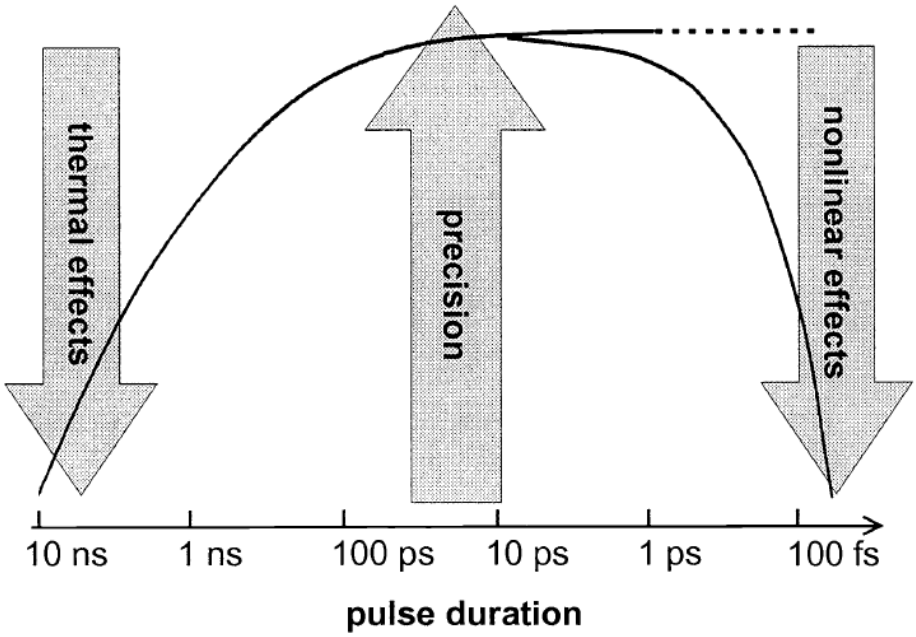

Figure 1.8. Precision as an effect of varying scales of pulse duration [39].

Beam spot size and screening effect

The size of generated pattern and the expansion dynamics of the plasma cloud is determined by the diameter of the laser spot on the material surface. In studies conducted by Wolff-Rottke et al. [44] and Heitz et al. [45], for spot widths much greater than the ablated depths, it was observed that ablation rates were higher for smaller spot widths. Although above the saturation value, the ablation rate became independent of the spot width. When considering nanosecond laser ablation, it is important to take into account the plasma cloud formation due to the longer pulse duration as compared to pico- or femtosecond laser ablation. Plasma shielding effect is seen which affects the absorption characteristics of the substrate material [46].

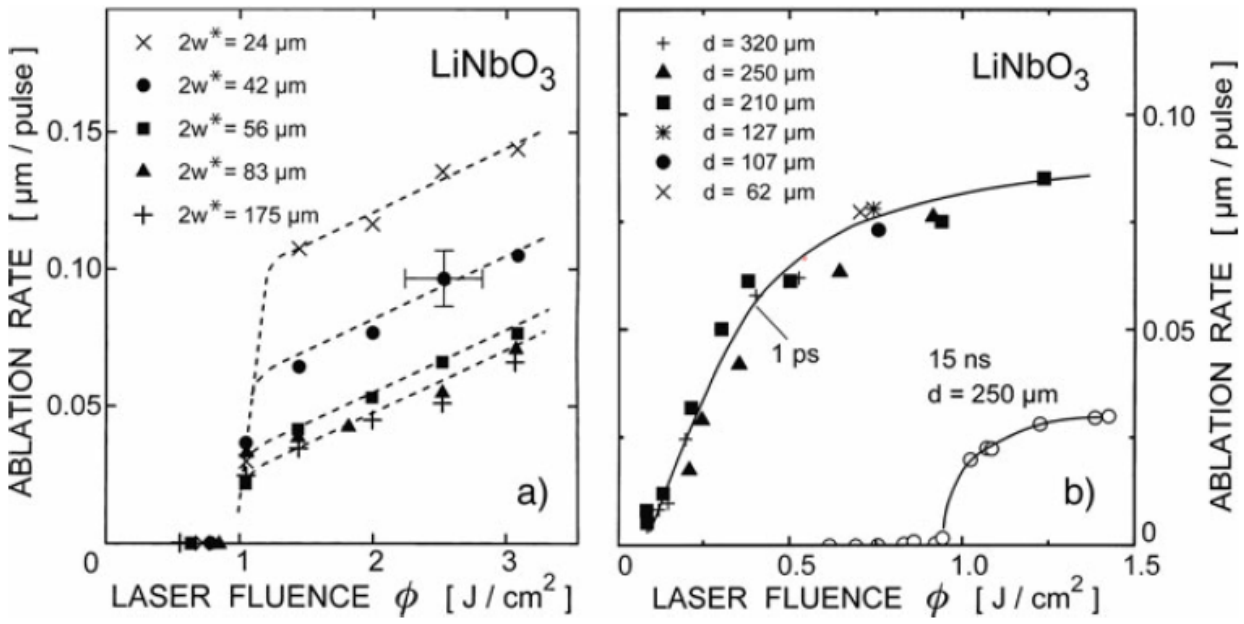

Figure 1.9. Effect of variation of laser spot width on the ablation rate for a $LiNbO_3$ target by an excimer laser (L) [47] and comparison between picosecond and nanosecond laser to exhibit effect of screening (R) [46].

For nanosecond pulses, the ablation rates are higher for smaller spot sizes. Above a 'saturation' value, about 80 μm, the ablation rate becomes independent of the width of laser spot, w. Similar observations were made by Wolff-Rottke [44] and Heitz [45] by using various other materials and longer laser pulses.

Pulse number

As intuitive as it may sound, the ablation depth is directly proportional to the number of laser pulses only for materials that are good absorbers. Good absorbers are opaque and non-reflecting in nature (e.g., an ideal black-body), whereas poor absorbers are often transparent/translucent and reflecting in nature (e.g., plastics) based on Kirchoff's radiation law [48]. This may not hold true for poor absorbing materials, where the material removal could be very slow or even be absent for the first few pulses which would then increase in a linear or a non-linear manner, depending on the thermal absorptive nature of the material. In the findings reported by Srinivasan [49], in nanosecond excimer-laser ablation of various polymers the decrease in the rate of ablation with high number of pulses was attributed

to the loss of energy by heat conduction, which in turn decreased the radiation-induced temperature rise. Figure 1.10 shows the effect of variation of number of pulses in a PZT substrate. This example was included to demonstrate the effect of number of pulses on a solid substrate. This effect became prominent when the ablated depth approached the beam spot width. With increasing depth, the transport of the particulates in the gaseous phase became inefficient and they re-solidified within the cavity itself (see Figure 1.11) [50]. The beam spot size was directly proportional to the depth at which the transport became inefficient.

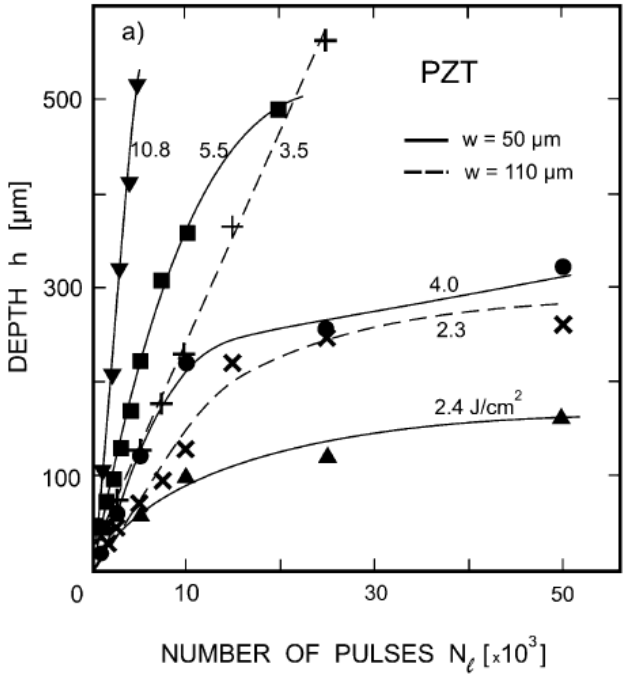

Figure 1.10. Effect of variation of number of pulses for two beam spot widths on the ablated depth of ceramic lead zirconia titanate (PZT) [51].

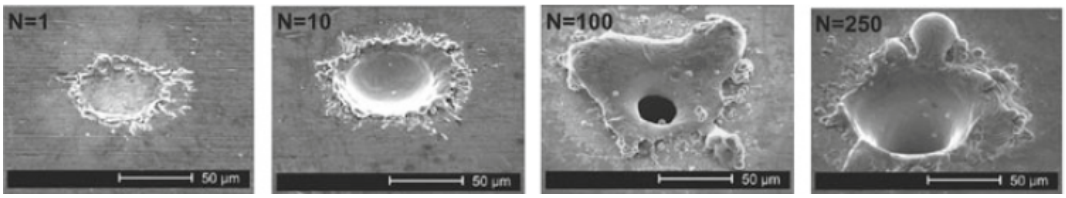

Figure 1.11. Effect of variation of number of pulses (1, 10, 100, and 250 respectively) on the diameter of the ablated zone on a stainless steel target [50].

1.4 Introduction to Self-Sensing Materials

Due to the complex nature of manually assessing the extent of damage in composite materials and the potentially deleterious effect of laser exposure on composites, it is desirable to have some form of structural health monitoring (SHM) for detecting laser exposure in composites. Self-sensing materials may be very promising in this regard. 'Self-sensing' refers to the ability of a material to intrinsically report on its health or condition. A common approach to self-sensing is via the piezoresistive effect. Piezoresistivity is generally used to describe a material that has deformation and damage-dependent electrical conductivity [52]–[58]. However, conductivity changes have been used for detecting non-mechanical effects such as resin infusion in a composite laminate [59], pH exposure [60], and UV exposure [61]. Although a wide variety of materials naturally exhibit some extent of piezoresistivity (e.g. carbon fiber composites, semi-saturated cementitious materials, and soils [62]), nanofiller-modification has received much attention in this regard in recent decades. In this approach, a non-conductive material such as a polymer matrix is modified with conductive nanofillers such as carbon nanotubes (CNTs), CNFs, or carbon black (CB). The intent is to add sufficiently many conductive fillers for an electrically connected (i.e., percolated) network to form, which allows electricity to propagate through the material along the conductive filler network. Effects that alter the connectivity of the network therefore manifest as conductivity changes. For example, deformations may alter the spacing of the fillers thereby making it easier or more difficult for current to flow in the vicinity of the deformation. Because it is generally desirable to minimize the relative concentration of conductive fillers in the host material (due to cost and to minimize the fillers degrading the mechanical properties of the host material), fillers such as CNTs are commonly used because their ultra-high aspect ratio allows for electrical percolation at low filler weight fractions [63]–[65].

Herein, it is hypothesized that laser exposure-induced ablation will likewise cause a conductivity change in conductive filler-modified polymers thereby allowing for intrinsic self-sensing of lasers in these materials. To better understand this hypothesis, it is necessary to better understand the mechanism by which electricity is conducted in a conductive nanofiller-modified polymer system. For direct current (DC) transport, the nanofillers act as one-

dimensional conduits of electricity – like a resistor. Networks of high-aspect ratio fillers (e.g., CNTs and CNFs) are therefore often modeled as equivalent resistor networks [66]. Often, the fillers are not physically touching each other. Transport between sufficiently proximate fillers is therefore achieved via electrons 'jumping' between fillers. That is, via quantum tunneling [67], [68]. The equivalent resistance felt by a tunneling electron is well-approximated via Simmons' equation as shown in Equation 1.2.

$$R_{\text{tunnel}} = \frac{h^2 t}{A e^2 \sqrt{2m\phi_{\text{tunnel}}}} \exp\left(\frac{4\pi t}{h}\sqrt{2m\phi_{\text{tunnel}}}\right) \tag{1.2}$$

In Equation 1.2, h is Planck's constant, t is the inter-nanofiller distance, A is the area between the nanofillers, e is the charge of an electron, m is the mass of an electron, and ϕ_{tunnel} is the potential barrier height between the nanofillers. Thus, two possible manifestations of the piezoresistive effect are changing inter-filler distance (i.e., changing t) and changing inter-filler barrier height (i.e., changing ϕ_{tunnel}).

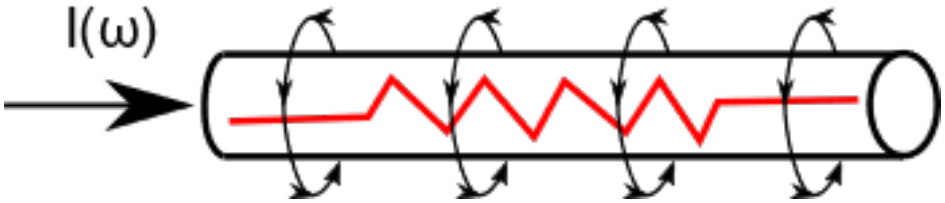

(a) Current flowing through a conductive nanofiller in the fiber direction.

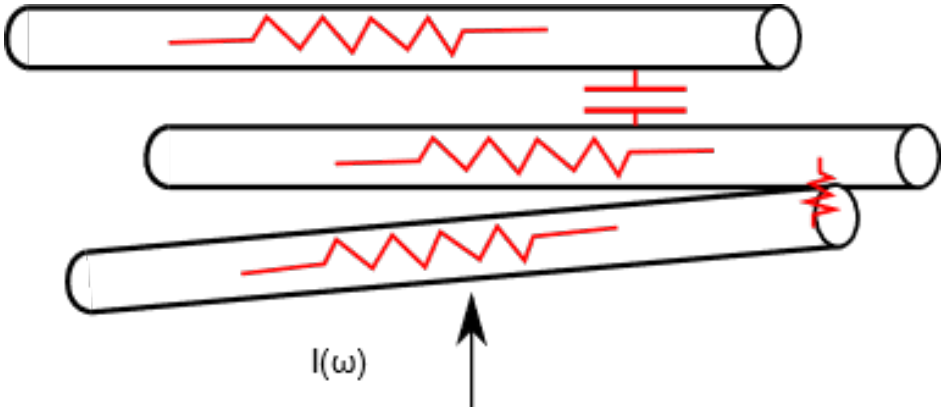

(b) Current flowing through a conductive nanofiller in the transverse direction.

Figure 1.12. Inductive, capacitive, and resistive behavior of conductive nanofillers [69].

Depending on the distribution and arrangement of the conductive nanofillers, alternating current (AC) can flow through various modes ranging from resistive, inductive, capacitive, and even in combinations of these factors [70], [71]. The distance between the nanofillers dictates the mode of current flow through them (see Figure 1.13); when in direct contact, inter-filler transport is akin to DC transport as in the contact impedance acts like a resistor. When the nanofillers are not in contact but are in the quantum tunneling range, the transport can occur in a parallel-RC (resistive-capacitive) mode. Beyond the quantum tunneling range but within the capacitive coupling range, capacitive coupling connects the nanofillers with a single capacitor. Nanofillers outside the capacitive range do not interact with other nanofillers.

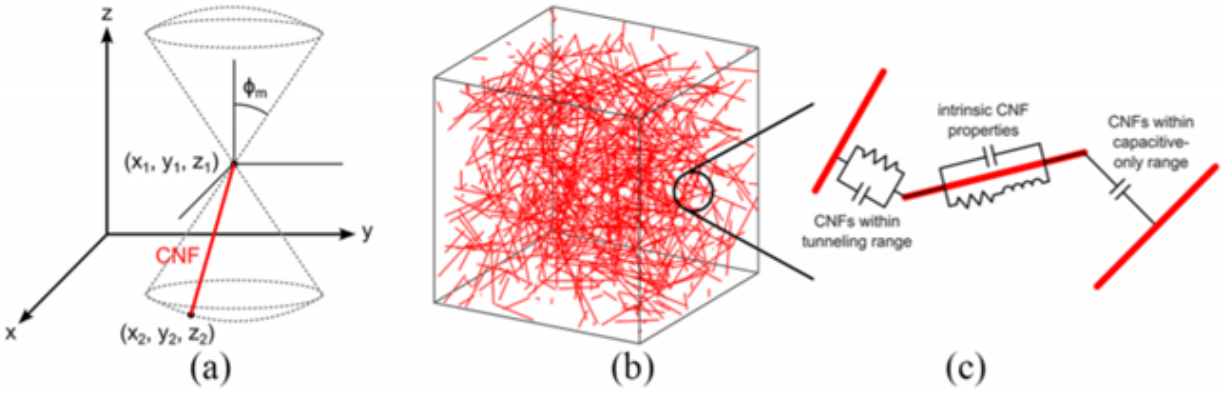

Figure 1.13. AC transport in CNF depending on the inter-nanofiller distance [71].

MWCNT-modified composites have been extensively studied for their strain-sensing capabilities. For example, Parmar et al. [53] investigated the effect of CNT alignment on the strain-sensing ability of MWCNT/polycarbonate (PC) composites. It was found that injection-molded composites resulted in a higher MWCNT alignment than compression-molded alignment. As a result of which, the former exhibited a higher gage factor than the latter (see Figure 1.14).

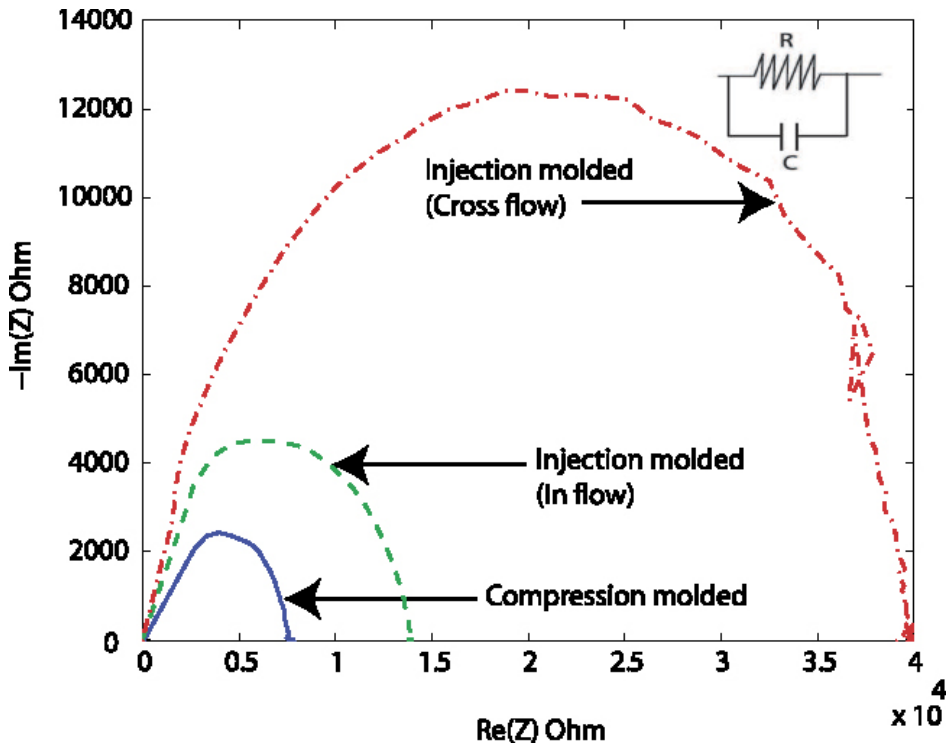

Figure 1.14. Comparison between the compression molded and injection molded (in-flow and cross-flow) composites [53].

In another study conducted by Nofar et al. [52] MWCNTs were used to determine the failure location in MWCNT/GFRC tabs with artificial cracks. They proved to be more sensitive than traditional strain gages in identifying the crack location. This theory was bolstered by the fatigue results of both crack-initiated samples and samples without cracks. The MWCNT network is spread throughout the matrix, whereas the strain gages are present at discrete locations only. This allows the network to detect minute deformations or crack propagation more easily than strain gages (see Figure 1.15) [52].

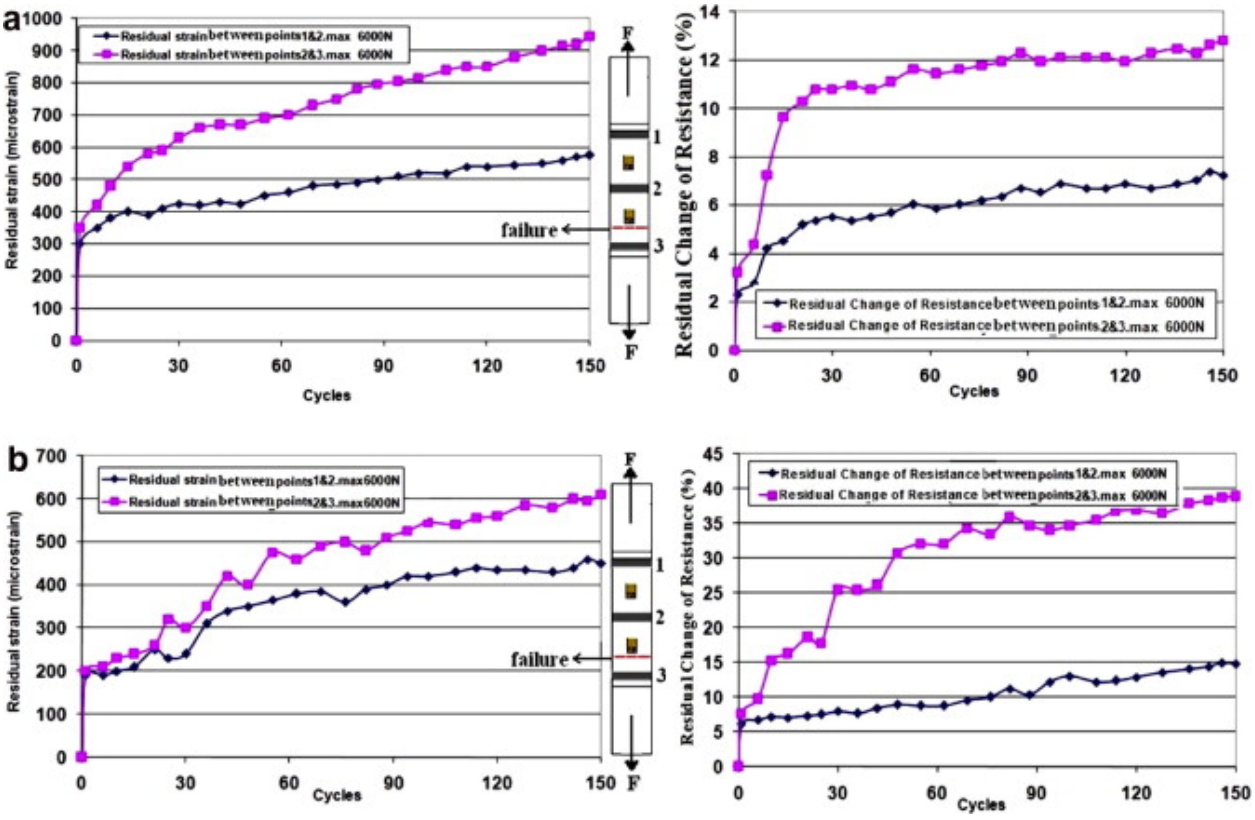

Figure 1.15. Residual change in resistance proportional to strain in MWCNT-GFRC composites [52].

Gao et al. [55] investigated the rise in electrical resistance in laminates manufactured with CNT-modified epoxy due to repeated impact loading. The author was able to correlate the resistance change, absorbed energy, acoustic emission (AE) counts, and damage area of the composite (see Figure 1.16a). In a separate experiment, Gao et al. [54] were able to detect damage due to incremental cyclic tensile loading of modified GFRC laminates. As a result of increasing amounts of damage, a permanent change in resistance was observed (see Figure 1.16b).

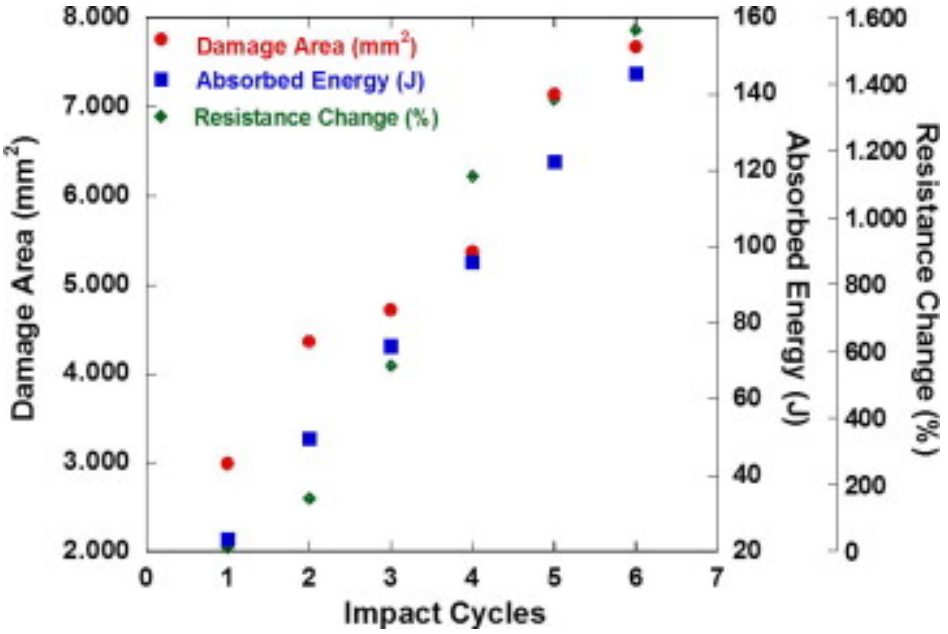

(a) Resistance change in specimen after cyclic impact loading [55].

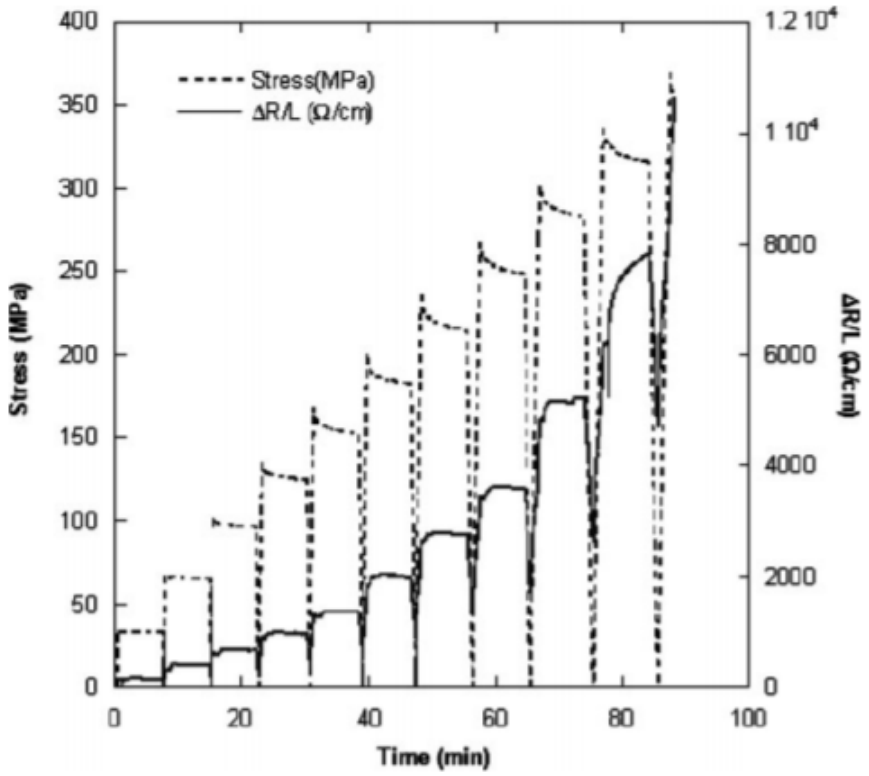

(b) Resistance change in specimen after cyclic tensile loading [54].

Figure 1.16. Resistance changes in CNT-modified composites as a result of physical deformations [54], [55].

Gao et al. [54] utilized CNT's electrical response combined with the AE signals to sense damage initiation and evolution in CNT-modified FRCs. The results showed a bi-linear relationship between the resistance change and AE signal cumulative counts which a better understanding of the damage condition of the material during quasi-static and cyclic testing (see Figure 1.17).

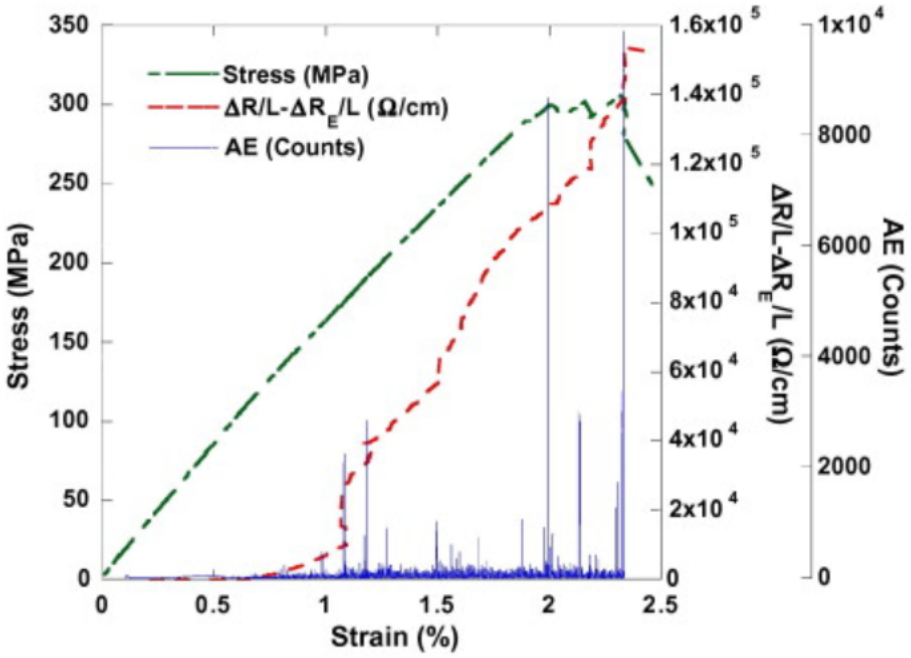

Figure 1.17. Stress, acoustic emission, and resistance change in specimen as a result of deformation [54].

Pandey et al. [58] were able to successfully correlate electric time domain reflectometry (TDR) with the strain and AE measurements to capture the damage state of CNT-based composites. As a result of this study, it was realized that CNTs increase TDR sensitivity to strain and introduce the ability to sense development of micro-scale cracks (see Figure 1.18).

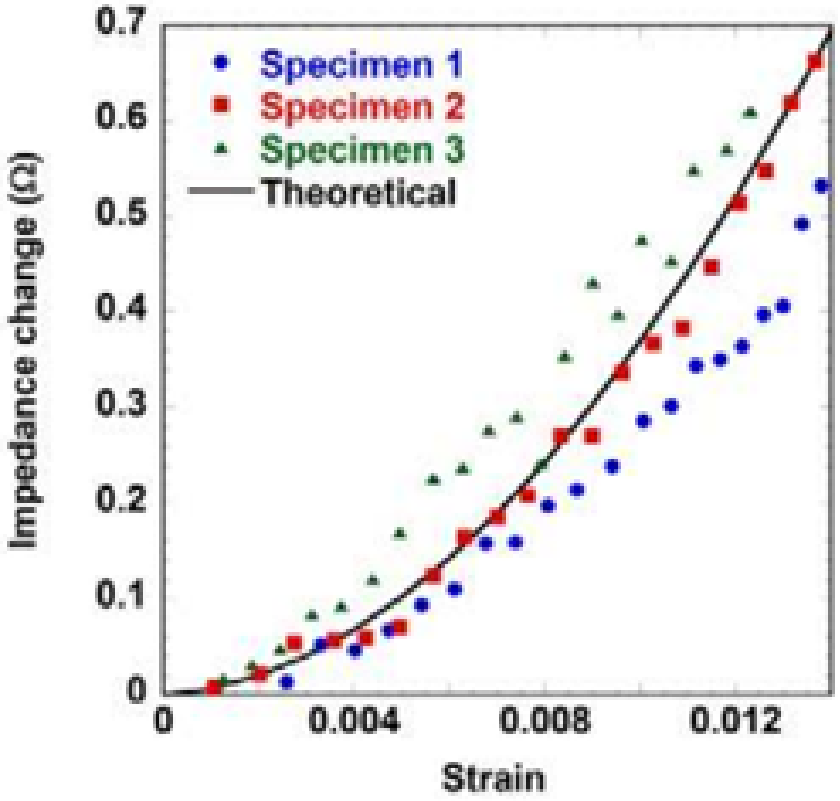

Figure 1.18. Specimen showing proportional rise in impedance with respect to strain [58].

Beyond just detecting the occurrence of some stimulus via piezoresistivity, it is often desirable to spatially locate and shape the deleterious effect. For this, electrical impedance tomography (EIT) has received much attention in combination with self-sensing materials [72]. Summarily, EIT is a method of estimating the internal conductivity distribution of a domain via voltage-current relationships measured at the boundary. As a few representative examples, Loh et al. [73] worked on the development of sensing skins for spatial strain and identification of impact damage. EIT's virtue of generating two-dimensional conductivity mapping enabled the authors to identify deformation and cracking induced by an impact apparatus (see Figure 1.19). Loyola et al. [74] also demonstrated the spatial sensing of spray-coated CNT-GFRP composites. Tallman et al. [56] showed the resolution of EIT on a CNF-modified GFRC with pre-damaged through-holes in the specimen. EIT successfully mapped the two-dimensional conductivity distribution and revealed the damage state of the

specimen (see Figure 1.20). And lastly, EIT-based conductivity mapping is not restricted to planar specimens only; Thomas et al. [57] have shown the successfully damage detection via EIT in cylindrical specimens (see Figure 1.21). The damage was induced in the composite tubes by drilling holes of various diameters, and impact testing. These examples show how EIT can be used for continuous imaging of conductivity changes in self-sensing materials.

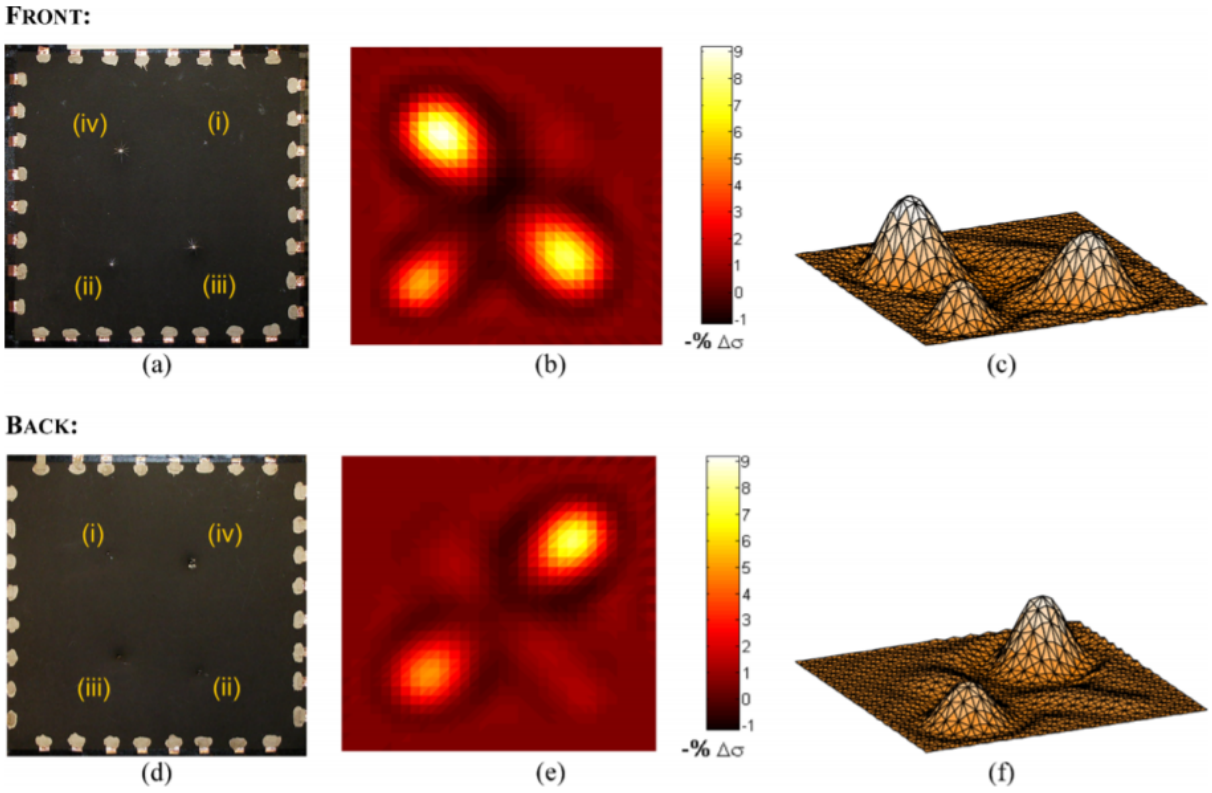

Figure 1.19. EIT reconstruction of impact damage on sensing skins [73].

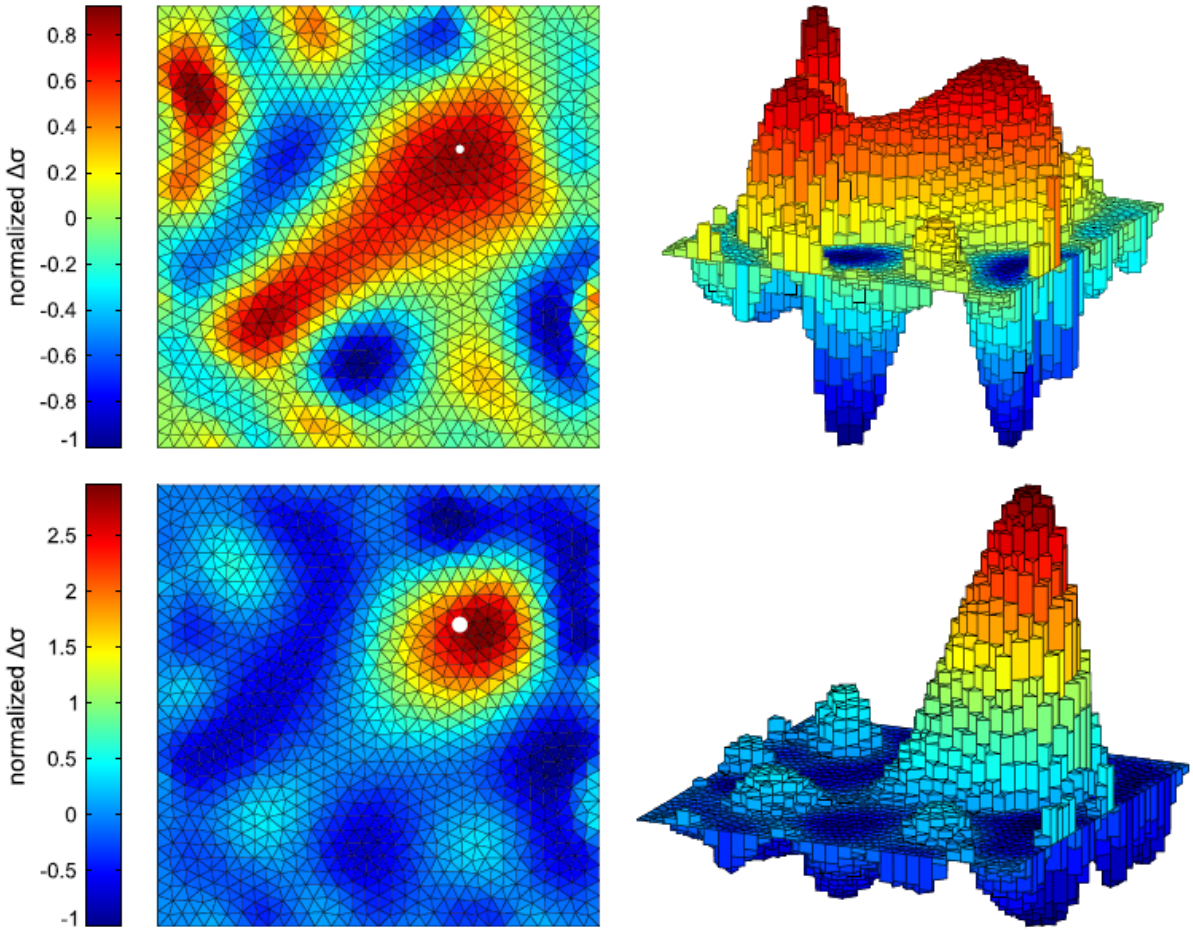

Figure 1.20. Reconstruction of through-hole damage in composite plate via EIT [56].

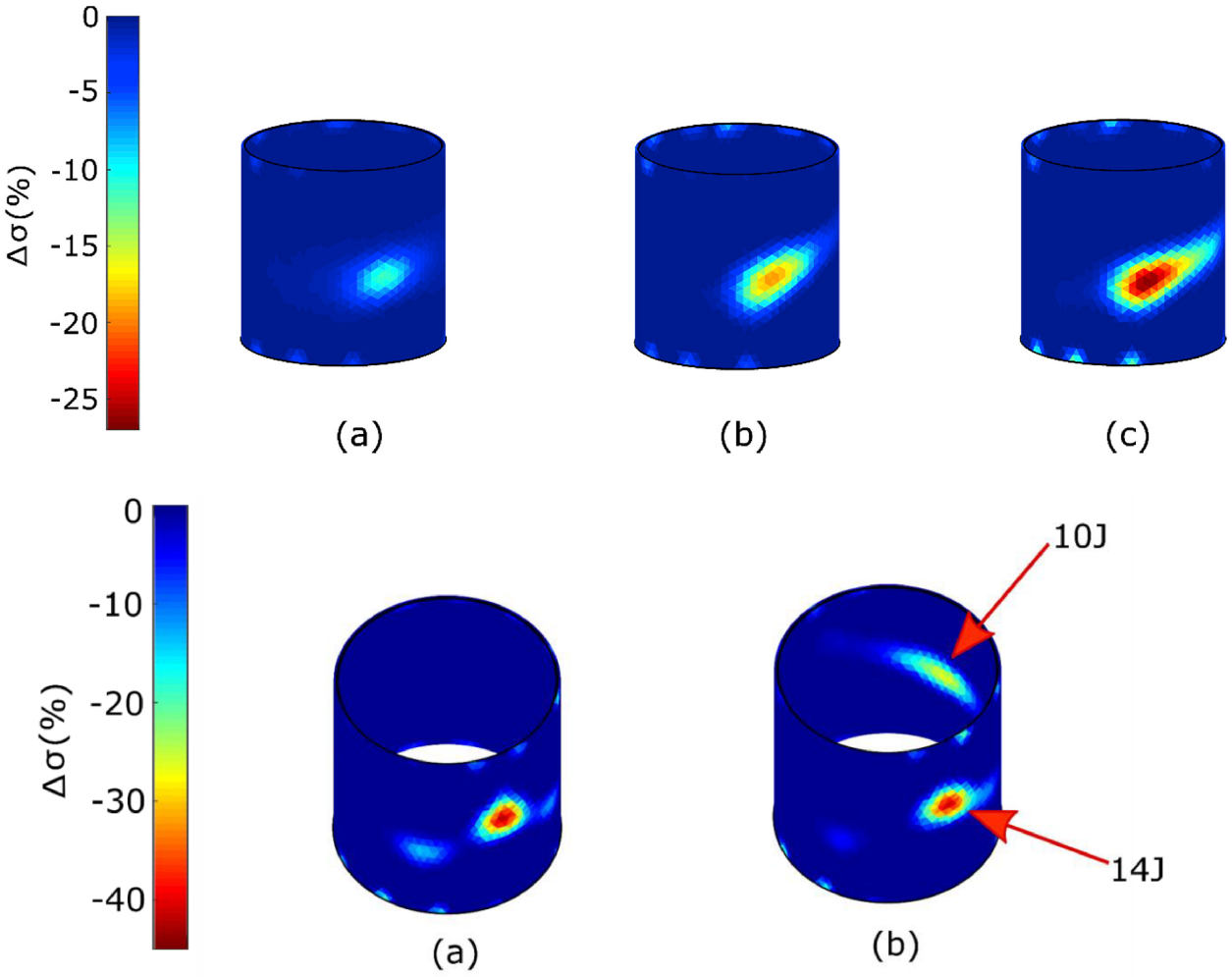

Figure 1.21. EIT mapping of conductivity showing impact location on cylindrical composite tube [57].

EIT-based conductivity mapping is also not limited to the imaging of mechanical effects. As a few representative examples of non-mechanical sensing via the combination of self-sensing materials and EIT, Dai and Thostenson [59] used EIT to demonstrate spatial flow mapping of epoxy resin in CNT-based textile manufactured by vacuum-assisted resin transfer molding. The sensor electrical response during the elevated temperature cure correlated with the viscosity and gelation of the epoxy resin (see Figure 1.22). Next, Hou et al. [60] investigated the two-dimensional conductivity mapping of CNT composite thin films on their response to various pH stimuli. The study demonstrated conductivity changes in acidic as well as basic environments (ranging from pH 5 through 9) (see Figure 1.23). The con-

ductivity measured by this method lay within 2% than those measured by two-point probe technique, thereby displaying a strong agreement between the two methods. And as a final example, Clausi et al. [61] demonstrated the use of electrical resistance tomography (ERT) to investigate the changes in surface electrical properties of UV-sensitive nanocomposite films upon exposure to UV-C (254 nm) radiation. The study showed change in conductivity of the material subject to the intensity of the UV radiation (see Figure 1.24).

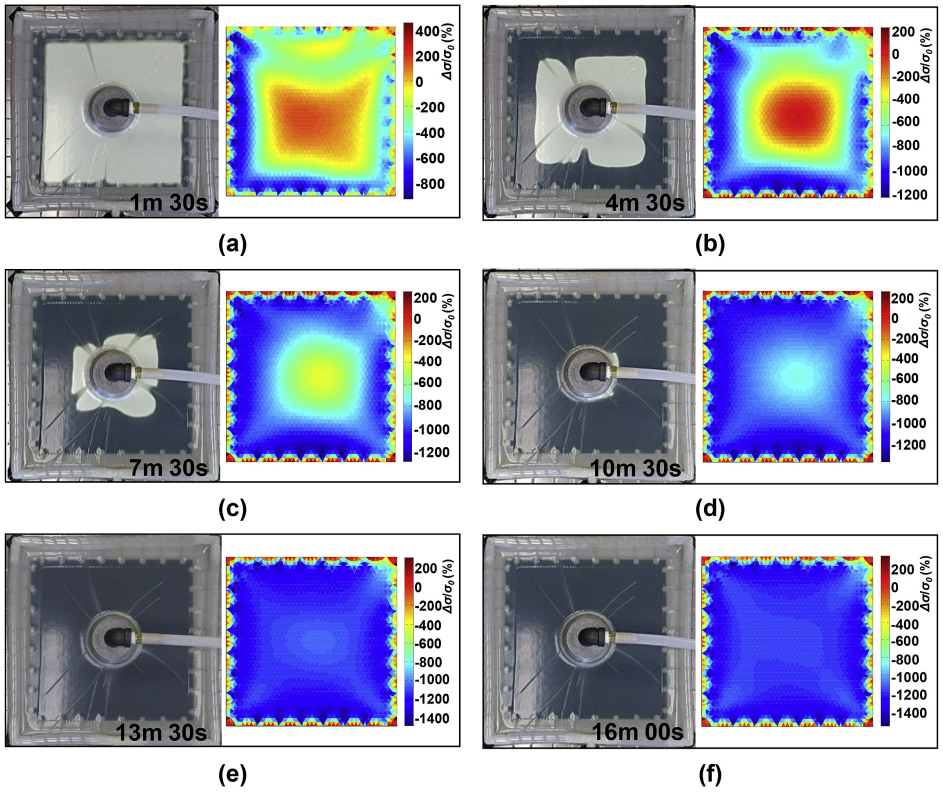

Figure 1.22. Changes in conductivity observed during resin infusion [59].

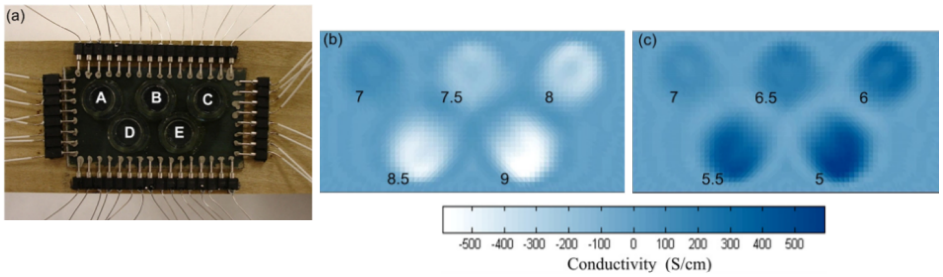

Figure 1.23. Changes in spatial conductivity on $(SWNT\text{-}PSS/PANI)_{100}$ films in basic and acidic environments [60].

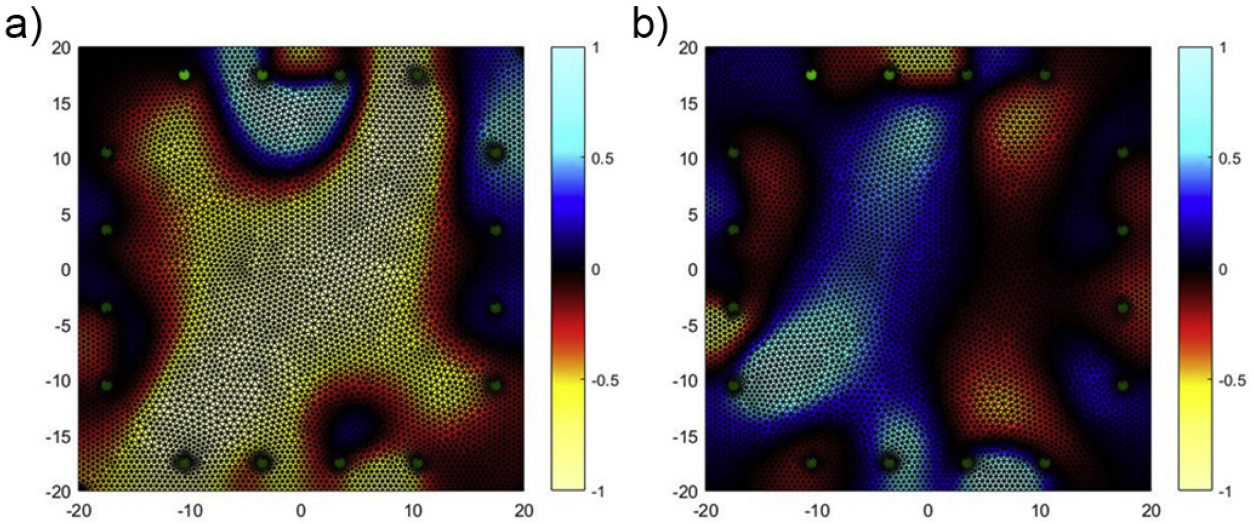

Figure 1.24. Effects of varying UV-C fluence (2.6 mW/cm^2) (L) and (4.0 mW/cm^2) (R) on surface conductivity of GNP/DNA/PEDOT:PSS films [61].

2. PROBLEM STATEMENT AND RESEARCH GOAL

2.1 Problem Statement

Composites are being increasingly used in a wide range of industries as a result of their excellent properties such as high strength-to-weight ratios, ease of manufacturability, and scalability. Laser-to-composite interactions in venues like rapid manufacturing [31], [32], machining [33], [34], and surface treatment and microstructuring [35] involve optical energy transfer and are likewise becoming increasingly common. The energy transmitted by the laser may interact with the material and could possibly bring about undesirable changes. Even with lack of physical contact, lasers are capable of dealing seemingly imperceptible structural damage to materials. It is therefore desirable to have a way to sense such exposure on composite materials. This could be realized with the incorporation of self-sensing materials in such applications. Furthermore, although self-sensing materials have been frequently used to detect strain and identify damage locations and some work has even been done to sense non-mechanical effects (e.g. pH, UV, and infusion), little-to-no research has been done on utilizing these materials to sense laser exposure.

2.2 Research Goal

Motivated by the potential of self-sensing materials for continuous laser sensing, the research goal of this thesis is to establish the feasibility of conductivity changes in CNF-modified GFRC as a mechanism of sensing pulsed laser ablation. More specifically, this study aims to not only detect laser exposure on laminates, but also accurately map the damage site and quantify the damage in terms of conductivity change across the material. This research could potentially benefit applications like material processing and composite-to-laser interactions in military applications, which are sensitive and susceptible to laser radiation.

3. EXPERIMENTAL METHODS

This chapter describes the processes by which self-sensing glass fiber/epoxy laminates were manufactured and the processes by which these materials were tested. Two types of specimens were produced – rectangular strip-like specimens for one-dimensional resistance testing and square plate specimens for two-dimensional conductivity mapping. A total of 30 strips per weight fraction were made at 0.5, 1.0, and 1.5 percent CNFs by weight, and a total of two plates were made at 1.0 percent CNFs by weight.

3.1 Carbon Nanofiller-Modified Glass Fiber/Epoxy Laminate Manufacturing

The composite laminate specimens in this study used CNF (Applied Sciences Pyrograf®III PR-24-XT-HHT [75])-modified epoxy reinforced with glass fiber (FibreGlast® Style 7725 Bi-directional E-Glass) [76]. The PR-24-XT-HHT nanofiller results from the heat-treatment of carbon nanofiber to 3000 °C, which converts the fibers to a highly conductive and completely graphitized form. The average diameter of these fibers is approximately 100 nm, and they have lengths of 30-100 μm [75]. The epoxy is a FibreGlast® System 2000 Laminating Epoxy Resin, which is a mixture consisting of about 98% epoxy resin based mixture and about 2% multifunctional acrylate [77]. The epoxy hardener is a FibreGlast® 2060 Epoxy Hardener, which is composed of modified amine mixture [78]. Epoxy mixtures were made with CNF concentrations of 0.5, 1.0, and 1.5 percent by weight. Weight percentages of CNF greater than 1.5 wt% were avoided due to the increase in viscosity of epoxy mixture at higher concentration of CNFs which makes the manufacturing process much more challenging.

For the preparation of an epoxy mixture for manufacturing a laminate plate, epoxy resin was measured out in a glass beaker. In a fume hood, an appropriate amount of CNF corresponding to the desired weight percent was added carefully to the epoxy. BioWorld Triton X-100 [79] surfactant was added at a 0.76:1 ratio by weight, followed by acetone, with an acetone-to-epoxy ratio by volume of 1:2 [80]). The addition of the surfactant reduces the interfacial and surface tension which allows for better dispersion of the CNF with the epoxy, while the acetone helps lower the viscosity of the mixture. This mixture was stirred by hand for five minutes before transferring it to a planetary centrifugal mixer (Thinky AR-100)

for five minutes. The resulting mixture was then sonicated in a bath ultrasonicator (Crest Ultrasonics P360) for five hours at 45 kHz. For every ten additional grams of epoxy resin, the mixture was sonicated for an extra hour. Once sonicated, the mixture was transferred to a glass beaker placed on a heat-assisted magnetic stirrer at 60 °C for 24 hours. This allows the acetone to evaporate, leaving only the CNF/epoxy mixture behind. The mixture was then allowed to cool to room temperature by placing the beaker in cold water. Next, the epoxy hardener was added to the mixture at a weight ratio of 100:27 resin-to-hardener. This was followed by BYK® A-501 [81] air-release additive at a ratio of 0.1–0.5:100 by weight of the air release agent to the combined weight of the epoxy resin and hardener. This addition promotes the removal of air bubbles from the epoxy mixture that can lead to formation of voids in the specimen. Once the air release agent was added, the mixture was degassed in a vacuum chamber at room temperature and 0.1 MPa negative pressure for 30 minutes. The degassing procedure is significant because the majority of the air bubbles incorporated during the epoxy mixture preparation phase are removed here. While the epoxy mixture was degassing, the vacuum bag assembly was prepared for the manufacturing of the laminate. Figure 3.1 shows the cross-sectional view of the vacuum bag assembly. Once the vacuum bag was checked for any stray air leaks, the build plate was transferred to an oven and cured at 60 °C for five hours. Upon curing, the plate was allowed to cool to room temperature and the laminate was removed. The plate was trimmed to a 6"×6" square using a water-cooled tile saw to remove frayed edges.

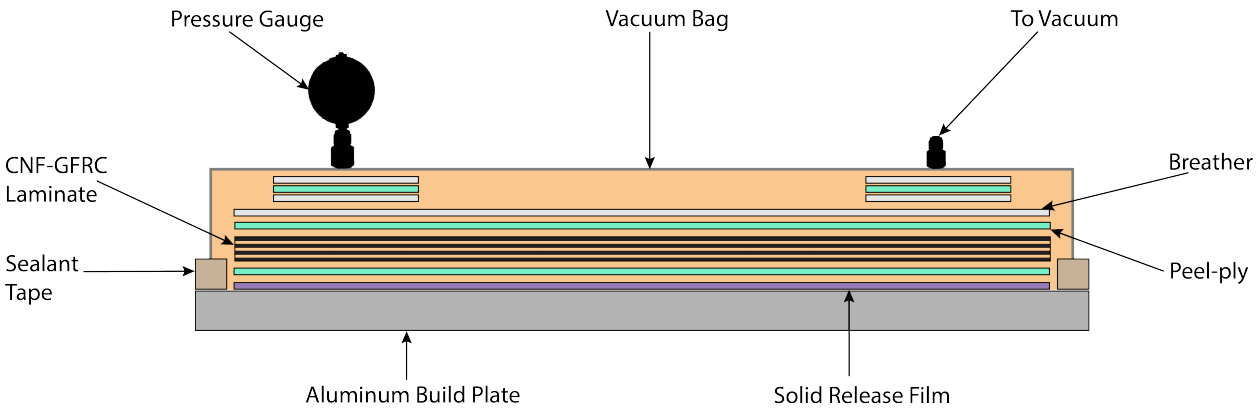

Figure 3.1. Cross-sectional view of the vacuum bag assembly used to manufacture the CNF-modified GFRC laminates.

Following this, the finished laminate was sized down to smaller 1.9"×0.6" rectangles using a water-cooled tile saw. The shorter edges of these specimens were sanded off and cleaned thoroughly with acetone to ensure the edge is smooth and free of grit. The edges were coated with Fast Drying Silver Paint Electrodag 1415M (Ted Pella, Inc., Redding, CA) to allow the specimen to conduct electricity across its length. Once the paint was dry, the shorter side of the specimen was enveloped with 0.25" 3M Copper Tape (Ted Pella, Inc, Redding, CA) so that the specimen could be used to gather electrical data from these copper electrodes. Figure 3.2 shows a representative rectangular strip specimen with the copper tape partly removed to show silver paint applied to the shorter edge of the specimen. A total of thirty test samples per weight fraction (0.5, 1.0, and 1.5 percent) were manufactured and tested.

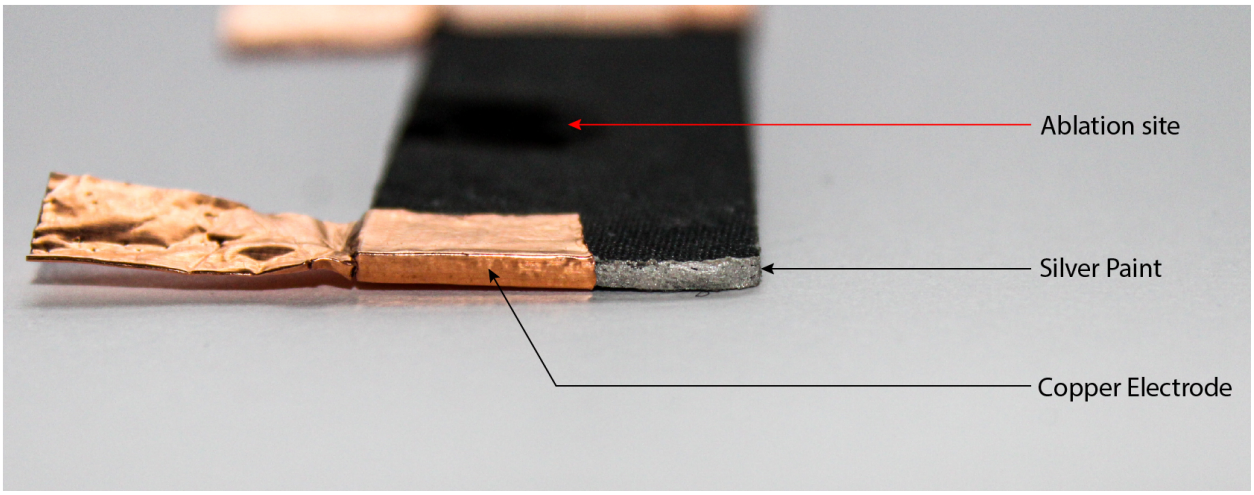

Figure 3.2. A rectangular strip specimen with copper tape partly removed to reveal conductive silver paint on its shorter edge. The ablation site (out of focus) is visible as a dark smudge.

The plate specimen for two-dimensional conductivity measurement was prepared using a 1.0 wt.% CNF-epoxy mixture. After curing, the finished laminate was sized down to make two squares – one measuring 2.75" per side and another measuring 3.25" per side. Each specimen was secured to an acrylic sheet measuring 4"×4" with the help of polyacrylate glue. Fast Drying Silver Paint Electrodag 1415M was applied in an alternating pattern with a equal spacing of 0.21" on all four edges of the 2.75" laminate and with 0.25" spacing for the 3.25" laminate. It was ensured that the corners of each side were left unpainted. The paint

was extended onto the acrylic sheet, which served the purpose of an electrode attachment. As a result of this, a laminate with 24 electrodes (6 per side) was prepared (see Figure 3.3). Due to the symmetric appearance of the laminate, the electrodes were numbered in order to avoid confusion during baseline measurement.

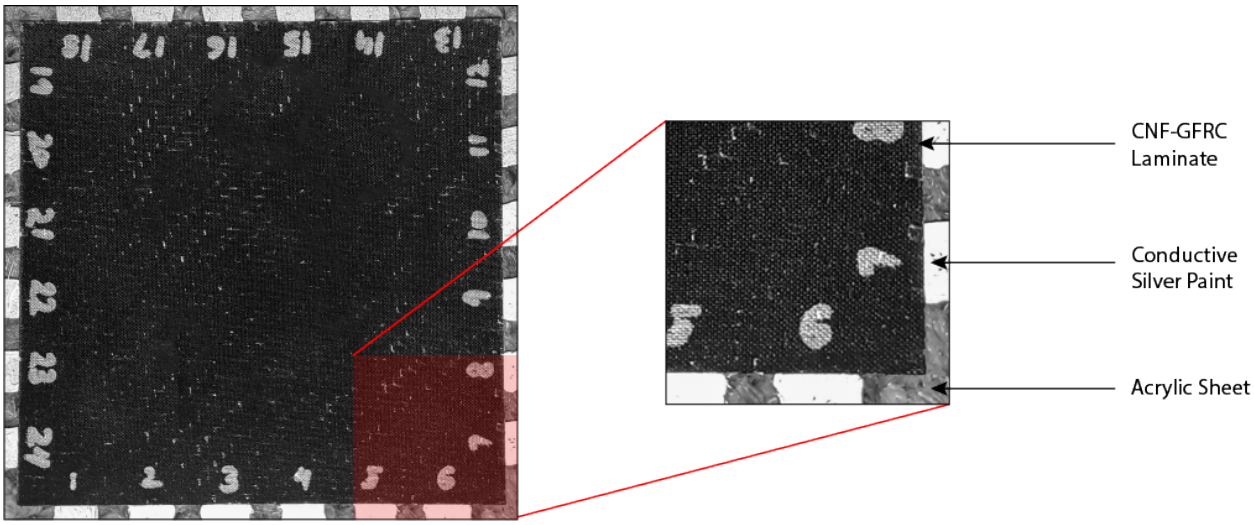

Figure 3.3. Prepared EIT square plate specimen ready for PLA. Magnified view shows the acrylic sheet, conductive silver paint, and the laminate.

3.2 Electrical Measurements

3.2.1 One-Dimensional Resistance Measurement in Rectangular Specimens

In order to test the rectangular strip specimens, a baseline resistance was measured for each specimen using a hand-held digital multimeter. The specimens were then placed in the fixture for laser ablation as shown in Figure 3.4. Two sets of experiments were initially planned to be performed on the specimens. The first by holding the fixture stationary in front of the beam and the second by moving the fixture in a path perpendicular to the beam at a constant velocity with the help of a uniaxially translating stage. However, when the non-stationary ablation was carried out, the energy output by the laser was so high that the specimen caught on fire by the time it passed the beam from one end to the other (see Figure 3.5). Consequently due to safety concerns, this type of testing was abandoned and only stationary ablation was carried out.

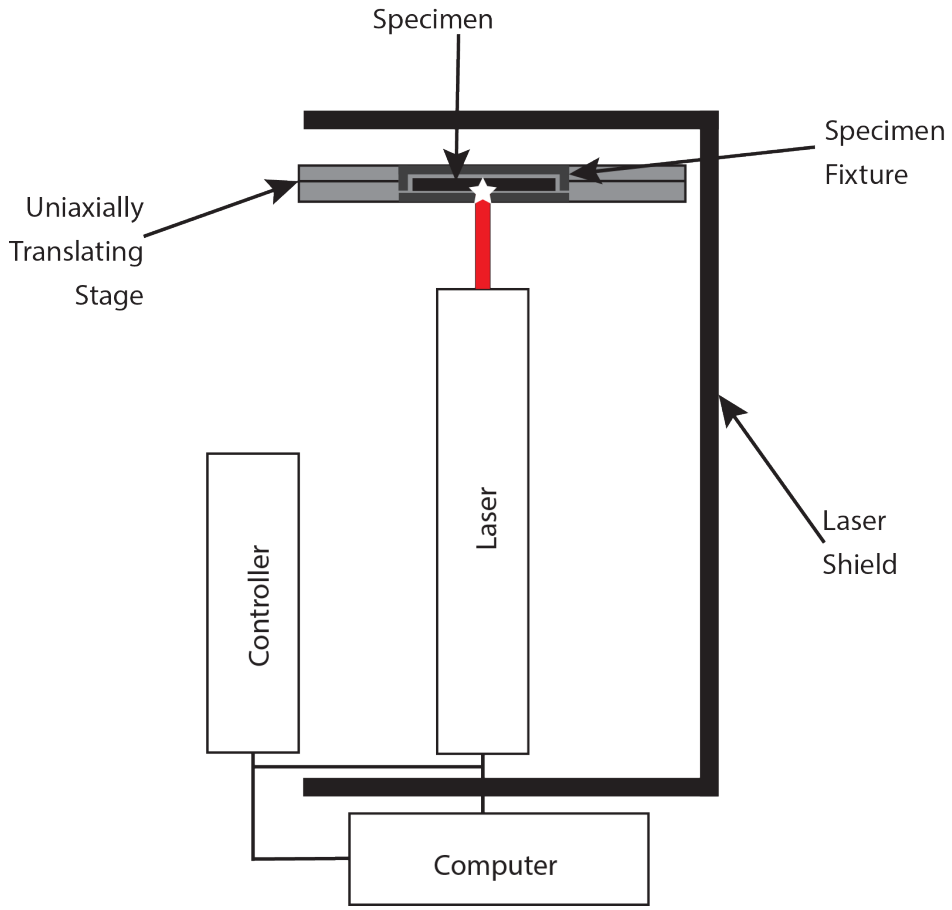

Figure 3.4. Schematic of the experiment for PLA of the CNF-GFRC laminates. The laser beam is represented in red color for better clarity, however, the beam is invisible to the human eye (since the laser operates at a wavelength of 1064 nm). The star signifies the site of ablation.

Each specimen was ablated for a total of 20 seconds (four exposures of five seconds each). Once ablated, the laser was turned off and the interlock opened. The specimen was carefully removed from the fixture and replaced with the next one. After all specimens were exposed to the laser, the change in resistance was again measured using a digital multimeter. This process was repeated for all strip-like specimens.

3.2.2 Two-Dimensional Conductivity Measurement in Square Plates

A baseline set of boundary voltage-current measurements was collected for each plate-like specimen prior to laser exposure. These baseline measurements are used for EIT as

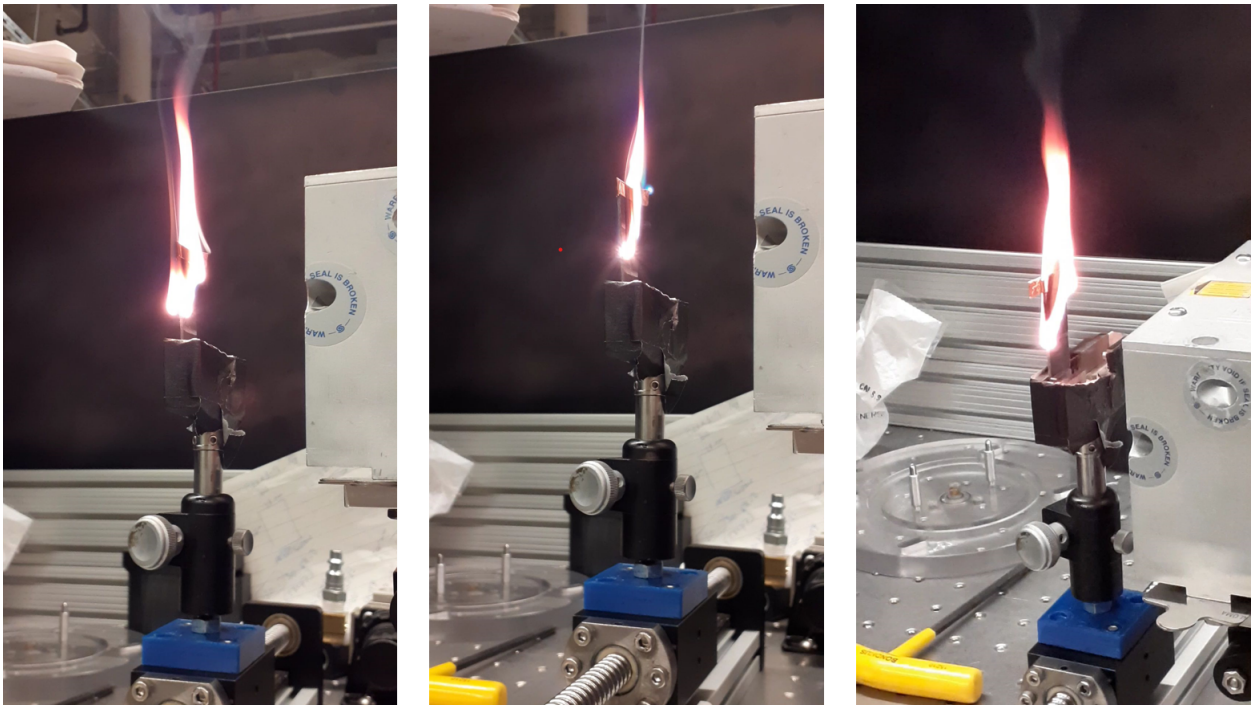

Figure 3.5. A montage of images showing the CNF-GFRC specimen bursting in flames as it passed in front of the beam at a velocity of 30 mm per minute.

described next in §3.3. Following these baseline measurements, stationary PLA was carried out on these specimens. The 2.75" laminate was exposed to the laser for 20, 10, and 5 seconds, and the 3.25" laminate was exposed to the laser for 1, 3, and 5 seconds. Each exposure took place in different areas of each laminate. Conductivity measurements via EIT were made after each ablation occurrence.

3.3 Electrical Impedance Tomography

EIT is a method of non-invasively mapping the conductivity distribution of a domain. EIT has been extensively explored for self-sensing materials [72]. Herein, EIT is used to detect and spatially localize laser exposure in self-sensing CNF-modified glass fiber/epoxy laminates. Note that EIT is merely used as a tool in this work – this work does not seek to advance the state of the art in EIT. Nonetheless, it is informative to provide some context to this imaging modality. To that end, a concise summary of both the mathematics and

experimental procedure used in this work are presented below. Relevant references are also provided for interested readers.

3.3.1 Mathematical Formulation

EIT consists of two parts – the forward problem and the inverse problem. The forward problem seeks to simulate the physics of current propagation in the domain being considered. The inverse problem then seeks to find a conductivity distribution that, when supplied to the forward problem, results in a predicted set of boundary voltages that match experimental observations for a prescribed set of current injections. Thus, EIT can be thought of as a minimization problem wherein we try to minimize the difference between model-predicted voltages and experimentally measured voltages as a function of the model's conductivity distribution.

EIT Forward Problem

The EIT forward problem begins with Laplace's equation for steady-state electrical diffusion in the absence of internal sources. This is expressed in Equation 3.1 where $\phi = \phi(\boldsymbol{x})$ is the domain solution (i.e., the domain voltage), $\sigma = \sigma(\boldsymbol{x})$ is the domain conductivity, and $\boldsymbol{x}$ is the position vector.

$$\boldsymbol{\nabla} \cdot \sigma \boldsymbol{\nabla} \phi = 0 \tag{3.1}$$

The complete electrode model (CEM) boundary conditions are then applied to Equation 3.1. This condition is shown in Equation 3.2. In Equation 3.2, z_l is the contact impedance between the lth electrode and the domain, $\boldsymbol{n}$ is an outward-pointing normal vector, and V_l is the voltage on the lth electrode.

$$\phi + z_l \sigma \boldsymbol{\nabla} \phi \cdot \boldsymbol{n} = V_l \tag{3.2}$$

Equation 3.1 is also subject to conservation of charge (i.e., current entering through the electrodes equals current leaving through the electrodes). This condition is shown in Equation 3.3 where E_l is the length of the lth and L is the total number of electrodes.

$$\sum_{l=1}^{L} \int_{E_l} \sigma \boldsymbol{\nabla} \phi \cdot \boldsymbol{n} \, \mathrm{d}S_l = 0 \tag{3.3}$$

Equations 3.1-3.3 are most often solved via the finite element method. Details on the discretization process can be found in references [72], [82].

EIT Inverse Problem

The EIT inverse problem refers to the process of finding a conductivity distribution that, when supplied to the forward model, minimizes the difference between a set of predicted boundary voltages and a set of experimentally measured boundary voltages. A common method of formulating this minimization problem is via a so-called difference image. In this approach, a conductivity change between two times is sought (i.e., the conductivity change before laser exposure and after laser exposure). This is in contrast to absolute imaging which seeks to produce the actual conductivity distribution at any given time. Difference imaging is more commonly used because it is more robust to errors that arise from, for example, model-to-experiment electrode misplacement and shape differences. Herein, a one-step linearization approach is used to find this difference. This approach is used because of its ease of implementation and satisfactory imaging capabilities. It should be noted, however, that more sophisticated non-linear difference imaging techniques also exist (e.g., [83], [84]). A good summary of various minimization techniques can also be found in reference [85].

Returning to the linear difference imaging problem, this can be cast as shown below in Equation 3.4 where $\delta\boldsymbol{\sigma}^*$ is a conductivity change distribution that satisfies the minimization, $\boldsymbol{y} = \boldsymbol{V}_m(t_2) - \boldsymbol{V}_m(t_1)$ is a voltage difference vector (i.e., the difference in boundary voltages measured before and after laser exposure at times t_1 and t_2, respectively), and $\boldsymbol{R}(\delta\boldsymbol{\sigma})$ is a regularization term the contribution of which is controlled by the scalar α. Regularization is needed because the EIT inverse problem is ill-posed. Herein, the discrete Laplace operator is used as regularization due to its ability to filter out high-frequency noise and promote

spatially smooth solutions. $\boldsymbol{J}$ is called the sensitivity matrix and is equal to the derivative of the forward model electrode voltages with respect to the conductivity distribution, $\boldsymbol{J} = \partial \boldsymbol{F}(\boldsymbol{\sigma}) / \partial \boldsymbol{\sigma}$. In this work, both the error and regularization norms are treated in the least-squares sense (i.e. they both utilize the l_2-norm). Different combinations of l_1 and l_2-norms for the error and/or regularization terms have been explored elsewhere [86]. Interested readers are directed to this reference for more information.

$$\delta\boldsymbol{\sigma}^* = \underset{\delta\boldsymbol{\sigma}}{\arg\min} \left(\|\boldsymbol{J}\delta\boldsymbol{\sigma} - \boldsymbol{y}\|_2^2 + \alpha \|\boldsymbol{R}(\delta\boldsymbol{\sigma})\|_2^2 \right) \tag{3.4}$$

3.3.2 Experimental Procedure

A 24-electrode setup was used in this work as shown in Figure 3.3. Current was injected at 1 mA (for the 2.75" plate) and 0.5 mA (for the 3.75" plate) and using an adjacent injection-measurement scheme and a Keithley 6221 current supply. Voltages were measured with respect to ground over a period of 10 s using a National Instruments (NI) PXIe-6368 data acquisition system. Voltages were measured for a period of 10 s so that averages could be calculated offline. This reduces the impact of noise in the measurements. Inter-electrode voltages were also calculated offline. One set of pre-laser exposure measurements was collected for each plate. Additional post-exposure measurements were then collected for each plate shortly after lasing the plates.

3.4 Pulsed Laser Ablation

A Spectra Physics Explorer® Diode-Pumped Solid State (DPSS) IR laser was employed in order to induce ablation. At the heart of this DPSS laser is a neodymium orthovanadate (Nd:YVO_4) crystal which serves as the active lasing medium. The laser operates at the nanosecond scale, with a pulse duration of 8.2 ns and emits in the NIR regime of the electromagnetic spectrum, at a wavelength of 1064 nm. With pulse energy, E, of 0.1628 mJ (at repetition rate, f_{rep}, of 35 kHz) and pulse width, τ_l, the laser provides a peak pulse power of 19.86 kW [87].

The laser in the Dynamic Mechanics Laboratory at Purdue University was equipped with safety interlocks which allowed for the safe operation of the laser. The laser would not operate if the door of the laboratory was ajar. This ensured the safety of the lab personnel in and around the vicinity of the laser. Before performing the laser ablation, appropriate eye protective gear was equipped. The protective goggles were opaque to the infra-red radiation emitted by the laser but were transparent to some frequencies of visible light. This ensured proper visibility and protection simultaneously. After the necessary connections between the computer, controller, and the laser were established, the power supply for the laser was turned on, and the laser was allowed to warm up for about ten minutes. In the meantime, a fixture to hold the specimen was attached on the optical bench at a distance of 60 mm from the laser output. Following this, the prepared specimen was secured in the fixture, as seen earlier in Figure 3.4.

The repetition rate on the laser was set to 0 Hz, so that the laser could be operated in CW mode. The laser has a pulse energy of 0.1628 mJ, as described earlier. When it operates in a pulsed manner, this energy is delivered in the pulse duration, i.e., 8.2 ns. As a result, the laser delivers a power of 19.86 kW in that time period. If the laser were to be operated in the CW mode, the output power would be 0.1628 mW. This was essential to bring the output power to a very small value, which is benign for skin exposure. The interlock was closed and the gate was opened, allowing the laser to radiate. With the help of a Thorlabs VRC2 VIS/IR Detector Card [88] (capable of operating in 400-640 nm and 800-1700 nm) the alignment of the specimen was carried out, ensuring that the laser spot was roughly in the center. This was done by placing the card in the beam path, between the laser and fixture. If the fixture was aligned with the beam, a spot on the detector card would be illuminated by IR beam. Adjustments were made to the fixture until the beam perfectly aligned with the center of the specimen. Once aligned, the interlock was engaged once again, and the gate was closed. The repetition rate was set to 35 kHz. The controller was set to an exposure time of five seconds. This allowed the trigger to allow lasing to occur only for the stipulated amount of time, after which the lasing action would cease automatically. This process primed the laser to be ready for operation.

Figure 3.6 shows the laser under use, performing PLA on a 1.0 wt% CNF-modified GFRC rectangular strip. The IR radiation is invisible to the human eye, and hence can be deceivingly destructive in nature. The laminate immediately starts exuding fumes of epoxy on contact with the beam, signifying the high amount of energy transferred from the beam to the surface.

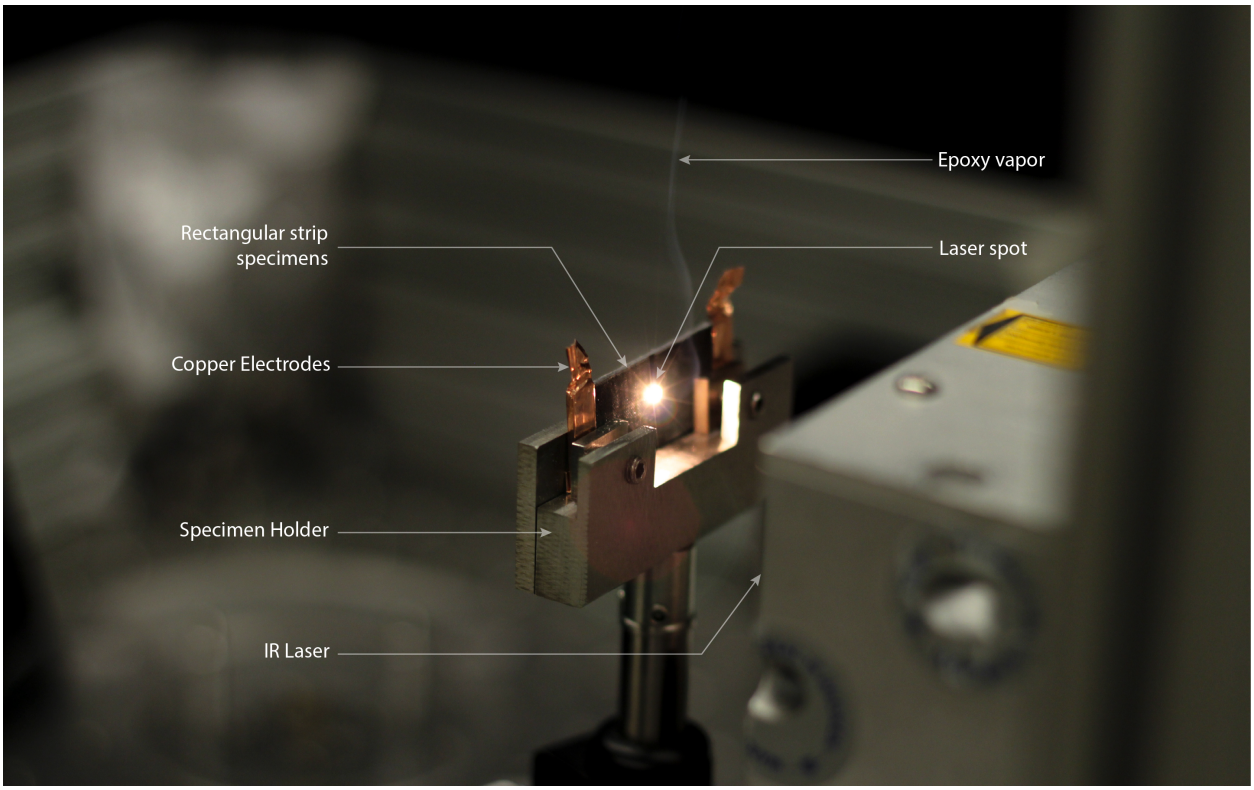

Figure 3.6. A rectangular CNF-GFRC strip specimen under laser ablation. The invisible radiation is intense enough to vaporize/ablate (see white fumes emerging off-center) the epoxy from the laminate.

4. RESULTS AND DISCUSSION

This chapter comprises the visual observations of the different topographical features on the rectangular strip specimens and the square plate specimens. These observations were made using a Carl Zeiss Axioskop 2 MAT microscope with Nikon D610 DSLR Camera (for optical imaging) and a FEI^{TM} Quanta 3D FEG Dual-beam scanning electron microscope (for SEM imaging). The results from one-dimensional resistance (for rectangular strip specimens) and two-dimensional conductivity (for square plate specimens) measurements are discussed too.

4.1 Visual Observations

A variety of topographical features in and around the ablation craters were observed by using an optical and microscope and a scanning electron microscope (SEM). The SEM used a high voltage of 5 kV and beam current of 25 pA, working distance of 2 mm, T2 detector, and OptiPlan mode as imaging parameters. SEM imaging was conducted at the Purdue Electron Microscopy Facility. It is important to note that a detailed exploration of the effect of laser exposure on microstructure exceeds the scope of this thesis. Rather, the intent of this sub-section is to show via optical and scanning electrical microscopy that the laser exposure does indeed have a considerable impact on the connectivity of the underlying CNF network, which allows for piezoresistive-based self-sensing.

4.1.1 Optical Imaging

Figure 4.1 shows the effect of nanosecond pulse duration on a 1.5 wt.% CNF-modified GFRC rectangular strip specimen. The presence of glass fiber bubbles is apparent on the surface at first glance. The yellow outline in Figure 4.1 shows the outline of the ablation crater on the top surface. Even though the laser beam formed a circle on the laminate surface, the hole is not circular. The shrinking yellow outline indicates the decrease in damage with

increasing depth. The Gaussian profile of the beam corroborates this effect; the intensity of the beam can represented as Equation 4.1.

$$I(r) = I_0 \exp\left(-\frac{r^2}{w_0^2}\right) \tag{4.1}$$

Where w_0 is the width of the laser focus defined by the intensity $I(w_0) = I_0/\mathrm{e}$. With increasing depth, coupled with heat absorption by the glass fibers and CNF, and heat of vaporization of epoxy in each lamina, it is possible that the volume of damage is crudely conical in geometry.

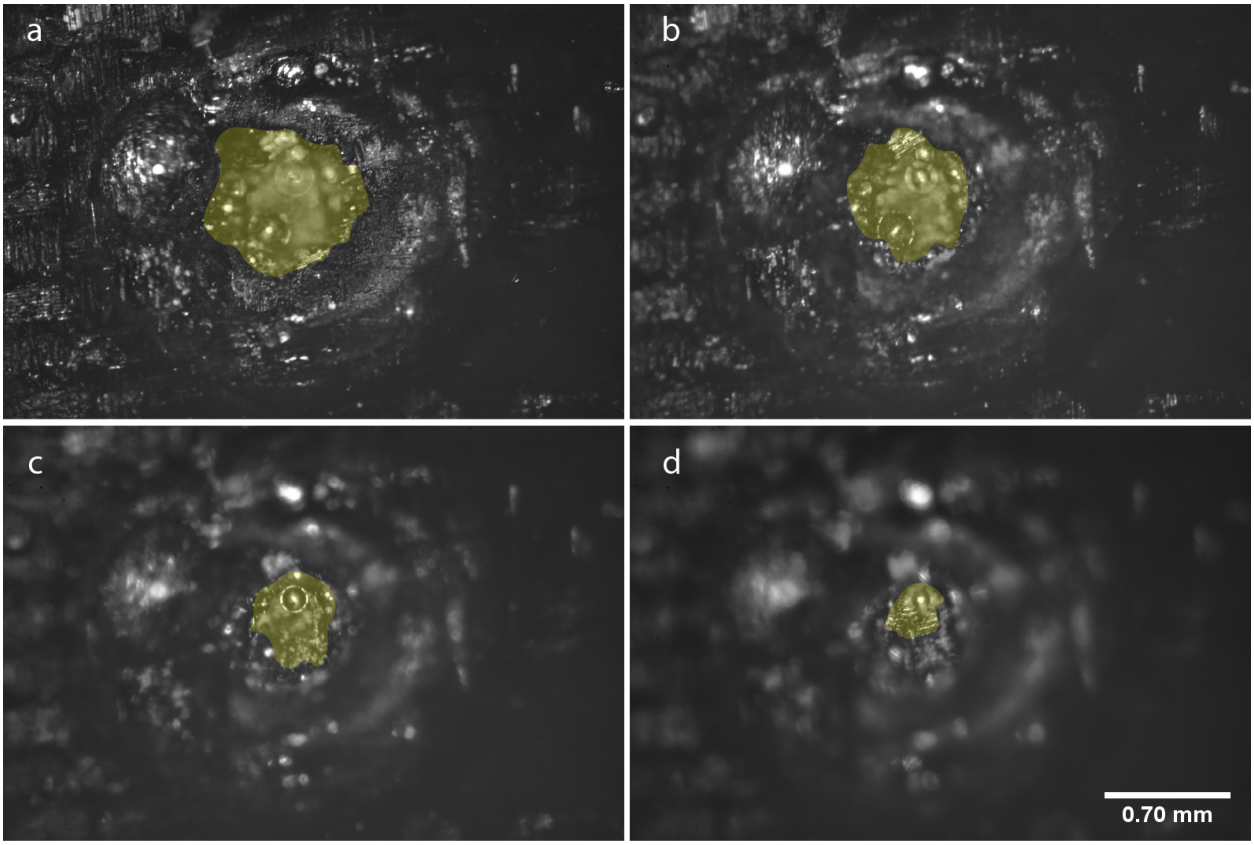

Figure 4.1. An ablation crater (with increasing depth of focus) on a 1.5 wt% CNF-modified GFRC rectangular strip specimen formed due to laser exposure of 20 seconds. The sub-figures get out-of-focus due to a very limited focal length of the microscope. The yellow outline represents the different layers of the composite seen at varying depths.

In Figure 4.2, several topographical features of the area surrounding the ablation crater can be observed. The boundary is especially interesting to observe because one can understand how the pulse duration plays an important role in heat transfer. As shown by Chichkov et al. (see Figure 1.6 [43]), the thermal effects dominate and cause splashing of the molten material during the lasing action. This results in the formation of the bubbles and uneven topography around the ablation crater.

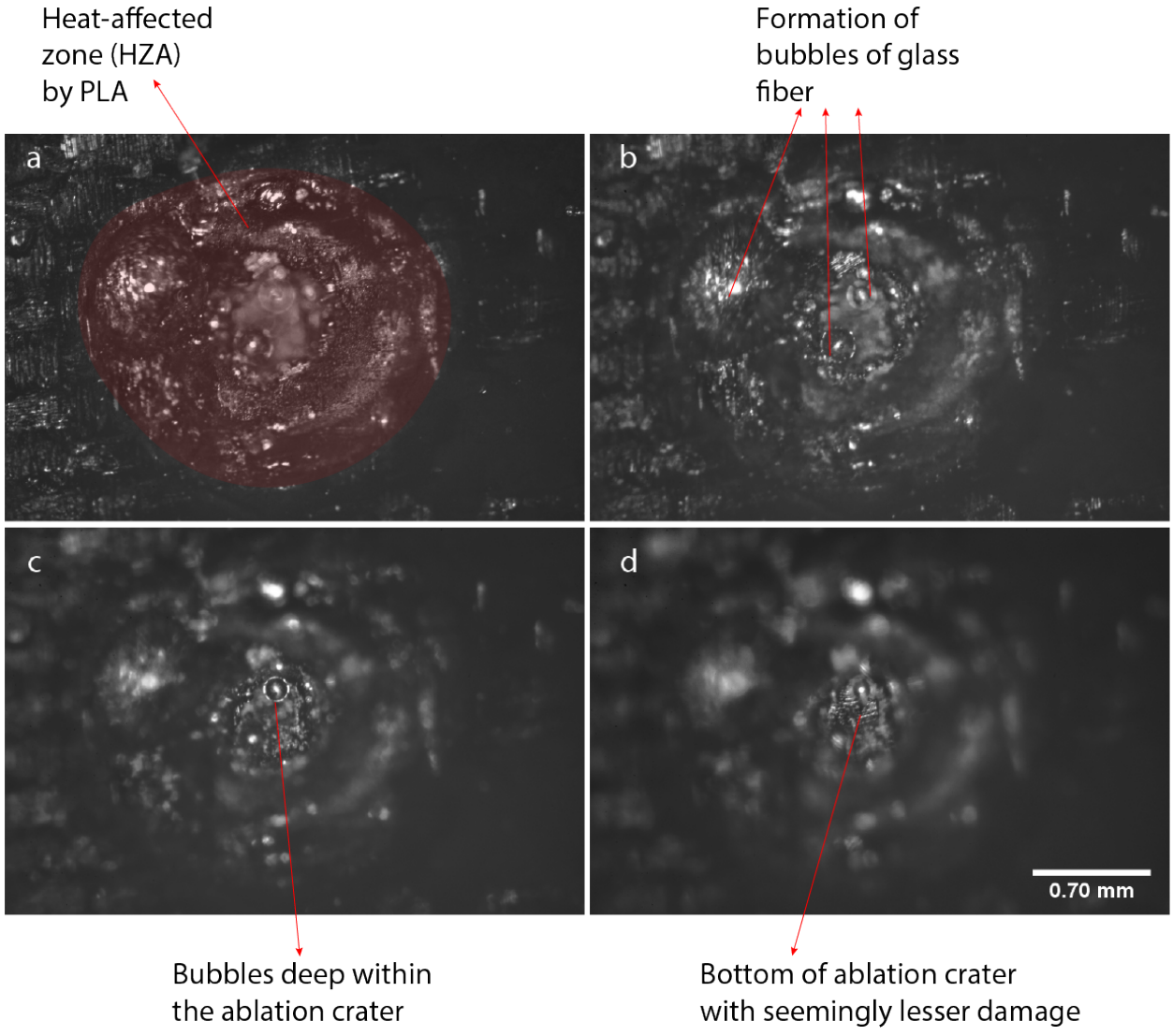

Figure 4.2. A sequence of images(from left to right, and top to bottom) showing various features of the ablation crater caused by PLA on 1.5 wt.% CNF-modified GFRC composite due to laser exposure for 20 seconds.

On closer inspection of the ablation trench (green box in Figure 4.3) formed in the non-stationary ablation specimen, the thermal effects of lasers operating in the nanosecond pulse duration were observed (similar to those seen in Chichkov's work (see Figure 1.6) on effect of pulse duration [43]). As the beam spot traversed across the specimen, molten glass fiber possibly resulted in splashing due to the escaping epoxy vapor and hardened on the surface. It can be safe to assume that the temperature of the trench during ablation was well above the softening temperature of the E-glass fibers which is around 846 °C [89].

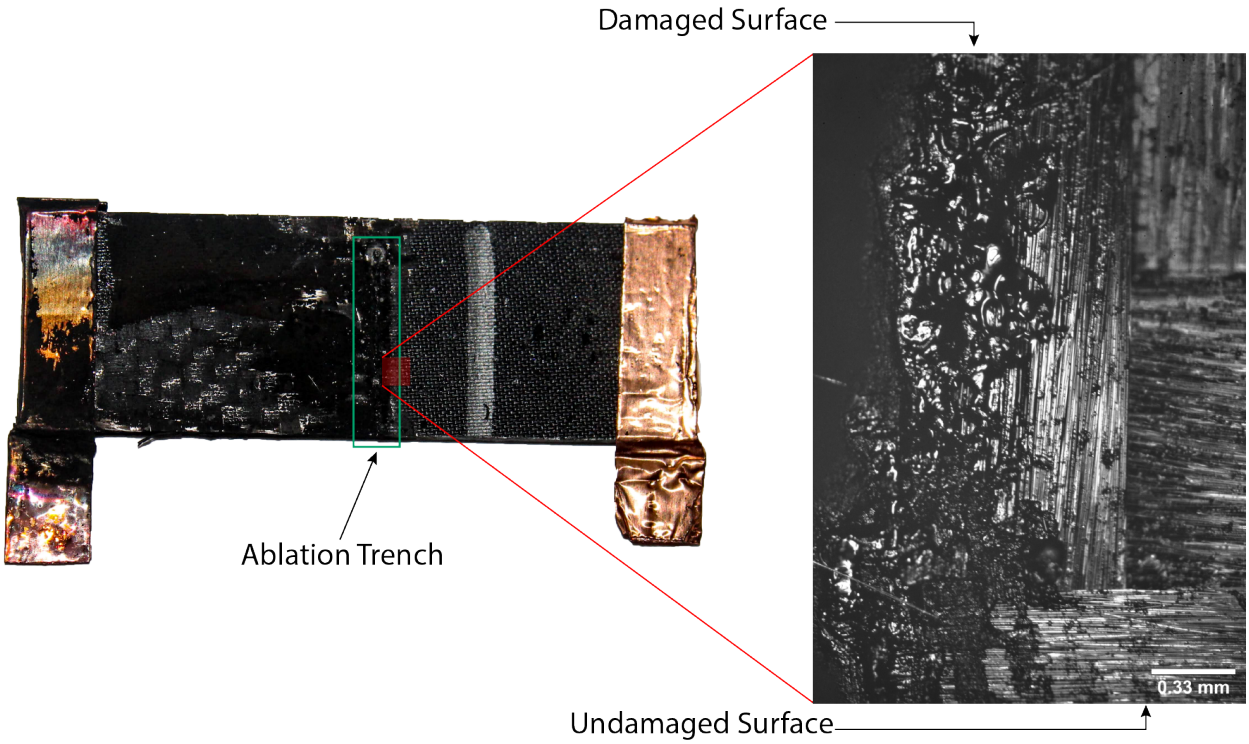

Figure 4.3. Ablation trench (green box) of the 1.5 wt.% CNF-modified GFRC specimen as a result of non-stationary PLA at a translatory rate of 30 mm per minute. The ablation trench, as seen at 20× magnification (magnified). Note the difference in topography of the damaged and undamaged surface. The laser was operated at 1064 nm, 35 KHz, and an open gate (to allow for uninterrupted lasing action).

Figure 4.4 shows the bubble formation within bubbles of glass fiber in a 0 wt.% CNF-modified GFRC (i.e., an un-modified GFRC). The reason for manufacturing a specimen with no CNF present in the matrix phase was to compare the effect of presence of CNF on the ablation crater. As seen in Figure 4.4, the bubbles are visibly translucent, if not completely

transparent. This could possibly give us an insight on the interior of glass fiber bubbles in CNF-modified GFRC specimens, which are opaque in nature. These bubbles could either be epoxy vapor or air trapped within the large bubble. The intense heating and rapid cooling of the specimen may have resulted in gas to evolve, but not escape from the viscous bubbles. The spherical shape of the bubbles may be attributed to the relatively high surface tension (around 230-360 dyne/cm) of molten glass [90], which is roughly between than that of water and mercury [91], [92].

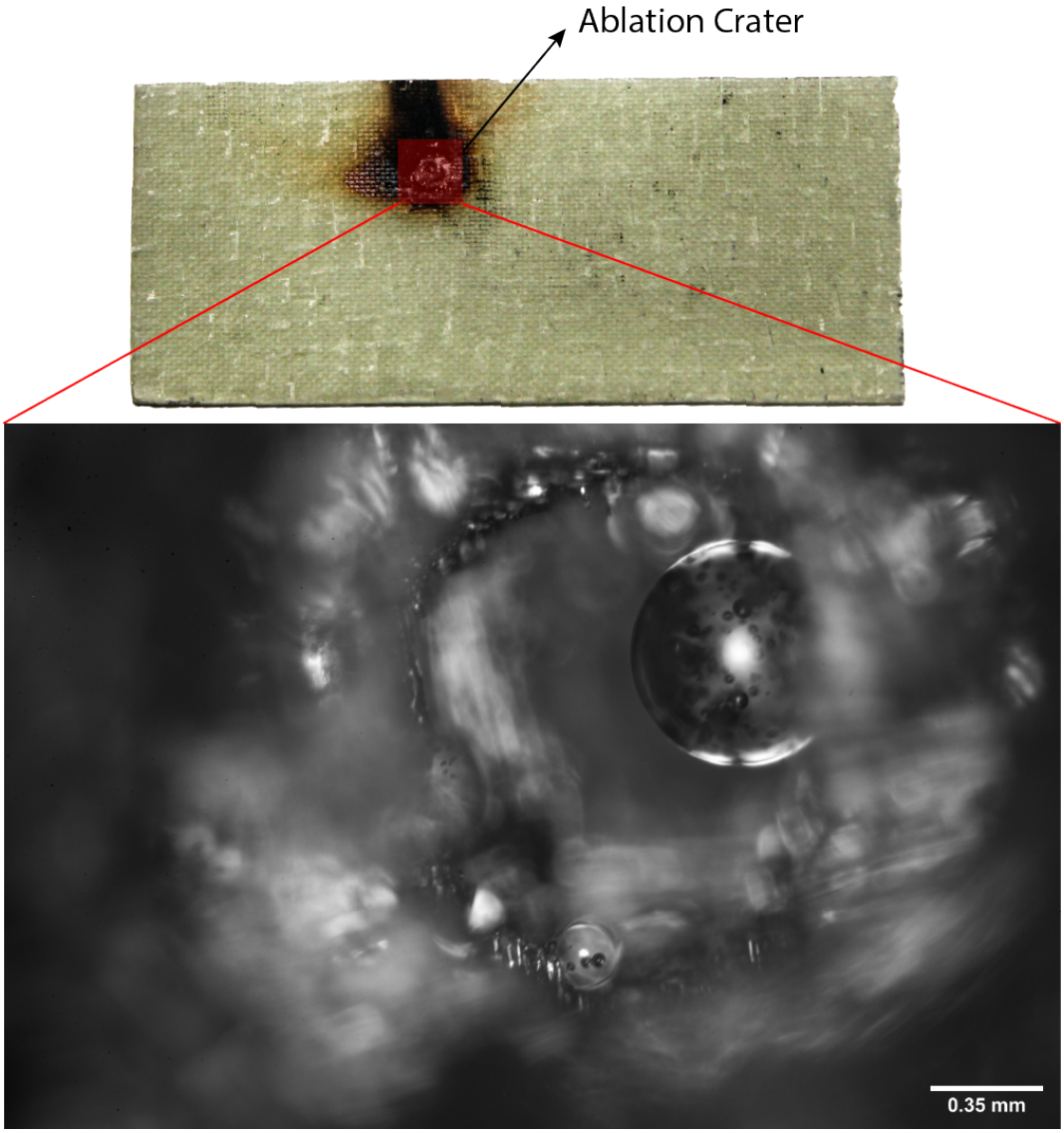

Figure 4.4. Bubble formation within bubbles of glass fiber in an ablation crater on a 0 wt.% CNF-modified GFRC specimen.

4.1.2 SEM Imaging

Figure 4.5 shows the comparison of 0.5, 1.0, and 1.5 wt.% CNF-modified GFRC specimens exposed to the laser for 20 seconds each. Every specimen exhibits a roughly circular ablation crater ring around the cavity. However with increasing concentration of CNF, the crater rings seem to be more defined. This could possibly result from a higher amount of CNFs absorbing the heat rather than diffusing the same through glass fibers. It should be noted, however, that this conjecture was not tested; as mentioned previously, an in-depth investigation into the effect of CNF modification on ablation mechanisms exceeds the scope of this thesis. Unlike the damage surface resulting from fracture which often has glass fibers protruding through it, the damage surface obtained via ablation results in a bubbled texture throughout it.

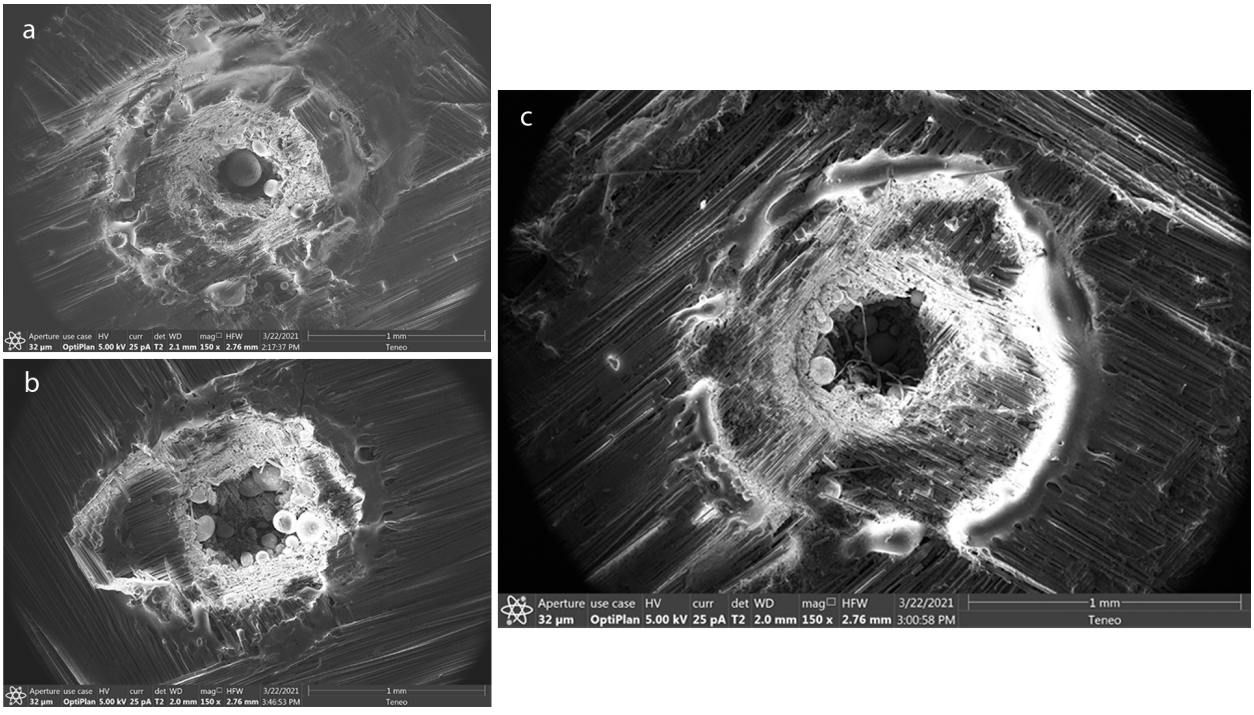

Figure 4.5. Ablation crater formed in (a) 0.5, (b) 1, and (c) 1.5 wt.% CNF-modified GFRC specimens after laser exposure of 20 seconds as seen at 150× magnification.

It was interesting to note that CNFs were virtually absent at the ablation surfaces of specimens containing 0.5 and 1.0 wt.% CNF, however CNFs were observed in epoxy debris

present on glass bubbles. Figure 4.6 shows the absence of CNFs and prevalence of bubbly texture at the damage surface, and the CNFs protruding through the epoxy debris found on one of the glass fiber bubbles in the interior of the crater.

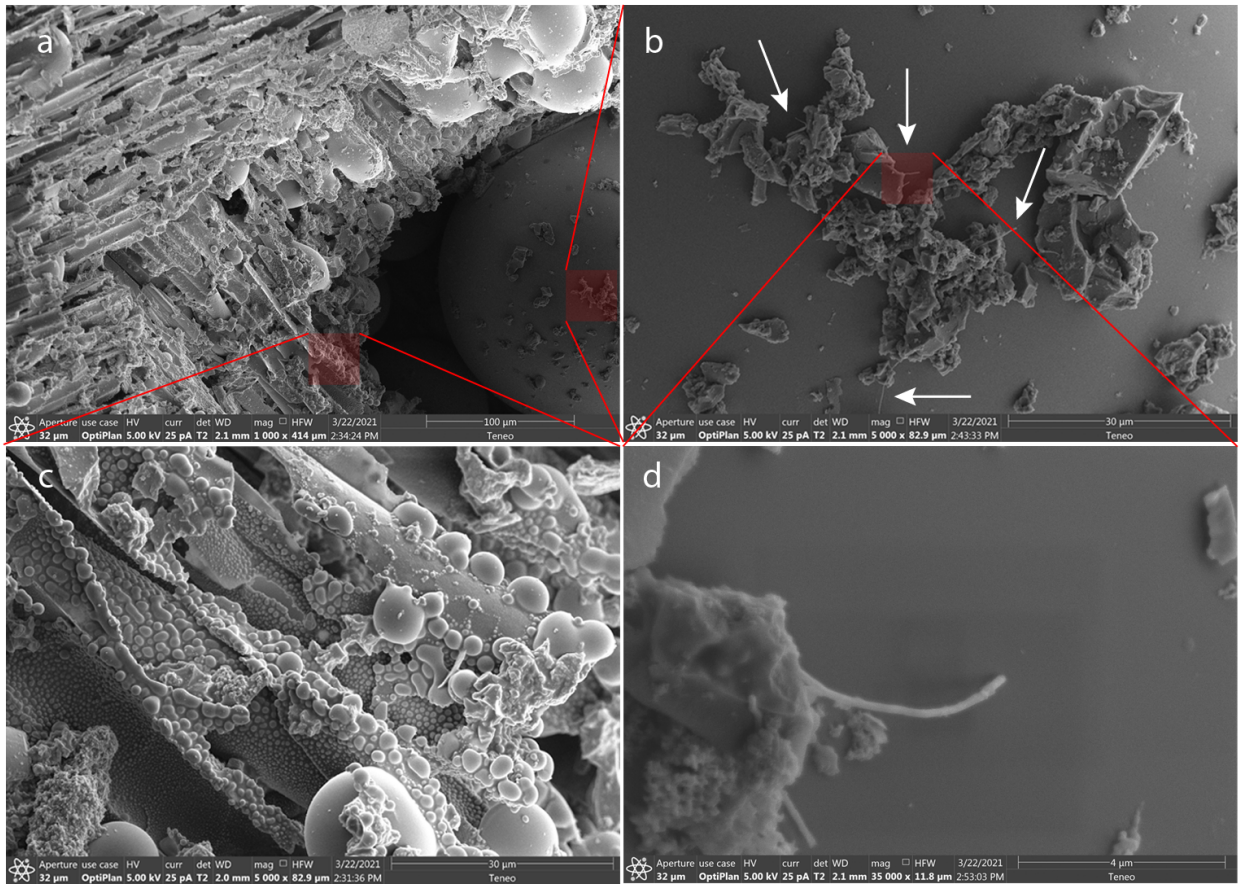

Figure 4.6. Fracture surface of an ablation crater in a 0.5 wt.% CNF-modified GFRC specimen with (a) showing the damaged surface in the ablation crater, as seen at 1000× magnification, (b) CNFs protruding through epoxy debris found on one of the glass fiber bubbles, as seen at 5000× magnification, (c) Bubble formation on glass fibers on fracture surface, and (d) magnified view of CNF protruding through epoxy debris as seen at 35000× magnification.

Figure 4.7 shows a 1.5 wt.% CNF-modified GFRC specimen with CNFs protruding through the epoxy matrix at the ablation surface within the crater. There also seems to be ripple formation on one of the epoxy pieces.

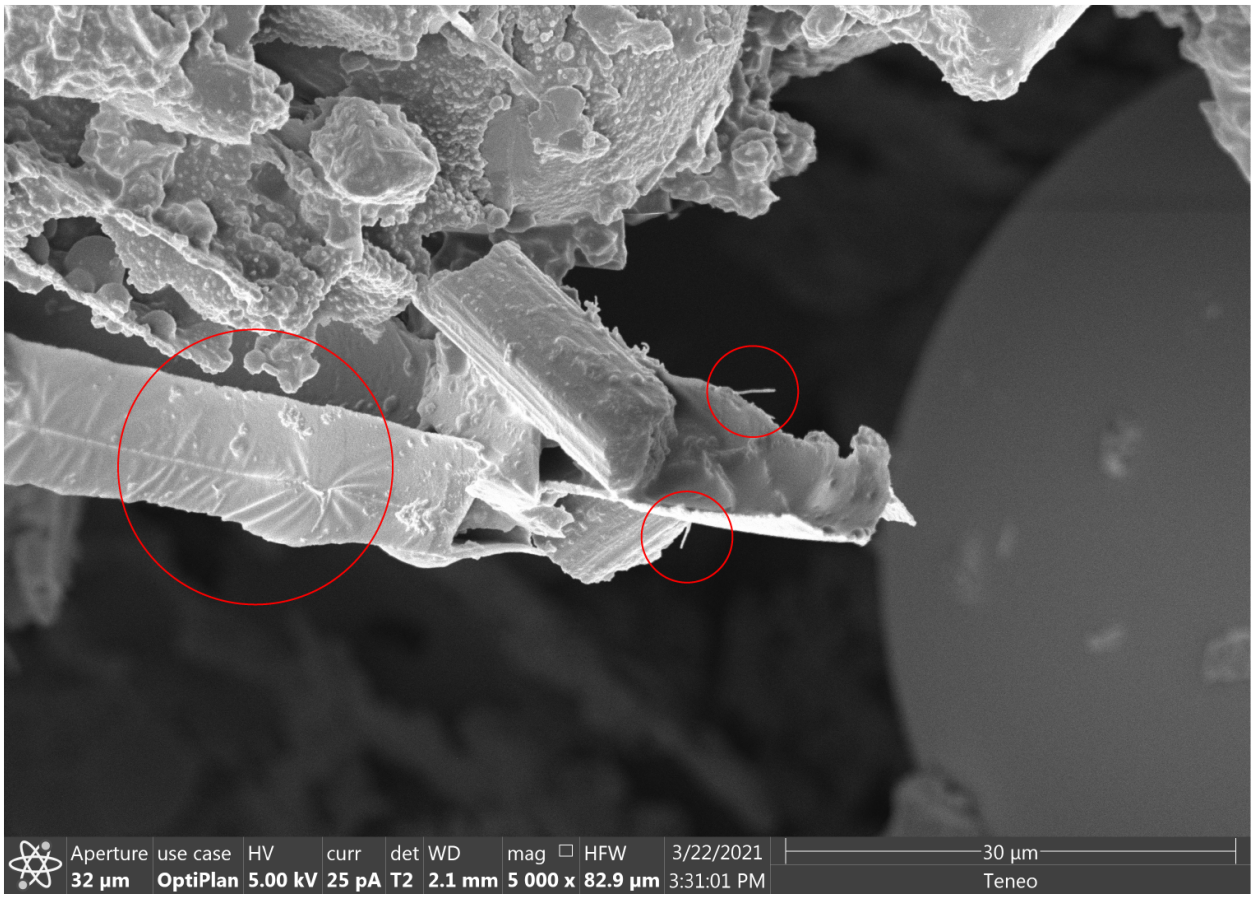

Figure 4.7. CNFs, as seen at 5000× magnification, protruding out of epoxy on ablation surface of 1.5 wt.% CNF-modified GFRC specimen on laser exposure of 20 seconds.

The effect of 1, 3, 5, 10, and 20 seconds of laser exposure on 1.0 wt.% CNF-modified GFRC specimens was observed. Figure 4.8a shows a 1-second laser exposure with a relatively low penetration damage to the glass fibers; glass fibers from the lamina beneath are visible. Bubble formation is prevalent on the periphery of the crater, but the bubbles do not seem to be very large in size. Figure 4.8b shows a 3-second laser exposure with similar features as the 1-second laser exposure, with the exception of having larger bubbles rather than small ones.

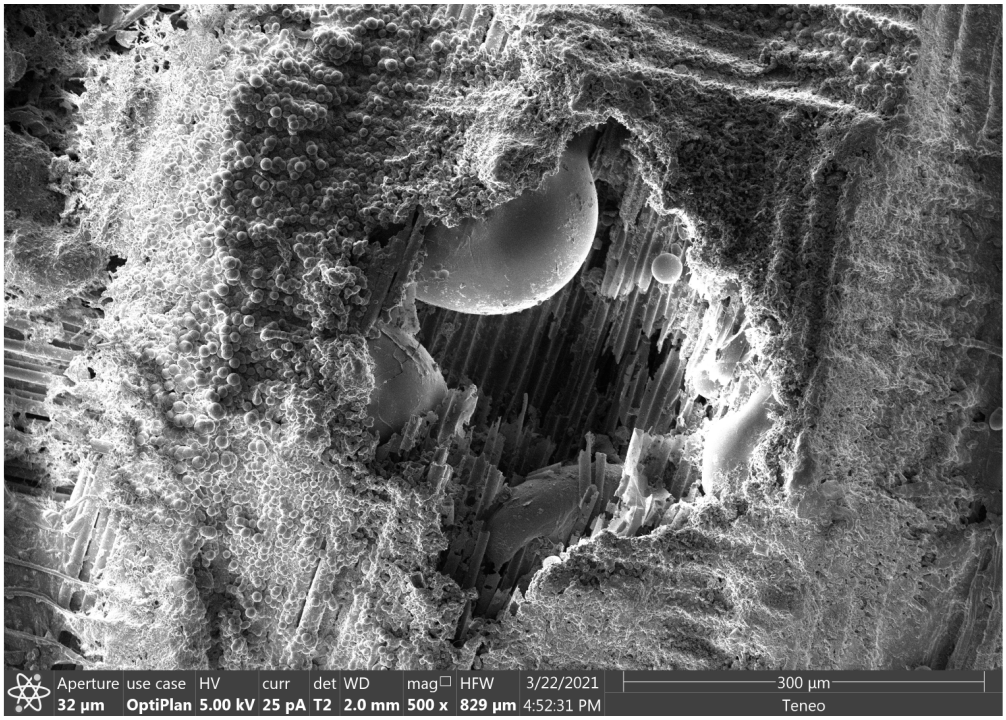

(a) 1-second laser exposure on 1.0 wt.% CNF-modified GFRC specimen.

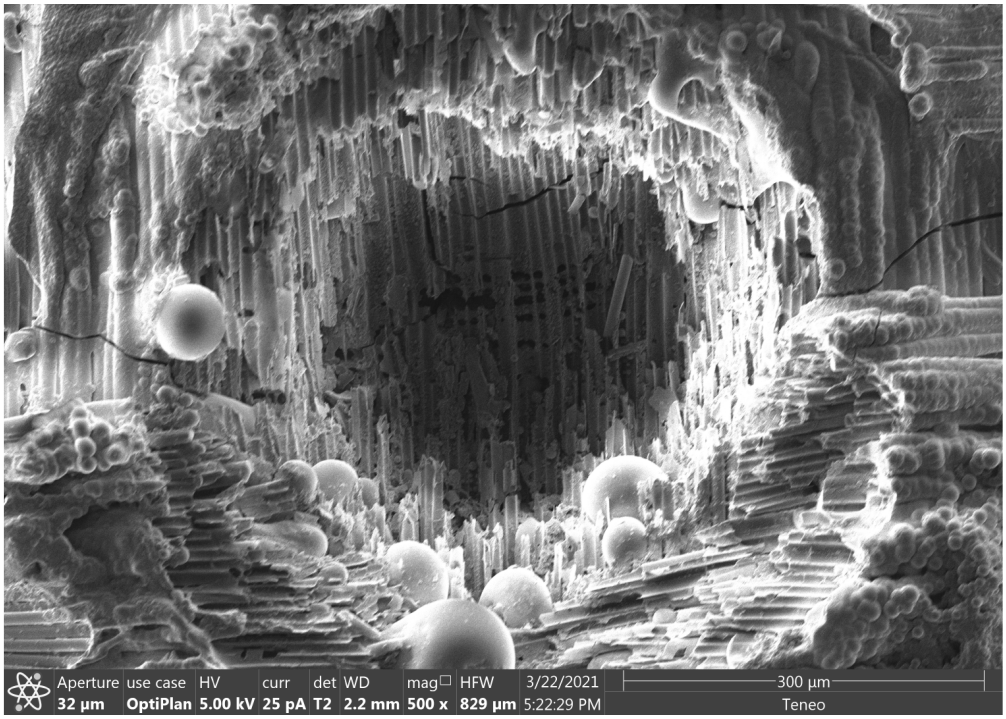

(b) 3-second laser exposure on 1.0 wt.% CNF-modified GFRC specimen.

Figure 4.8. Comparison of ablation craters formed by 1 and 3 seconds of laser exposure on 1.0 wt.% CNF-modified GFRC specimens as seen at 500× magnification.

Increasing the duration of laser exposure to 5 seconds resulted in the formation of a deeper crater, as seen in Figure 4.9. The depth of the crater appears to be greater than those of craters in Figure 4.8. However, a crack is present at the bottom of the crater. Figure 4.10 show the ablation craters formed by exposing the specimens to the laser for 10 and 20 seconds respectively. Figure 4.10a shows a large glass bubble at the center of the crater, which has a small 'bridge' of epoxy connecting the bubble to the crater periphery. The crater has a more defined circular boundary as compared to those exposed for lesser duration. Figure 4.10b shows extensive large bubble formation which extends to the bottom of the crater. This resulted from exposing the specimen for an extended period of time, which allowed immense amount of heat to be transferred deep within the laminate. As a result of which, the crater is deeper than those formed by exposures of lesser duration. In addition to this, the bubbles exhibit a bumpy texture, ripples, and other irregular geometry on them.

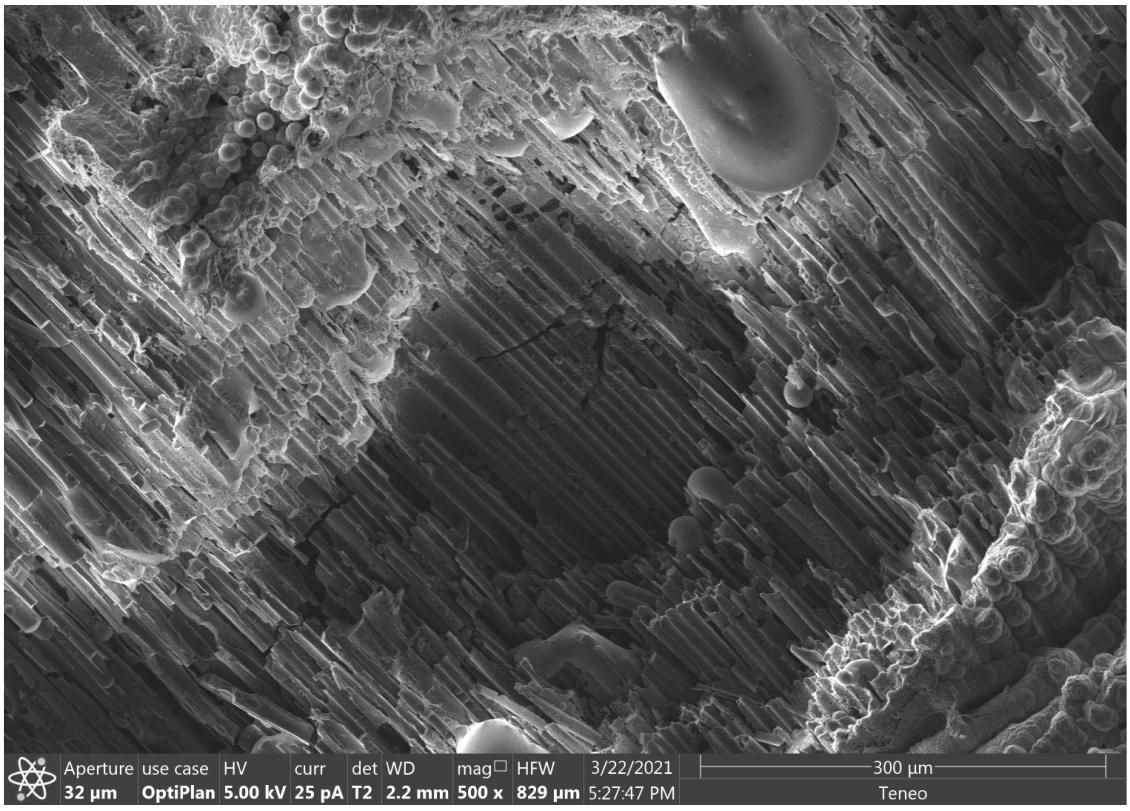

Figure 4.9. Ablation crater formed by a 5-second exposure on 1.0 wt.% CNF-modified GFRC specimen, as seen at 500× magnification.

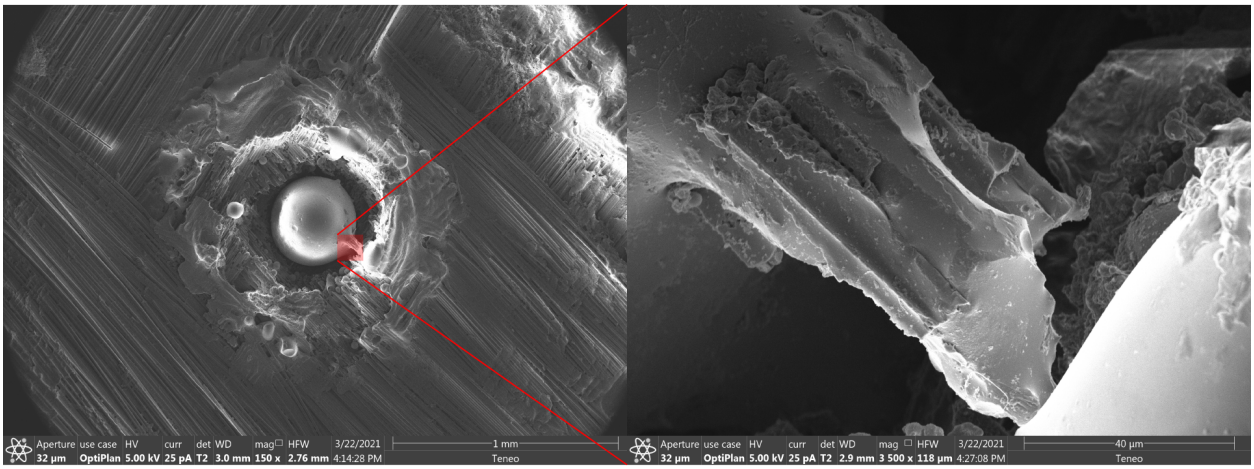

(a) Ablation crater formed by a 10-second exposure on 1.0 wt.% CNF-modified GFRC specimen as seen at 150× magnification. The magnified image (at 3500× magnification) shows epoxy bridge connecting the bubble to the crater periphery.

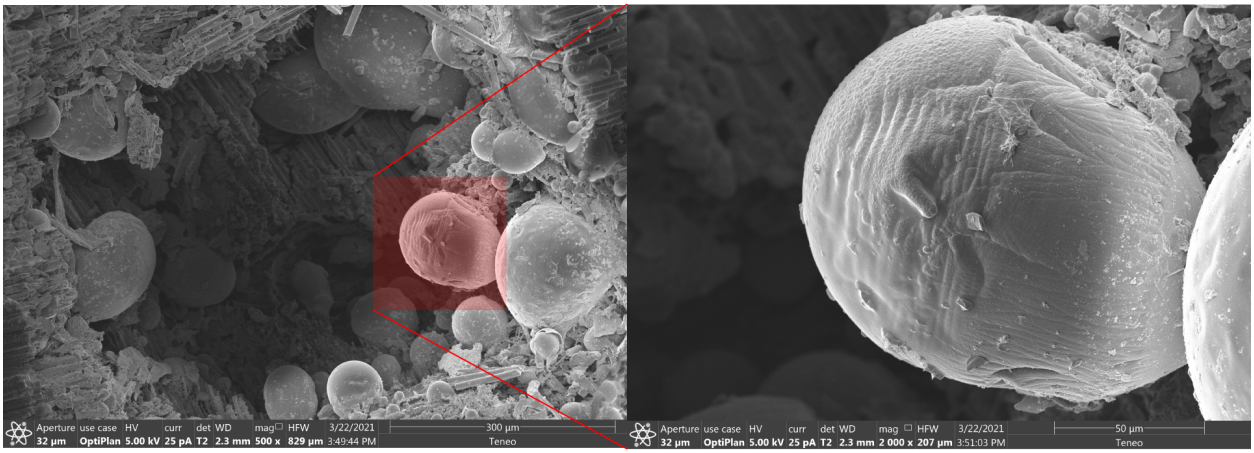

(b) Bubble formation within an ablation crater formed by a 20-second exposure on 1.0 wt.% CNF-modified GFRC specimen as seen at 500× magnification. The magnified image (at 2000× magnification) shows topography of a bubble.

Figure 4.10. Comparison of ablation craters formed by 10 and 20 seconds of laser exposure on 1.0 wt.% CNF-modified GFRC specimens.

The photomicrographs in this section reveal the detrimental effects of laser exposure on the connectivity of the CNF network. The glassy masses around the ablation crater, the presence of glass bubbles within the ablation crater, and the absence of CNF on the damaged surfaces all suggest the presence of the insulating nature of glass and the absence of the conductive nature of CNF. We therefore expect this damage to be able to be sensed via electrical changes.

4.2 One-Dimensional Resistance Measurement in Rectangular Specimens

Once the cured laminate was sized to rectangular strips, the physical dimensions of the strips were recorded. The physical dimensions of the specimens are summarized in Table 4.1.

Table 4.1. Summary of physical dimensions of rectangular strips for one-dimensional resistance measurement. All dimensions values are averaged.

CNF wt.%	Dimension (mm)		
	Length	Breadth	Thickness
0.5	47.08±1.92	15.77±0.92	1.19±0.02
1.0	43.68±6.26	17.49±0.97	1.19±0.01
1.5	47.47±0.79	15.11±0.85	1.19±0.01

Thirty specimens of each type of laminate were tested. The physical dimensions of the specimens are very close, hence a comparative study can be made. Resistance measurements were made using a hand-held digital multimeter for each specimen before and after exposure to the laser. The resistance measurements before and after PLA are summarized in Table 4.2.

Table 4.2. Summary of electrical properties of rectangular strips for one-dimensional resistance measurements before and after laser exposure. All resistance and change in resistance values are averaged.

CNF wt.%	Resistance (kΩ)		Change in Resistance (%)
	Pre-Ablation	Post-Ablation	
0.5	499.15±165.18	2351.55±1966.70	330.61±268.64
1.0	6.24±3.04	7.32±3.57	17.76±5.78
1.5	3.31±2.09	3.70±2.26	12.95±6.71

Table 4.2 shows that the average material resistance uniformly decreases with an increase in the weight percent of CNF in the matrix. However, the mean pre- and post-ablation resistance of the 0.5 wt.% specimens was abnormally larger than the 1.0 and 1.5 wt.% CNF-

modified GFRC specimens. Similar behavior was observed in the standard deviation of the resistance. This is likely due to the fact that lower filler weight fractions are well known to have significant variability in conductive properties due to the lack of redundant electrical paths in the nanofiller network.

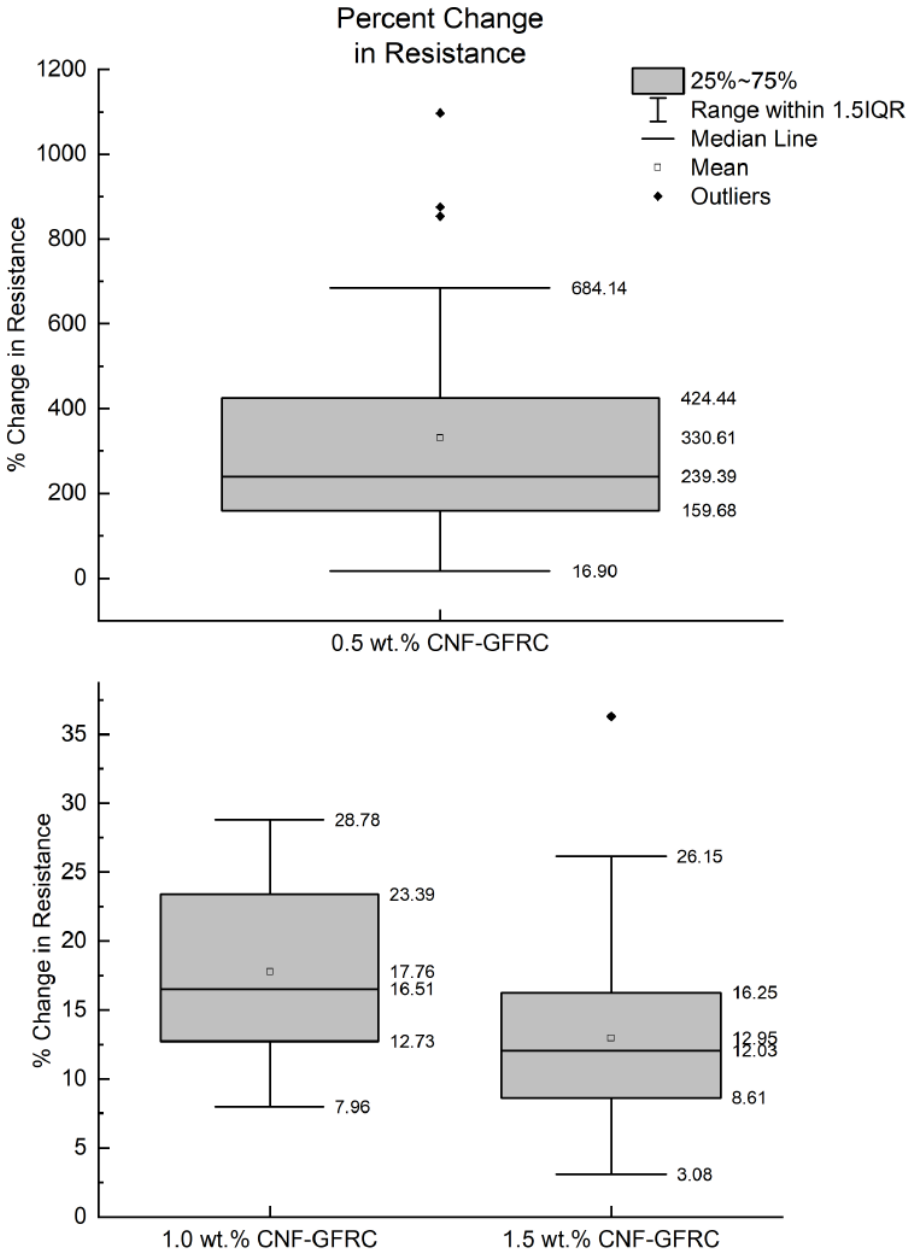

Figure 4.11. Comparison of resistance spread with 0.5, 1.0, and 1.5 wt.% CNF-modified GFRC specimens.

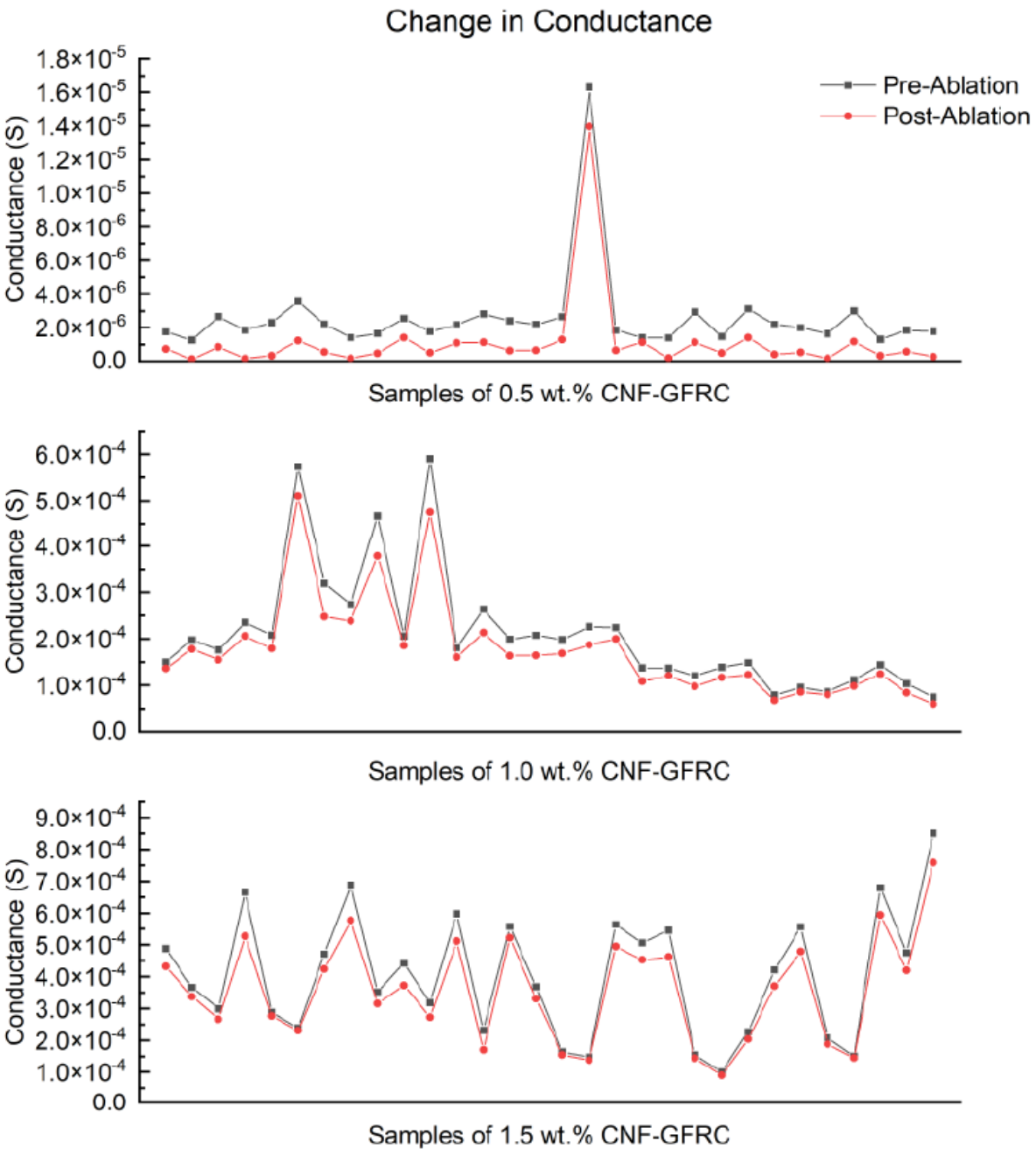

Figure 4.12. The conductance of 0.5, 1.0, and 1.5 wt.% CNF-modified GFRC specimens before and after PLA processing of the laminate.

By the visual inspection of the boxplots in Figure 4.11, it can be inferred that the 0.5 wt.% CNF-modified GFRC specimens exhibit the highest variability in the percent change in resistance (as high as approximately 1100% for one particular outlier) with an average change

of about 330%, while the 1.5 wt.% CNF-modified GFRC specimens exhibit the lowest variability, with an average change of about 13%. Again, this agrees with our expectation that composites with higher nanofiller concentrations exhibit less variability and less sensitivity compared to lower concentrations.

The effect of the concentration of the CNFs is very apparent. The CNFs present in the matrix transform the initially non-conductive epoxy to a conducting one. In its presence it is therefore possible to monitor the electrical properties such as resistance and voltage with ease. The CNFs form a dense three-dimensional network within the laminate and act as miniature electrically-conductive pathways, thereby making it possible to record electrical measurements through the laminate. Since current chooses the shortest pathway to flow between any two given points, thus in an undamaged state (pre-ablation), the resistance measured by the digital multimeter is the resistance experienced by the current in the shortest path. Any kind of damage to this network would potentially sever the network partially. This would cause the shortest path to elongate slightly, thereby increasing the resistance of the laminate. Upon exposing the rectangular strip specimens to laser radiation, a rise in the resistance of all strips was observed. This rise in resistance was, however, inversely proportional to the amount of CNFs present in the laminate.

4.3 Localized Ablation in Plate Specimens

A total of two square plates were manufactured for this experiment, one measuring 2.75" and the other 3.25". Both plates were made with 1 wt.% CNF/epoxy. This weight percent of CNF was chosen because it showed consistent electrical properties without an excessively high CNF concentration which makes the manufacturing process more difficult. The 2.75" square plate was exposed to the laser for 5, 10, and 20 seconds at the laser parameters specified in §3.4. EIT was then applied to localize these laser exposures. It was found that EIT was not only successful in detecting the presence of laser-induced ablation, but also accurately localizing the site of ablation. As a result of this, the experiment was repeated with lesser duration of laser exposures (1, 3, and 5 seconds) to determine the lower limit of detecting laser exposure by EIT.

Table 4.3. Summary of electrical properties of square plates for two-dimensional conductivity measurements before and after laser exposure. All conductivity, change in conductivity, and cumulative change in conductivity values are averaged.

Side Length	Exposure (s)	Conductivity (S/m)$\times 10^{-3}$		$\Delta\sigma$(%)	Cumulative $\Delta\sigma$(%)
		Pre-Ablation	Post-Ablation	$\times 10^{-2}$	$\times 10^{-2}$
	20	380.00	371.52±26.67	-223.09	-223.09
2.75±0.00	20, 10	371.52±26.67	358.17±34.33	-359.50	-574.57
	20, 10, 5	358.17±34.33	342.87±34.81	-427.17	-977.20
	1	380.00	379.96±1.08	-1.12	-1.12
3.25±0.00	1, 3	379.96±1.08	379.39±2.10	-15.07	-16.19
	1, 3, 5	379.39±2.10	377.91±2.65	-38.99	-55.11

*pre-ablation conductivity is 0.38 S/m and the values for $\Delta\sigma$ are computed via EIT

Table 4.4. Summary of the maximum local conductivity drop of square plates for two-dimensional after laser exposure.

Side Length	Exposure (s)	Max. $\Delta\sigma$ (S/m) $\times 10^{-3}$	Min. Local Cond. (S/m)$\times 10^{-1}$
	20	-154.54±26.67	2.26
2.75±0.00	20, 10	-188.69±34.33	1.83
	20, 10, 5	-194.00±34.81	1.64
	1	-7.23±1.08	3.73
3.25±0.00	1, 3	-9.19±2.10	3.71
	1, 3, 5	-9.51±2.65	3.69

The electrical properties of the square plates are summarized in Table 4.3 and Table 4.4. Figure 4.13a shows the tomographic image of the 2.75" CNF-modified GFRC plate after 20 seconds of laser exposure. There is an accurate mapping of the ablation site – the location of the computed image and the actual ablation site coincide well with each other. The amount of heat absorbed by the plate during this run was equal to the heat absorbed by a rectangular strip specimen. Upon visual inspection the actual plate (Figure 4.13b), it is evident that there is visible damage at the ablation site. Bubbles of glass fiber were visible on the crater boundary, and also within the ablation crater similar to the ones seen in Figure 4.2.

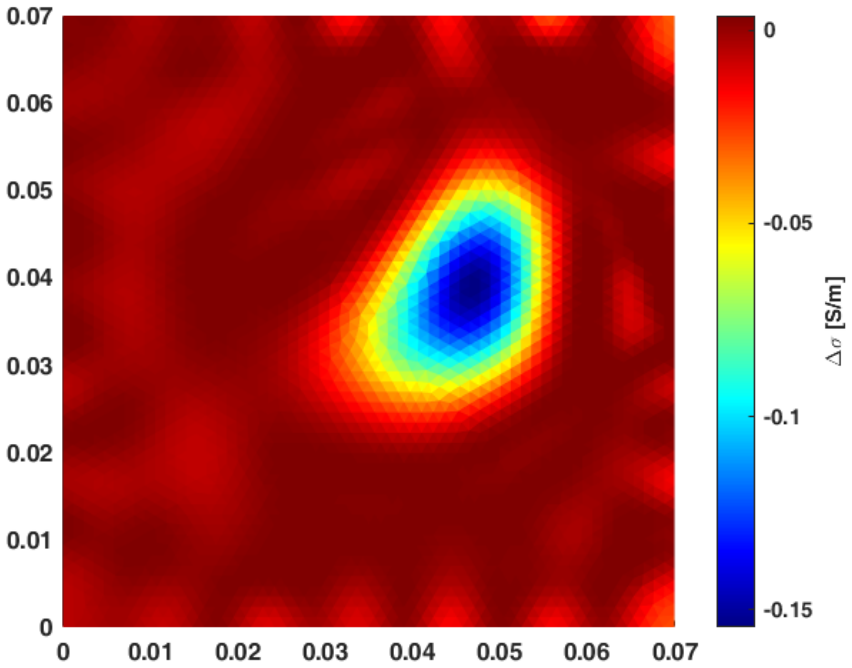

(a) The conductivity mapping of the 2.75" square plate after 20 seconds of laser exposure.

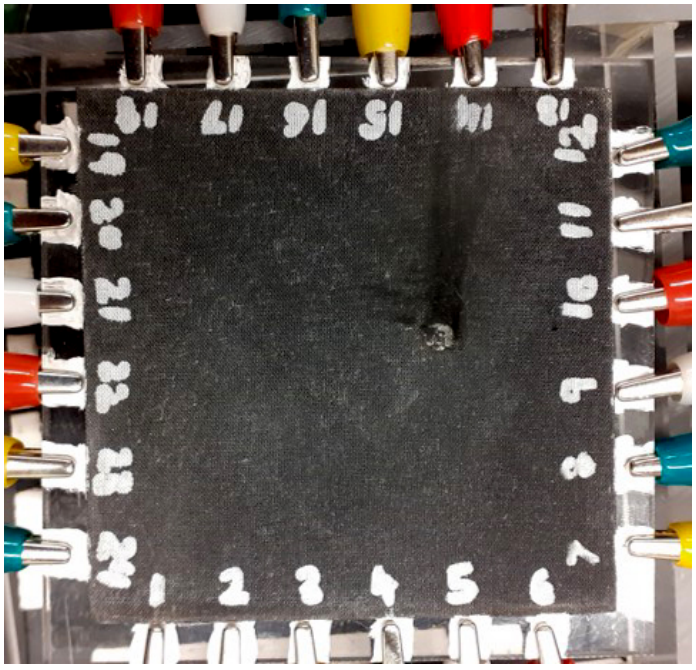

(b) Actual CNF-modified GFRC laminate showing site of ablation (center-right).

Figure 4.13. Comparison between actual site of damage and tomographically-computed site of damage.

Once the conductivity map was computed via EIT, the plate was exposed to laser radiation for 10 seconds and the conductivity map was re-evaluated. This step was repeated with a laser exposure of 5 seconds. Figure 4.15 shows the evolution of the conductivity maps created after each instance of laser exposure. The comparison between the final EIT-generated images and the actual plates can be seen in Figure 4.14a.

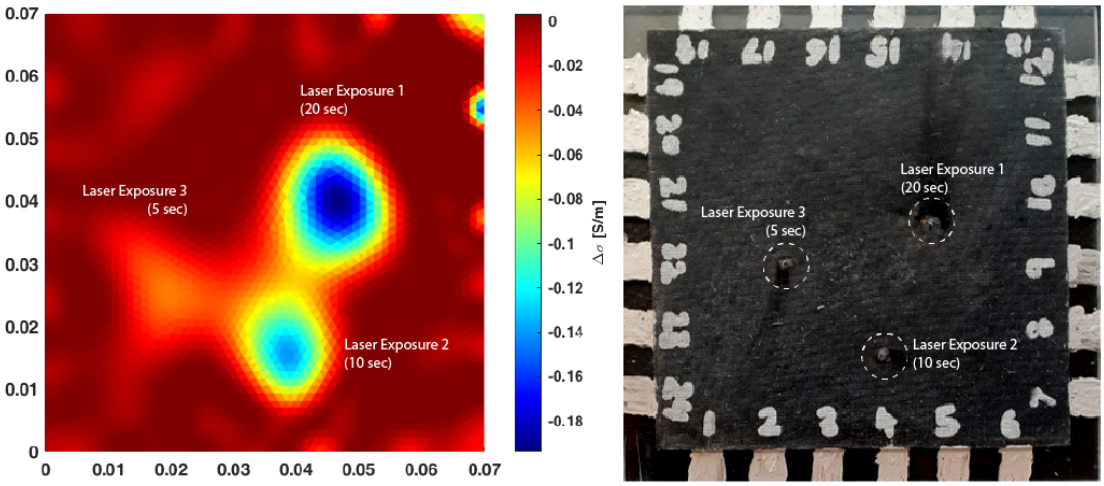

(a) Comparison between final damage state of the tomography image and the actual 2.75" plate.

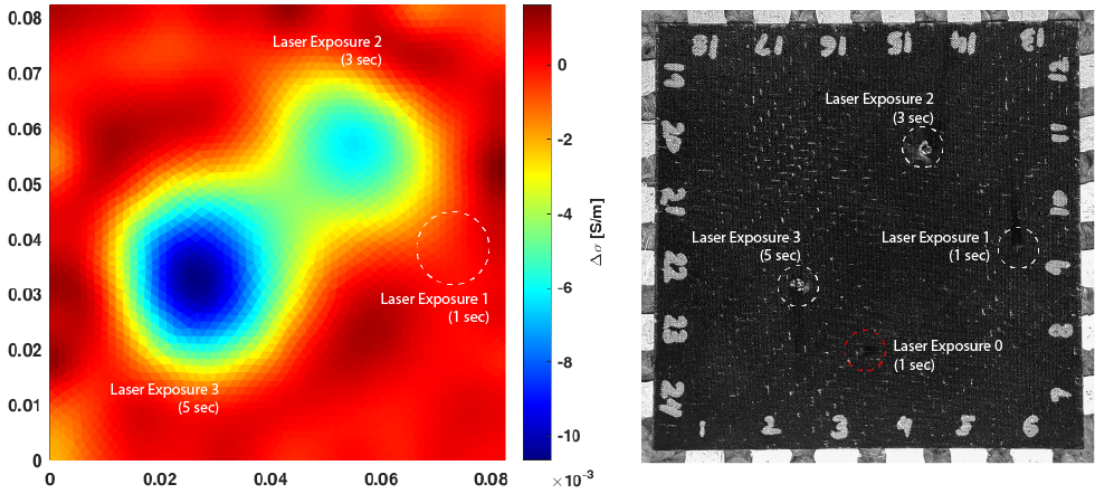

(b) Comparison between final damage state of the tomography image and the actual 3.25" plate.

Figure 4.14. Comparison between the tomographically-computed image and actual sites of damage of plate specimens.

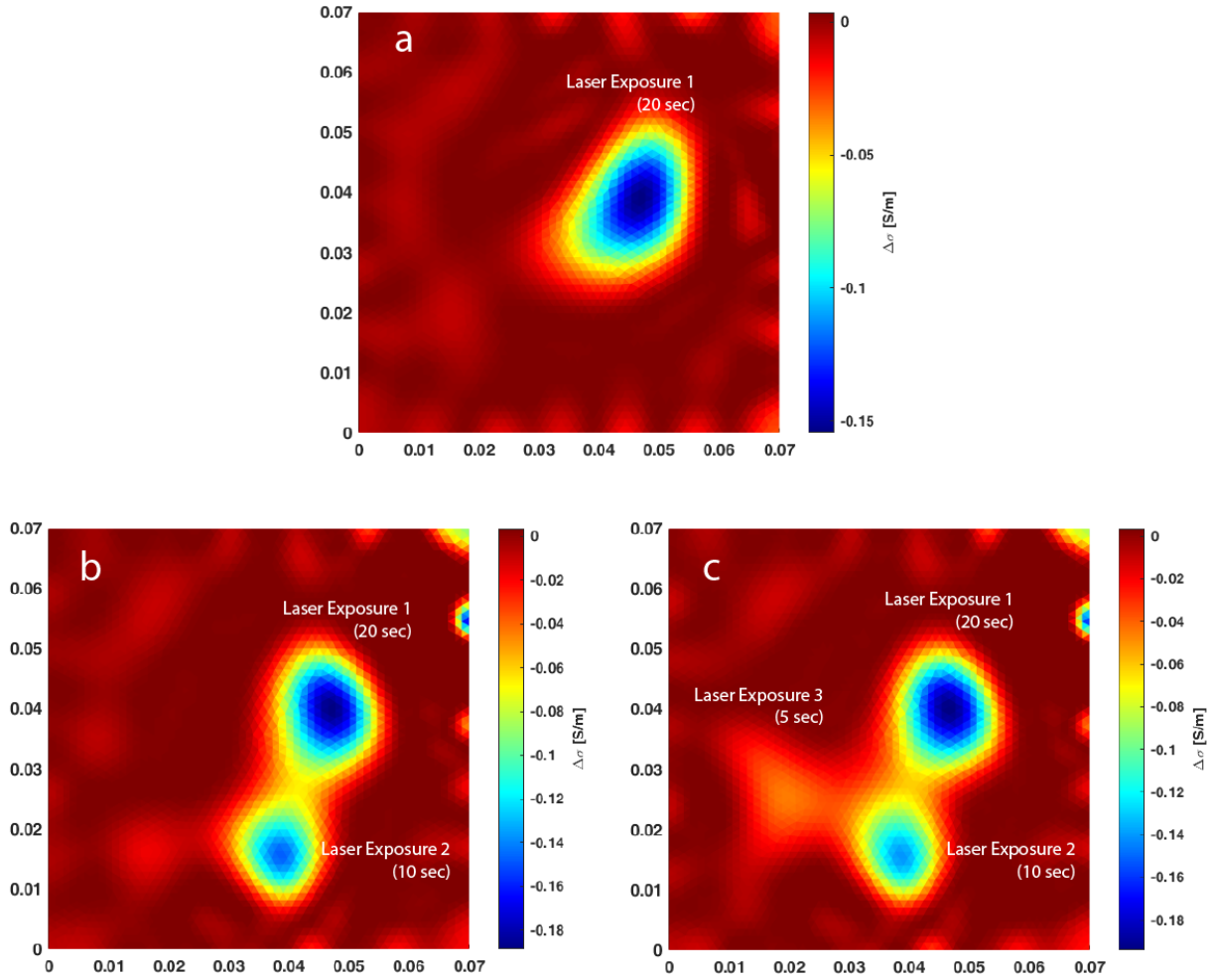

Figure 4.15. Tomographic images of the 2.75" 1 wt.% CNF-modified GFRC plate showing the evolution of damage. Conductivity maps after laser exposure of- (a) 20 seconds, (b) 20 and 10 seconds, (c) 20, 10, and 5 seconds, respectively.

Although the damage caused by the 5 second could not be clearly seen because the damage caused by the 20 and 10 second exposures was very high, it was better visualized by using the damage state after the 10 second exposure as a baseline and then using difference imaging to see the conductivity change (see Figure 4.16).

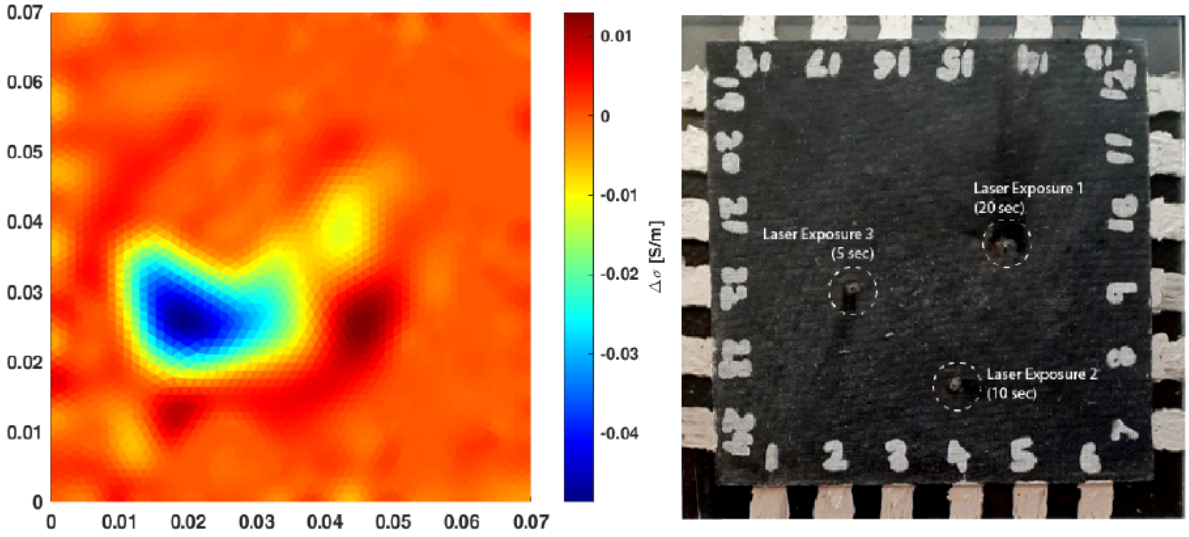

Figure 4.16. Conductivity changes on 2.75" 1 wt.% CNF-modified GFRC plate due to 5 second exposure only.

Next, the 3.25" square plate specimen was exposed to 1, 3, and 5 seconds of laser exposure. When the 1 second exposure was delivered to the laminate plate, there was an erroneous display of the conductivity mapping due to a faulty baseline of the undamaged plate. As a result of this, the damage state of the laminate after this exposure (red outline in Figure 4.14b) was considered as the new baseline and the 1-second PLA was conducted again at a new location. Figure 4.17 shows the conductivity evolution in the 3.25" square plate. The final exposure of 5 seconds causes the conductivity changes much greater than that caused by the 1-second exposure, as a result of which the conductivity change by the 1-second exposure is overshadowed by the change caused by the 5-second exposure. The comparison between the final EIT-generated image and the actual plate can be seen in Figure 4.14b.

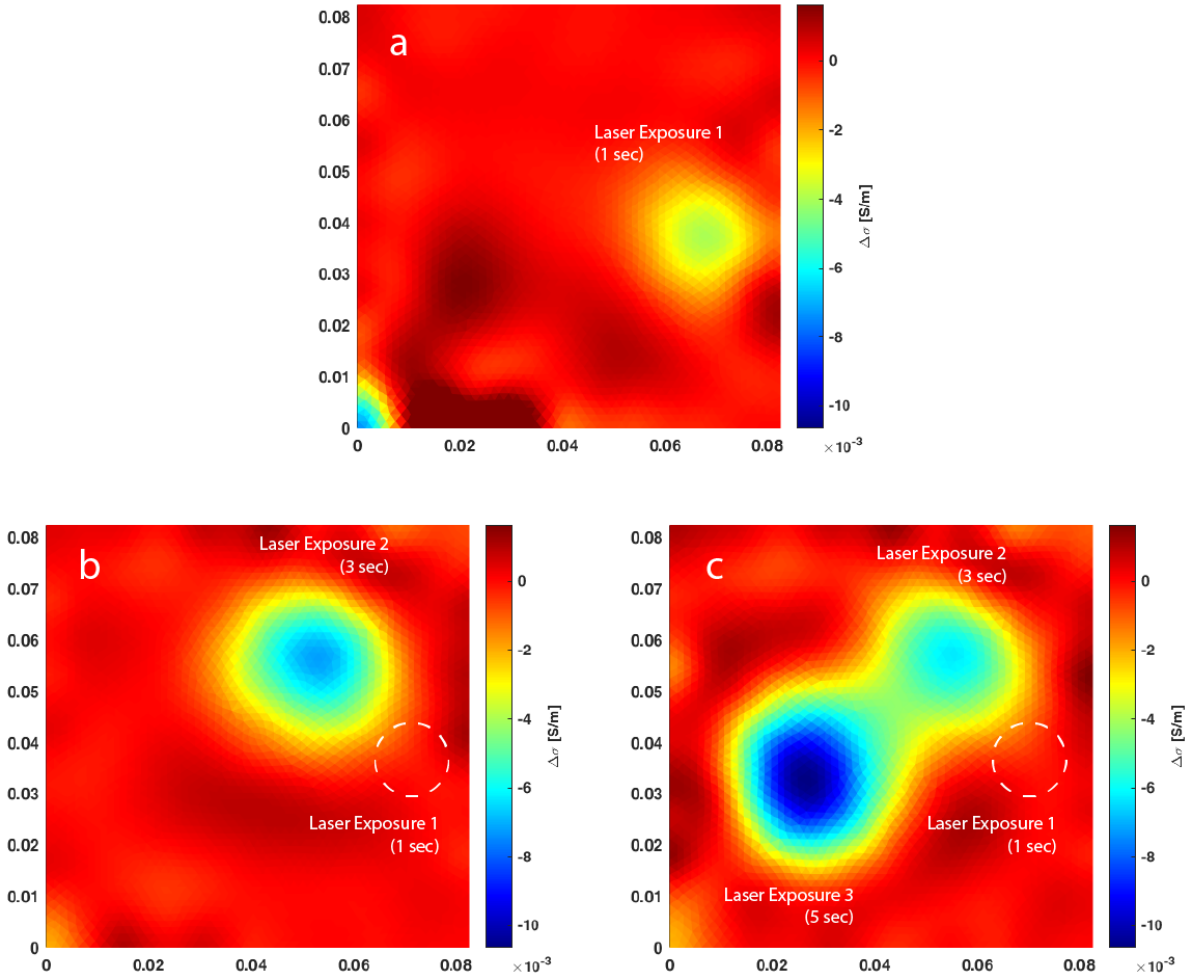

Figure 4.17. Tomographic images of the 3.25" 1 wt.% CNF-modified GFRC plate showing the evolution of damage. (From top to bottom): Conductivity maps after laser exposure of- (a) 1 second, (b) 1 and 3 seconds, and (c) 1, 3, and 5 seconds.

5. SUMMARY AND CONCLUSION

5.1 SUMMARY

In summary, this thesis was inspired by the versatile use of self-sensing nature of CNF-epoxy/GFRC material and the increasing frequency of laser-to-composite interactions in domains such as manufacturing, machining, surface treatment and microstructuring, and military. The optical energy delivered by the laser has the ability to induce potentially deleterious effects on composites. Even with the lack of physical contact, lasers can possibly bring about seemingly impalpable microstructural damage, which can result in degradation of the material. The lack of a method to sense laser exposure impelled the need for this research. It was hypothesized that CNF-modified GFRC can be used to detect laser exposure by taking advantage of the piezoresistive nature of the material.

CNF-modified epoxy with 0.5, 1.0, and 1.5 wt.% CNF was used in GFRC to manufacture rectangular specimens for one-dimensional resistance measurements, while square GFRC specimens with 1.0 wt.% CNF-modified epoxy were manufactured for detecting localized ablation in square plates. Baseline one-dimensional resistance and two-dimensional conductivity measurements were made for the rectangular and square specimens respectively. Specimens were exposed to an infra-red laser operating with nanosecond-pulse duration to induce surface ablation. Optical and electron microscopy of ablated composite specimens revealed some interesting topographical features caused by the local temperature hot-spots created in and around the ablation crater. Unlike cryofractured specimens, these specimens showed the absence of CNF at the damaged surface. Glass fiber bubble formation was observed in and around the crater which indicated pockets of insulating material in the composite. Resistance and conductance measurements were made post-ablation. The rectangular specimens exhibit decreasing baseline resistance with increasing weight percentages of CNF. Increasing weight fractions of CNF also resulted in lesser, but more consistent increase in resistance due to laser ablation. This shows the minimization of DC flow with increasing weight fractions; more CNF signify more pathways for current to flow, thereby lesser resistance. The square specimens utilized EIT to accurately map damage due to laser exposure by computing conductivity changes in the material after each instance of laser ab-

lation. The duration of laser exposure on the square plates was varied as 1, 3, 5, 10, and 20 seconds. Drops in conductivity as small as 7.23×10^{-3} S/m were successfully and accurately detected via EIT.

5.2 CONCLUSION

In conclusion, this work successfully showed that it is indeed possible to detect and localize laser exposure-induced degradation in self-sensing composites via electrical measurements. The optical and electron microscopy images revealed the pockets of insulating glass fiber bubbles, absence of CNFs, and other general destruction of conducting pathways at the ablation site, which is corroborated by the resistance spike and conductivity drop in the rectangular strip specimens and square plate specimens respectively, upon laser exposure. This work also elucidated the electrical effect of increasing CNF weight fraction on self-sensing potential. It is noteworthy that laser exposures that cause damage that is virtually imperceptible by the human eye can readily be detected and localized via EIT. This study therefore advances the state-of-the-art in conductivity-based self-sensing materials by firmly establishing the viability of this approach to laser sensing.

6. RECOMMENDATIONS FOR FUTURE WORK

The work presented in this thesis clearly demonstrates the potential of self-sensing materials for intrinsically monitoring laser exposure via non-invasive electrical measurements. Despite the success of this preliminary study, further work is needed to truly flesh out this concept. The following recommendations for future work are therefore suggested.

[1.] **Multi-scale modeling of ablation and electrical transport processes in CNF-modified polymers:**

Having established the proof-of-concept for this idea, building a computational model capable of explaining the physics behind the heat transfer during laser ablation would be beneficial in understanding the problem more comprehensively. Further, such a model would need to be multi-scale and multi-physical to accurately capture the combined effects of heat transfer, electrical transport, and ablative processes at both the CNF level and the macroscale. The presence of an ablation plume can represent the problem of not accounting the heat absorbed by the vapor species exhibiting the shielding effect. Depending on the power delivered by the laser and the thermal properties of the fiber and nanofiller used, there is a possibility that the material may/may not melt or ablate at all. There is a small, yet non-zero probability of fiber degradation without showing any signs of visual damage. It is therefore beneficial to model the experiment computationally in order to fully understand the interplay of these different processes across length scales.

[2.] **Exploration of the effect of reinforcing fiber type:**

This study uses CNF-modified GFRC with varying weight fractions of CNF as the conductive phase. The glass fiber is thermally insulating and has a softening temperature around 846 °C. Depending on the laser parameters, the power delivered by the laser can reach several gigawatts; this can result in local temperatures on the order of thousands of degrees. In avenues that require high strength and/or high temperature endurance, the glass fiber would need to be replaced by carbon or aramid fibers, depending on the application. Attributing to the relatively higher melting points and different thermo-mechanical properties of the material, it can be hypothesized that they would interact differently with the local temperature hot-spots caused by the laser ablation, i.e., may have a different microstructure

in and around the ablation crater, which can affect the material conductivity. Depending on the power delivered by the laser, there is a non-zero probability that the carbon fiber may not melt at all (due to its extremely high melting point), but degrade ever so slightly without showing any signs of visual damage. Therefore, future work should also consider the effect of different reinforcing fiber phases on laser-based self-sensing. In particular, carbon fibers, which are both electrically and thermally conductive, may render the CNF phase as superfluous.

[3.] **Detailed exploration of effect of nanofiller modification on ablation characteristics:**

Since the addition of nanofiller material to the epoxy matrix phase changes the thermal and electrical transport properties of the bulk material and these properties are tied to ablation characteristics, it is therefore important to develop detailed insight into the precise effect of nanofiller characteristics on ablation properties. The properties of a nanofiller are highly dependent on size, geometry, and composition. The composite manufactured in this study shows the effect of CNF in epoxy. The presence of carbonaceous nanofillers other than CNF (such as graphene, graphite, SWCNT, MWCNT, and CB) and piezoresistive materials such as barium titanate and PZT can result in the different electrical behavior of the composite depending on its piezoresistive behavior [93]. The nanofiller not only makes the composite conductive, but can also alter the mechanical properties of the composite depending on its concentration and mechanical properties. Thus, all of these factors should be studied in detail when designing a composite for self-sensing of laser exposure. For such a study, computational tools as described above would be invaluable.

REFERENCES

[1] C. T. Herakovich, "Mechanics of fibrous composites," 1998.

[2] R. B. Pipes, *Aae 590c: Advanced manufacturing of composite materials: Thermoplastic polymer transitions*, 2020.

[3] M. Knight and D. Curliss, "Composite materials," *Encyclopedia of Physical Science and Technology*, pp. 455–468, 2003.

[4] T. Maiman, "Optical and microwave-optical experiments in ruby," *Physical review letters*, vol. 4, no. 11, p. 564, 1960.

[5] A. E. Siegman, "Lasers university science books," *Mill Valley, CA*, vol. 37, no. 208, p. 169, 1986.

[6] J. Hecht, "A short history of laser development," *Applied optics*, vol. 49, no. 25, F99–F122, 2010.

[7] *Laser overview*. [Online]. Available: http://texaspetawatt.ph.utexas.edu/overview.php.

[8] F. Xing, G. Song, C. Ruan, J. Zhao, and Y. Yang, "The brief introduction of different laser diagnostics methods used in aero-engine combustion research," in *International Journal of Modern Physics: Conference Series*, World Scientific, vol. 42, 2016, p. 1 660 184.

[9] S. H. Yun and S. J. Kwok, "Light in diagnosis, therapy and surgery," *Nature biomedical engineering*, vol. 1, no. 1, pp. 1–16, 2017.

[10] T. Sakimoto, M. I. Rosenblatt, and D. T. Azar, "Laser eye surgery for refractive errors," *The Lancet*, vol. 367, no. 9520, pp. 1432–1447, 2006.

[11] K. D. Solomon, L. E. F. De Castro, H. P. Sandoval, J. M. Biber, B. Groat, K. D. Neff, M. S. Ying, J. W. French, E. D. Donnenfeld, R. L. Lindstrom, *et al.*, "Lasik world literature review: Quality of life and patient satisfaction," *Ophthalmology*, vol. 116, no. 4, pp. 691–701, 2009.

[12] R. E. Fitzpatrick, M. P. Goldman, N. M. Satur, and W. D. Tope, "Pulsed carbon dioxide laser resurfacing of photoaged facial skin," *Archives of dermatology*, vol. 132, no. 4, pp. 395–402, 1996.

[13] S. L. Kilmer and R. R. Anderson, "Clinical use of the q-switched ruby and the q-switched nd: Yag (1064 nm and 532 nm) lasers for treatment of tattoos," *The Journal of dermatologic surgery and oncology*, vol. 19, no. 4, pp. 330–338, 1993.

[14] M. C. Grossman, C. Dierickx, W. Farinelli, T. Flotte, and R. R. Anderson, "Damage to hair follicles by normal-mode ruby laser pulses," *Journal of the American Academy of Dermatology*, vol. 35, no. 6, pp. 889–894, 1996.

[15] P. J. Gilling, C. B. Cass, M. D. Cresswell, and M. R. Fraundorfer, "Holmium laser resection of the prostate: Preliminary results of a new method for the treatment of benign prostatic hyperplasia," *Urology*, vol. 47, no. 1, pp. 48–51, 1996.

[16] M. Sofer, J. D. Watterson, T. A. Wollin, L. Nott, H. Razvi, and J. D. Denstedt, "Holmium: Yag laser lithotripsy for upper urinary tract calculi in 598 patients," *The Journal of urology*, vol. 167, no. 1, pp. 31–34, 2002.

[17] O. Wazni, L. M. Epstein, R. G. Carrillo, C. Love, S. W. Adler, D. W. Riggio, S. S. Karim, J. Bashir, A. J. Greenspon, J. P. DiMarco, *et al.*, "Lead extraction in the contemporary setting: The lexicon study: An observational retrospective study of consecutive laser lead extractions," *Journal of the American College of Cardiology*, vol. 55, no. 6, pp. 579–586, 2010.

[18] R. Hibst and U. Keller, "Experimental studies of the application of the er: Yag laser on dental hard substances: I. measurement of the ablation rate," *Lasers in Surgery and Medicine*, vol. 9, no. 4, pp. 338–344, 1989.

[19] H. A. Wigdor, J. T. Walsh Jr, J. D. Featherstone, S. R. Visuri, D. Fried, and J. L. Waldvogel, "Lasers in dentistry," *Lasers in surgery and medicine*, vol. 16, no. 2, pp. 103–133, 1995.

[20] *Research at max-planck gesselschaft, physiks, attosecond laser*. [Online]. Available: https://www.mpg.de/7021624/postech-attosecond-korea.

[21] *Research at max-planck gesselschaft, physiks*. [Online]. Available: https://www.pks.mpg.de/de/fast/research.

[22] M. Krishnamurthy, M. Kundu, K. Bane, A. D. Lad, P. K. Singh, G. Chatterjee, G. R. Kumar, and K. Ray, "Enhanced x-ray emission from nano-particle doped bacteria," *Optics express*, vol. 23, no. 14, pp. 17 909–17 922, 2015.

[23] G. R. Kumar, "Intense, ultrashort light and dense, hot matter," *Pramana*, vol. 73, no. 1, pp. 113–155, 2009.

[24] C. N. Danson, C. Haefner, J. Bromage, T. Butcher, J.-C. F. Chanteloup, E. A. Chowdhury, A. Galvanauskas, L. A. Gizzi, J. Hein, D. I. Hillier, *et al.*, "Petawatt and exawatt class lasers worldwide," *High Power Laser Science and Engineering*, vol. 7, 2019.

[25] *Airbus had 1,000 parts 3d printed to meet deadline*. [Online]. Available: https://www.bbc.com/news/technology-32597809.

[26] *Ge team secretly printed a helicopter engine, replacing 900 parts with 16*. [Online]. Available: https://www.additivemanufacturing.media/articles/ge-team-secretly-printed-a-helicopter-engine-replacing-900-parts-with-16.

[27] J. S. Suehle, "The magic of lasers in entertainment—behind the technology," in *2014 IEEE International Integrated Reliability Workshop Final Report (IIRW)*, IEEE, 2014, pp. viii–viii.

[28] G. Nyati, R. Palanisamy, M. Alagh, S. Mishra, R. Sharma, and V. D. Vankar, "Development of low-to-high blu-ray recordable (bdr) disc," *Journal of alloys and compounds*, vol. 498, no. 2, pp. 207–210, 2010.

[29] *High energy laser weapon system*. [Online]. Available: https://www.afrl.af.mil/News/Photos/igphoto/2002486787/.

[30] *Laser-directed energy weapon : Uk's dragonfire*. [Online]. Available: https://uk.leonardocompany.com/en/innovation/dragonfire.

[31] D. Zhang and B. Gökce, "Perspective of laser-prototyping nanoparticle-polymer composites," *Applied Surface Science*, vol. 392, pp. 991–1003, 2017.

[32] S. Kumar and J.-P. Kruth, "Composites by rapid prototyping technology," *Materials & Design*, vol. 31, no. 2, pp. 850–856, 2010.

[33] R. Negarestani, M. Sundar, M. Sheikh, P. Mativenga, L. Li, Z. Li, P. Chu, C. Khin, H. Zheng, and G. Lim, "Numerical simulation of laser machining of carbon-fibre-reinforced composites," *Proceedings of the Institution of Mechanical Engineers, Part B: Journal of Engineering Manufacture*, vol. 224, no. 7, pp. 1017–1027, 2010.

[34] Z. Li, H. Zheng, G. Lim, P. Chu, and L. Li, "Study on uv laser machining quality of carbon fibre reinforced composites," *Composites Part A: Applied Science and Manufacturing*, vol. 41, no. 10, pp. 1403–1408, 2010.

[35] V. Oliveira, S. Sharma, M. De Moura, R. Moreira, and R. Vilar, "Surface treatment of cfrp composites using femtosecond laser radiation," *Optics and Lasers in Engineering*, vol. 94, pp. 37–43, 2017.

[36] D. Bäuerle, *Laser processing and chemistry*. Springer Science & Business Media, 2013.

[37] M. Stafe, A. Marcu, and N. N. Puscas, *Pulsed laser ablation of solids: basics, theory and applications*. Springer Science & Business Media, 2013, vol. 53.

[38] *Ucf researchers generate attosecond light from industrial laser*, 2020. [Online]. Available: https://www.ucf.edu/news/ucf-researchers-generate-attosecond-light-from-industrial-laser/.

[39] F. Dausinger, H. Hugel, and V. I. Konov, "Micromachining with ultrashort laser pulses: From basic understanding to technical applications," in *ALT'02 International Conference on Advanced Laser Technologies*, International Society for Optics and Photonics, vol. 5147, 2003, pp. 106–115.

[40] S. Küper, J. Brannon, and K. Brannon, "Threshold behavior in polyimide photoablation: Single-shot rate measurements and surface-temperature modeling," *Applied Physics A*, vol. 56, no. 1, pp. 43–50, 1993.

[41] N. Arnold, B. Luk'Yanchuk, and N. Bityurin, "A fast quantitative modelling of ns laser ablation based on non-stationary averaging technique," *Applied surface science*, vol. 127, pp. 184–192, 1998.

[42] M. Himmelbauer, E. Arenholz, and D. Bäuerle, "Single-shot uv-laser ablation of polyimide with variable pulse lengths," *Applied Physics A*, vol. 63, no. 1, pp. 87–90, 1996.

[43] B. N. Chichkov, C. Momma, S. Nolte, F. Von Alvensleben, and A. Tünnermann, "Femtosecond, picosecond and nanosecond laser ablation of solids," *Applied physics A*, vol. 63, no. 2, pp. 109–115, 1996.

[44] B. Wolff-Rottke, J. Ihlemann, H. Schmidt, and A. Scholl, "Influence of the laser-spot diameter on photo-ablation rates," *Applied Physics A*, vol. 60, no. 1, pp. 13–17, 1995.

[45] J. Heitz, X. Wang, P. Schwab, D. Bäuerle, and L. Schultz, "Krf laser-induced ablation and patterning of y–ba–cu–o films," *Journal of applied physics*, vol. 68, no. 5, pp. 2512–2514, 1990.

[46] T. Beuermann, H. Brinkmann, T. Damm, and M. Stuke, "Picosecond uv excimer laser ablation of linbo3," *MRS Online Proceedings Library (OPL)*, vol. 191, 1990.

[47] M. Eyett and D. Bäuerle, "Influence of the beam spot size on ablation rates in pulsed-laser processing," *Applied physics letters*, vol. 51, no. 24, pp. 2054–2055, 1987.

[48] M. J. Riedl, *Optical design fundamentals for infrared systems*. SPIE press, 2001, vol. 48.

[49] R. Srinivasan, "Interaction of laser radiation with organic polymers," in *Laser Ablation*, Springer, 1994, pp. 107–133.

[50] K.-H. Leitz, B. Redlingshöfer, Y. Reg, A. Otto, and M. Schmidt, "Metal ablation with short and ultrashort laser pulses," *Physics Procedia*, vol. 12, pp. 230–238, 2011.

[51] M. Eyett, D. Bäuerle, W. Wersing, and H. Thomann, "Excimer-laser-induced etching of ceramic pbti1- x zr x o3," *Journal of applied physics*, vol. 62, no. 4, pp. 1511–1514, 1987.

[52] M. Nofar, S. Hoa, and M. Pugh, "Failure detection and monitoring in polymer matrix composites subjected to static and dynamic loads using carbon nanotube networks," *Composites Science and Technology*, vol. 69, no. 10, pp. 1599–1606, 2009.

[53] K. Parmar, M. Mahmoodi, C. Park, and S. S. Park, "Effect of cnt alignment on the strain sensing capability of carbon nanotube composites," *Smart Materials and Structures*, vol. 22, no. 7, p. 075 006, 2013.

[54] L. Gao, E. T. Thostenson, Z. Zhang, and T.-W. Chou, "Sensing of damage mechanisms in fiber-reinforced composites under cyclic loading using carbon nanotubes," *Advanced functional materials*, vol. 19, no. 1, pp. 123–130, 2009.

[55] L. Gao, T.-W. Chou, E. T. Thostenson, Z. Zhang, and M. Coulaud, "In situ sensing of impact damage in epoxy/glass fiber composites using percolating carbon nanotube networks," *Carbon*, vol. 49, no. 10, pp. 3382–3385, 2011.

[56] T. N. Tallman, S. Gungor, K. Wang, and C. E. Bakis, "Damage detection via electrical impedance tomography in glass fiber/epoxy laminates with carbon black filler," *Structural Health Monitoring*, vol. 14, no. 1, pp. 100–109, 2015.

[57] A. Thomas, J. Kim, T. Tallman, and C. Bakis, "Damage detection in self-sensing composite tubes via electrical impedance tomography," *Composites Part B: Engineering*, vol. 177, p. 107 276, 2019.

[58] G. Pandey, M. Wolters, E. T. Thostenson, and D. Heider, "Localized functionally modified glass fibers with carbon nanotube networks for crack sensing in composites using time domain reflectometry," *Carbon*, vol. 50, no. 10, pp. 3816–3825, 2012.

[59] H. Dai and E. T. Thostenson, "Scalable and multifunctional carbon nanotube-based textile as distributed sensors for flow and cure monitoring," *Carbon*, vol. 164, pp. 28–41, 2020.

[60] T.-C. Hou, K. J. Loh, and J. P. Lynch, "Spatial conductivity mapping of carbon nanotube composite thin films by electrical impedance tomography for sensing applications," *Nanotechnology*, vol. 18, no. 31, p. 315 501, 2007.

[61] M. Clausi, E. Toto, S. Botti, S. Laurenzi, V. La Saponara, and M. G. Santonicola, "Direct effects of uv irradiation on graphene-based nanocomposite films revealed by electrical resistance tomography," *Composites Science and Technology*, vol. 183, p. 107 823, 2019.

[62] T. Buasiri, K. Habermehl-Cwirzen, L. Krzeminski, and A. Cwirzen, "Piezoresistive load sensing and percolation phenomena in portland cement composite modified with in-situ synthesized carbon nanofibers," *Nanomaterials*, vol. 9, no. 4, p. 594, 2019.

[63] J. Sandler, J. Kirk, I. Kinloch, M. Shaffer, and A. Windle, "Ultra-low electrical percolation threshold in carbon-nanotube-epoxy composites," *Polymer*, vol. 44, no. 19, pp. 5893–5899, 2003.

[64] N. Hu, Z. Masuda, G. Yamamoto, H. Fukunaga, T. Hashida, and J. Qiu, "Effect of fabrication process on electrical properties of polymer/multi-wall carbon nanotube nanocomposites," *Composites Part A: Applied Science and Manufacturing*, vol. 39, no. 5, pp. 893–903, 2008.

[65] W. Bauhofer and J. Z. Kovacs, "A review and analysis of electrical percolation in carbon nanotube polymer composites," *Composites science and technology*, vol. 69, no. 10, pp. 1486–1498, 2009.

[66] K. Almuhammadi, T. K. Bera, and G. Lubineau, "Electrical impedance spectroscopy for measuring the impedance response of carbon-fiber-reinforced polymer composite laminates," *Composite Structures*, vol. 168, pp. 510–521, 2017.

[67] J. G. Simmons, "Generalized formula for the electric tunnel effect between similar electrodes separated by a thin insulating film," *Journal of applied physics*, vol. 34, no. 6, pp. 1793–1803, 1963.

[68] T. Tallman and K. Wang, "An arbitrary strains carbon nanotube composite piezoresistivity model for finite element integration," *Applied Physics Letters*, vol. 102, no. 1, p. 011 909, 2013.

[69] R. B. Pipes, *Aae 590c: Advanced manufacturing of composite materials: Transport property measurement*, 2020.

[70] T. Tallman and H. Hassan, "A network-centric perspective on the microscale mechanisms of complex impedance in carbon nanofiber-modified epoxy," *Composites Science and Technology*, vol. 181, p. 107 669, 2019.

[71] T. N. Tallman and H. Hassan, "A computational exploration of the effect of alignment and aspect ratio on alternating current conductivity in carbon nanofiber–modified epoxy," *Journal of Intelligent Material Systems and Structures*, vol. 31, no. 5, pp. 756–770, 2020.

[72] T. N. Tallman and D. J. Smyl, "Structural health and condition monitoring via electrical impedance tomography in self-sensing materials: A review," *Smart Materials and Structures*, vol. 29, no. 12, p. 123 001, 2020.

[73] K. J. Loh, T.-C. Hou, J. P. Lynch, and N. A. Kotov, "Carbon nanotube sensing skins for spatial strain and impact damage identification," *Journal of nondestructive evaluation*, vol. 28, no. 1, pp. 9–25, 2009.

[74] B. R. Loyola, V. La Saponara, K. J. Loh, T. M. Briggs, G. O'Bryan, and J. L. Skinner, "Spatial sensing using electrical impedance tomography," *IEEE Sensors Journal*, vol. 13, no. 6, pp. 2357–2367, 2013.

[75] *Pyrograf iii carbon nanofiber, hht grade*, Version 9, Pyrograf Products, Inc., Aug. 2016. [Online]. Available: http://pyrografproducts.com/nanofiber.html#-PR-24-XT-HHT-Data-Sheet.

[76] *Style 7725 bi-directional e-glass*, FibreGlast. [Online]. Available: https://s3.amazonaws.com/cdn.fibreglast.com/downloads/00079.pdf.

[77] *System 2000 epoxy resin*, Version 9, FibreGlast, Aug. 2019. [Online]. Available: https://s3.amazonaws.com/cdn.fibreglast.com/downloads/00343.pdf.

[78] *System 2000 epoxy hardener*, Version 1.00, FibreGlast, Aug. 2019. [Online]. Available: https://s3.amazonaws.com/cdn.fibreglast.com/downloads/PDCT-SDS-00132.pdf.

[79] *Triton x-100*, Version 6.6, Sigma-Aldrich, Aug. 2020. [Online]. Available: https://www.sigmaaldrich.com/MSDS/MSDS/DisplayMSDSPage.do?country=US&language=en&productNumber=X100&brand=SIAL&PageToGoToURL=https%5C%3A%5C%2F%5C%2Fwww.sigmaaldrich.com%5C%2Fcatalog%5C%2Fproduct%5C%2Fsial%5C%2Fx100%5C%3Flang%5C%3Den.

[80] T. Tallman, S. Gungor, K. Wang, and C. Bakis, "Damage detection and conductivity evolution in carbon nanofiber epoxy via electrical impedance tomography," *Smart Materials and Structures*, vol. 23, no. 4, p. 045 034, 2014.

[81] *Byk-a*, BYK, Sep. 2019. [Online]. Available: https://www.byk.com/en/products/additives-by-name/byk-a-501.

[82] D. S. Holder, *Electrical impedance tomography: methods, history and applications*. CRC Press, 2004.

[83] D. Liu, V. Kolehmainen, S. Siltanen, and A. Seppänen, "A nonlinear approach to difference imaging in eit; assessment of the robustness in the presence of modelling errors," *Inverse Problems*, vol. 31, no. 3, p. 035 012, 2015.

[84] D. Liu, V. Kolehmainen, S. Siltanen, A.-M. Laukkanen, and A. Seppänen, "Nonlinear difference imaging approach to three-dimensional electrical impedance tomography in the presence of geometric modeling errors," *IEEE Transactions on Biomedical Engineering*, vol. 63, no. 9, pp. 1956–1965, 2015.

[85] D. Smyl, S. Bossuyt, W. Ahmad, A. Vavilov, and D. Liu, "An overview of 38 least squares–based frameworks for structural damage tomography," *Structural Health Monitoring*, vol. 19, no. 1, pp. 215–239, 2020.

[86] T. Tallman and J. Hernandez, "The effect of error and regularization norms on strain and damage identification via electrical impedance tomography in piezoresistive nanocomposites," *NDT & E International*, vol. 91, pp. 156–163, 2017.

[87] *Pulsed lasers: Introduction to power and energy calculations*, Jul. 2019. [Online]. Available: https://www.thorlabs.com/images/tabimages/Laser-Pulses-Power-Energy-Equations.pdf.

[88] *Laser viewing card*, Rev C, ThorLabs, Jun. 2015. [Online]. Available: https://www.thorlabs.com/-sd.cfm?fileName=19180-S01.pdf&partNumber=VRC2.

[89] AGY, *High strength glass fibers*, 2006. [Online]. Available: https://www.agy.com/wp-content/uploads/2014/03/High-Strength-Glass-Fibers-Technical.pdf.

[90] W. Pietenpol, "Surface tension of molten glass," *Physics*, vol. 7, no. 1, pp. 26–31, 1936.

[91] I. M. Hauner, A. Deblais, J. K. Beattie, H. Kellay, and D. Bonn, "The dynamic surface tension of water," *The journal of physical chemistry letters*, vol. 8, no. 7, pp. 1599–1603, 2017.

[92] R. Marie Kernaghan, "Surface tension of mercury," *Physical Review*, vol. 37, no. 8, p. 990, 1931.

[93] P. Chen and S.-C. Wong, "Polymer nanocomposites reinforced with carbonaceous nanofillers and their piezoresistive behavior," in *Physical Properties and Applications of Polymer Nanocomposites*, Elsevier, 2010, pp. 404–430.